A SEARCH FOR EXTRATERRESTRIAL POINT-SOURCES OF NEUTRINOS WITH AMANDA-II

by

DAVID ARTHUR STEELE

A dissertation submitted in partial fulfillment of the
requirements for the degree of

DOCTOR OF PHILOSOPHY
(PHYSICS)

at the

UNIVERSITY OF WISCONSIN – MADISON

2004

A Search for Extraterrestrial Point-sources of Neutrinos with AMANDA-II

David Arthur Steele

Under the supervision of Professor Francis Halzen
At the University of Wisconsin — Madison

Frozen within the deep, pristine ice of the South Polar icecap, the Antarctic Muon and Neutrino Detector Array (AMANDA) glimpses at the fleeting signatures of muons resulting from the rare interactions of neutrinos: electrically neutral and nearly massless subatomic particles adept to carrying astronomical information. Neutrinos have the potential to reveal the mysterious engines that accelerate cosmic rays to energies in excess of 10^{20} eV. Completed in 2000, the AMANDA-II array has a larger sensitive volume, better angular resolution, and improved background rejection over it's predecessor AMANDA-B10. This work describes a search for neutrinos of astrophysical origin above a background of terrestrial atmospheric neutrinos using the first year of data collected using AMANDA-II. The search sample, comprising 699 muon events, is found to be statistically consistent with a random distribution of atmospheric neutrinos, and atmospheric muons near the horizon. Limits averaging $E^2 d\Phi_\nu/dE = 2\times10^{-7}\,\mathrm{GeV\,cm^{-2}\,s^{-1}}$ are placed on specific known astrophysical sources of high-energy γ-rays. With just 197 days live-time, AMANDA-II attains the benchmark sensitivity of $\nu/\gamma \sim 1$ to the blazar Markarian 501.

Francis Halzen (Adviser)

To my mother

my first and most important teacher,

for always encouraging me to chase my dreams.

Acknowledgments

Modern science is not performed by individuals in isolation. Every thesis written in this collaboration stands on a strong foundation built by hundreds of individuals, with many of whom I've had the pleasure of meeting and working. The AMANDA collaboration embodies curiosity, imagination, and strong dedication to improve our human understanding the Universe. I thank my collaboration, especially my colleagues in Madison, for the privilege of the last four years.

It was a pleasure to work in close collaboration with my counterpart from DESY-Zeuthen, Tonio Hauschildt. In Madison, I especially want to thank Gary Hill and Paolo Desiati for their mentor-ship and helpful contributions to the analysis.

As a student, I have enjoyed the rare pleasure of effectively having two complementary advisers, Albrecht Karle and Francis Halzen. I thank Albrecht for being a source of practical guidance and optimism, and Francis for his contagiously youthful enthusiasm and inspiration.

Contents

Chapter 1

Extending Our Senses

As human beings, we have the capacity to extend our senses beyond their natural limits. We also have the capacity, and perhaps even a need, to imagine.

The night sky has fueled human imagination since the earliest times. Thousands of years ago, our ancestors gazed into the heavens and imagined characters and stories playing out among the stars. Today, the sky is still a theater, but today's stories are far more bizarre and awe-inspiring than the ancients could have ever imagined. By extending our senses to learn more about the sky, we are expanding not only our perception of the universe, but also the collective capacity of human imagination.

The rapid scientific and technological advances of the last century have radically changed our human perception of the universe, and the latest advances have poised us to expand our perception in a new way. This thesis describes our first glimpse at the high-energy neutrino sky using the completed Antarctic Muon and Neutrino Detector Array (AMANDA-II), the world's largest and most sensitive high-energy neutrino telescope.

1.1 Photon Astronomy

AMANDA-II is an adolescent in the infant field of experimental neutrino astrophysics. In a larger context, it is just another new instrument, constructed with the same desire to explore the universe through observation kindled by astronomers for centuries. Traditional astronomy began with an extension of the sensitivity of the human eye. The telescope allowed astronomers to collect and focus more photons allowing us to see more detail at greater distances. But the human eye is sensitive to a mere fraction of a decade in electromagnetic energy (and wavelength, λ), from red ($\lambda \simeq 4 \times 10^{-5}\,\mathrm{cm}$) to violet ($\lambda \simeq 7 \times 10^{-5}\,\mathrm{cm}$). This means that even the telescope-aided human eye is insensitive to most of the electromagnetic radiation in the universe, as illustrated in Fig. 1.1.

Advances in technology beginning in the early 20th century have extended our senses out to all of the available electromagnetic wavelengths, from highly energetic gamma rays to the least energetic radio waves. Each new advance has invariably led to the discovery of previously unimagined phenomena: pulsars, active galaxies, and gamma ray bursts, for example. While some observations refine our knowledge, others prompt new questions.

The field of high-energy (gamma ray) astronomy is barely thirty years old. The late satellite-borne EGRET [2], and the HEGRA system of air Cerenkov telescopes [3], have mapped the high-energy photon sky from a few GeV ($10^{9}\,\mathrm{eV}$) to 10s of TeV ($10^{12}\,\mathrm{eV}$) in energy. Instruments such as these reveal supernova remnants, microquasars, active galaxies, and other objects to be gamma-ray emitters. These objects accelerate electrons which produce gamma rays through radiative processes (inverse

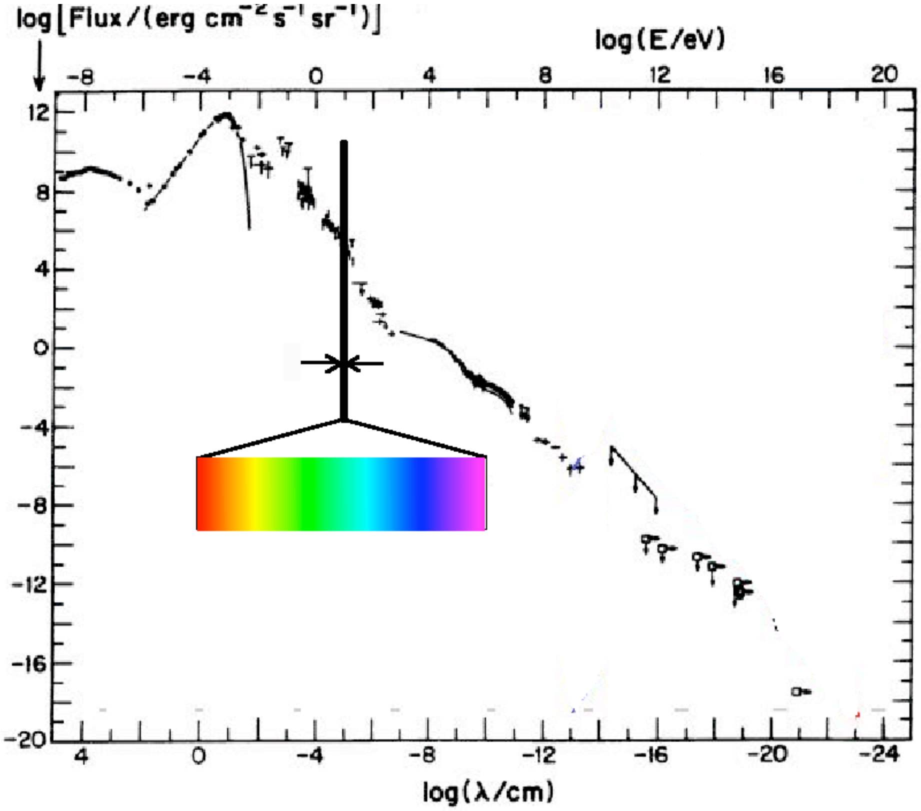

Figure 1.1: The extraterrestrial diffuse flux of electromagnetic radiation, from radio to gamma rays, is shown. The human eye is sensitive only to a narrow band of wavelengths at 10^{-5} cm. Modified from [1].

Compton scattering or synchrotron radiation). They may also accelerate protons, which collide with matter or ambient radiation to produce neutrinos, as well as photons.

Gamma ray astronomers have made great strides in technology in the last decades, but photons have their own intrinsic limitations as astronomical messengers. As shown in Fig. 1.2, photons with energy $E_\gamma > 100\,\mathrm{TeV}$ travel only 10 kpc ($1\,\mathrm{kpc} = 3 \times 10^{16}\,\mathrm{m}$) before scattering with the diffuse CMB. When viewing the blazar Markarian 501, HEGRA observes a "cutoff" energy of about 10 TeV due to scattering of the high-energy gamma rays with the diffuse infrared photon field around the source. Photons can only shed light on the universe up to a certain energy, and can not readily distinguish between electromagnetic and hadronic processes.

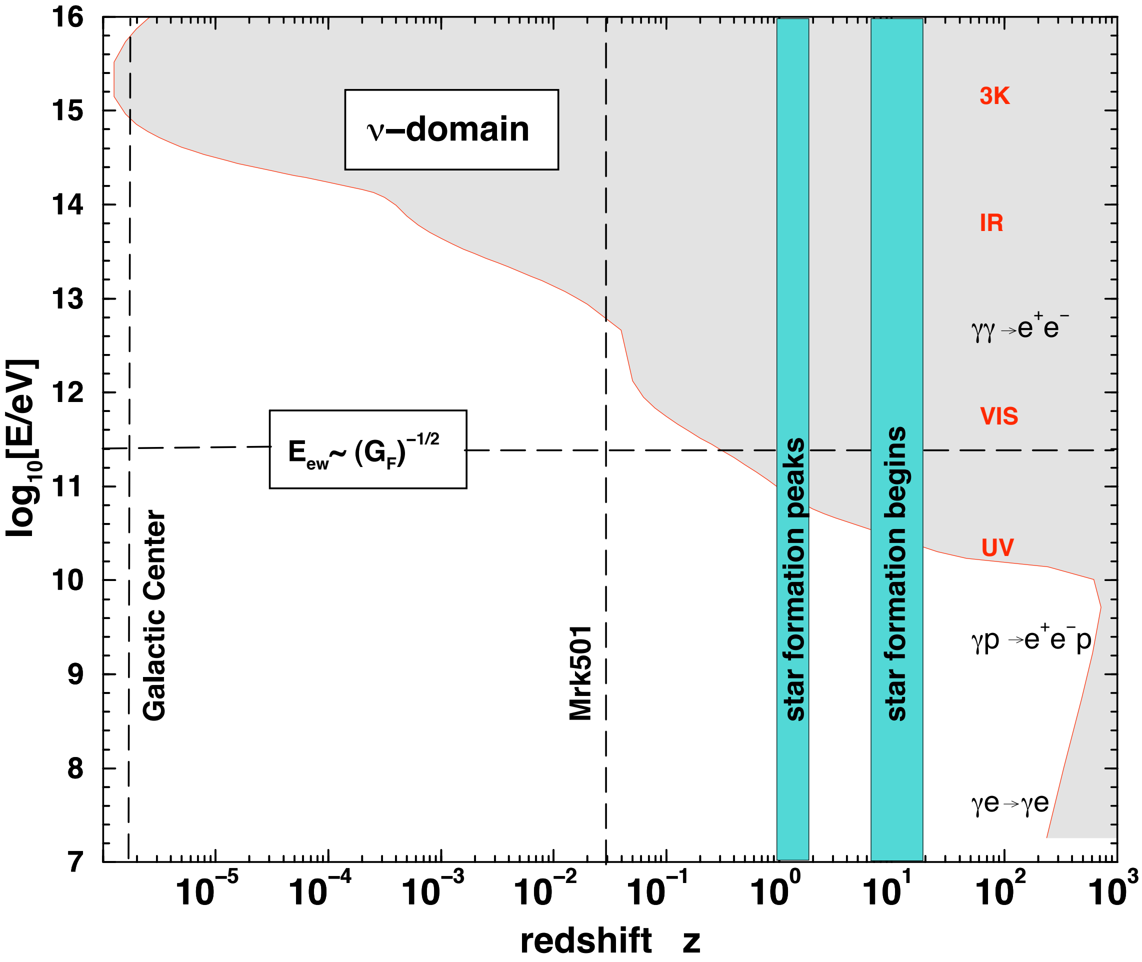

Figure 1.2: The photon horizon (redshift) vs. photon energy. Redshift is related to the distance via the Hubble constant, $d = zc/H$ (in a non-relativistic approximation) with $H \approx 75\,\mathrm{km\,s^{-1}\,Mpc^{-1}}$. The dominant modes of absorption at various photon energies are listed to the right. From [1].

1.2 Cosmic Rays

Cosmic rays are extra-terrestrially accelerated protons and heavier atomic nuclei impacting on the Earth's atmosphere. Since they were discovered aboard a hot air balloon by Victor Hess in 1912, our knowledge of cosmic rays has grown substantially.

Today's two largest Cosmic Ray observatories, AGASA and HiRes, have observed a handful of extremely-high-energy (EHE) cosmic ray air showers with primary energy above $10^{20}\,\mathrm{eV}$, or in macroscopic units, 10s of Joules [4, 5]. The largest laboratory particle accelerators can only reach energies up to a few times $10^{12}\,\mathrm{eV}$, making cosmic rays by far the most energetic particles ever observed.

Where are they accelerated? Cosmic rays have electric charge so one can not use directional information to deduce an origin. At high enough energy, a proton points back to its source with accuracy ($\Delta\theta$) determined by its gyro-radius in the intergalactic magnetic field, B:

$$\Delta\theta \simeq \frac{d}{R_{\mathrm{gyro}}} = \frac{dB}{E} \tag{1.1}$$

where d is the distance to the source, and E is the particle energy. Estimates of the strength of the intergalactic magnetic field run from 10^{-7} to 10^{-12} Gauss, thus the resolution carried by a particle with energy $3 \times 10^{20}\,\mathrm{eV}$ originating in a nearby galaxy ($d = 100\,\mathrm{Mpc}$) could be better than a degree for lower values of B. Based on observations of their highest energy (least deflected) events, HEGRA and HiRes both favor an extragalactic origin for the observed EHE cosmic rays, but can not be more specific.

One may further speculate on the origin cosmic rays by examining the observed energy spectrum shown in Fig. 1.3. The spectrum is characterized by a broken power

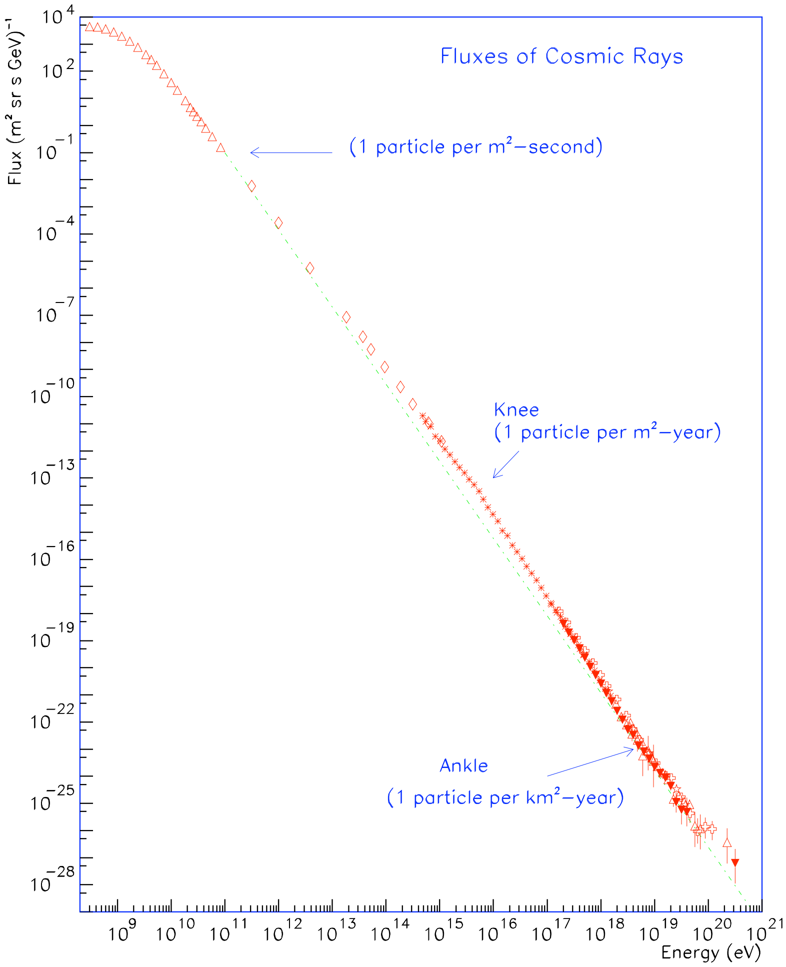

Figure 1.3: The flux of cosmic rays vs. energy and approximate integral flux per decade in energy. From [6].

law, with a “knee” near 10^{16} eV and an “ankle” near 10^{19} eV. Supernovae remnants in our own galaxy are likely candidates for the sites of proton acceleration up to energies of $\sim 10^{16}$ eV. The “knee” indicates the onset of a component of the spectrum thought to be extragalactic in origin.

Much progress has been made understanding how charged particles may be accelerated in magnetic shocks initiated by objects like supernovae explosions, or in “fireball” models of gamma ray bursts. But these conventional models must be pushed to their limits to explain the production of extremeley-high-energy cosmic rays, and as yet, no cosmic accelerators have been experimentally identified.

The problem is further exacerbated by the Greisen-Zatsepin-Kuzmin (GZK) cutoff. Just as is the case for high-energy photons, the universe is opaque to EHE cosmic rays. At energies above $E_{\mathrm{GZK}} \sim 5 \times 10^{19}\,\mathrm{eV}$, protons interact with CMB photons via the delta resonance,

$$p + \gamma_{\mathrm{CMB}} \rightarrow \Delta^* \rightarrow N\pi. \tag{1.2}$$

EHE protons with energy E_{GZK} have an attenuation length of 50 kpc (about the size of a galaxy), so if they are indeed of extragalactic origin, we should not be able to observe them in large numbers. Yet between the AGASA and HiRes experiments, about 20 events with $E > E_{\mathrm{GZK}}$ have been observed. The data are still somewhat controversial; HiRes claims to see the expected event reduction due to the GZK cutoff, while the AGASA claims to see a violation of the GZK cutoff [7].

We know that protons (and/or other charged hadrons) are being accelerated somewhere, and gamma ray observations hint at possible candidate sources, but neither gamma ray astronomy nor cosmic ray astronomy can conclusively settle the question of where and how the cosmos accelerates its most energetic particles.

1.3 Neutrinos

With no electrical charge and minuscule mass, neutrinos, though copious throughout the universe ($\rho_\nu \simeq 200/\mathrm{cm}^3$) lead solitary existences, interacting with other particles and radiation rarely, and even then feeling only the Weak force. With these properties, neutrinos are adept to carrying astronomical information across cosmological distances. Highly energetic photons have an attenuation length on the order of $1\,\mathrm{gm\,cm^{-2}}$ whereas a 1 TeV neutrino has an attenuation length of $2.5 \times 10^{11}\,\mathrm{gm\,cm^{-2}}$.

Highly energetic neutrinos are born out of collisions of highly energetic protons with matter and radiation, so wherever nature is accelerating cosmic ray protons, high-energy neutrinos are likely to be produced as well. The general scenario is depicted in Fig. 1.4. Protons (p) are accelerated by some cosmic accelerator (see §2.3 for specific classes of suspected cosmic proton accelerators) and impact on a beam dump. In some cases the beam dump is the radiation of the acceleration region; in others it might be a gaseous or dusty region like a molecular cloud. Neutrinos (ν) are produced (as described in §2.1.1) and escape the beam dump. Unlike charged cosmic rays, neutrinos propagate undeflected by magnetic fields, and proceed unhindered through matter and radiation opaque to photons (γ), and arrive at a terrestrial neutrino detector.

The same properties that engender neutrinos with the ability to carry information across cosmological distance scales render them elusive to detection. Neutrinos can not be detected directly; their presence must be deduced by the detection of leptons resulting from rare neutrino interactions in suitable detection media. Solar neutrinos, with a flux of $5 \times 10^{6}\,\mathrm{cm^{-2}\,s^{-1}}$ at the Earth, have tiny interaction cross sections, typically 30 orders of magnitude smaller than that of an electron or muon. At higher energies, the neutrino cross section rises, but is balanced by a decrease in flux with increasing energy.

The progress in neutrino detection of the last half century has shown that despite the neutrino's elusive characteristics, a picture of the neutrino sky is technologically within our grasp. As will be demonstrated in this thesis, the AMANDA-II neutrino

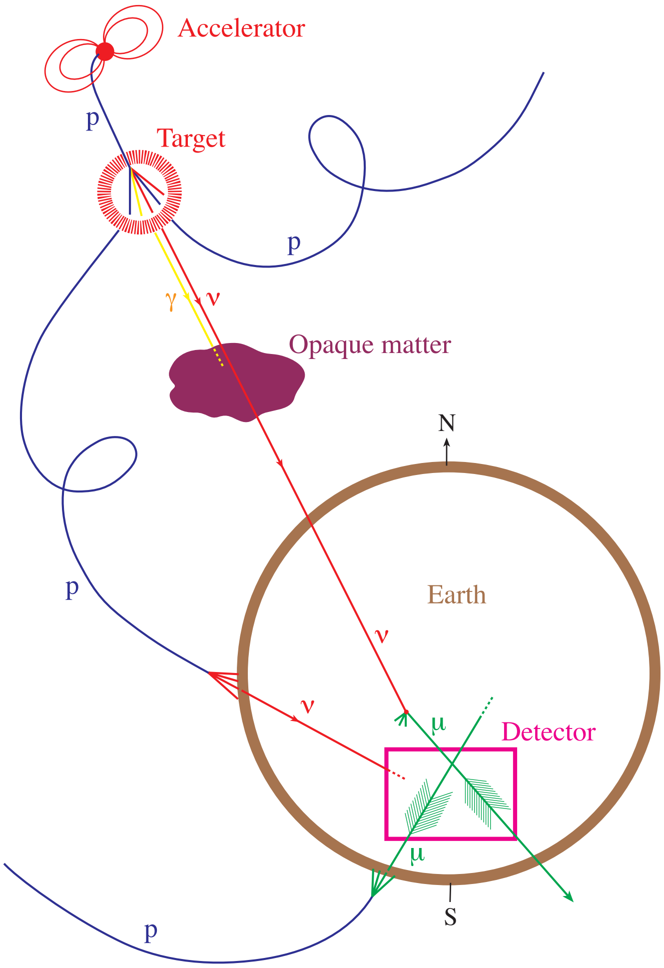

Figure 1.4: A cartoon demonstrating the principles of neutrino astronomy, as described in the text.

telescope has reached an important milestone in the young field of neutrino astrophysics: sensitivity to detect a neutrino source of strength equal to the observed photon flux of the gamma-ray-loud active galaxy Markarian 501..

Chapter 2

High Energy Neutrino Astrophysics

Neutrinos were theoretically postulated in the 1930s, by Wolfgang Pauli, who remarked: “I have done a terrible thing. I have postulated a particle that cannot be detected.” The pioneering theoretical work on the neutrino by Pauli and Enrico Fermi indicated the neutrino to have no charge, and a very tiny detection cross section.

But the neutrino would not go undetected for long. Twenty years after its existence was postulated, low energy neutrinos produced in a nuclear reactor were experimentally observed by Reines and Cowan. In the 1960’s Ray Davis and his collaborators became the first people to observe neutrinos of astrophysical origin. They built their detector in the Homestake gold mine planning to observe low energy solar neutrinos. They recorded only one third the neutrino flux predicted by solar models, thus posing the “solar neutrino problem” [8]. The experiment marked the birth of the new field of neutrino astrophysics, a child of astronomy and particle physics.

The 1980’s ushered in several other neutrino experiments designed to study the solar neutrino problem and neutrino oscillations. In February, 1987, the Japanese Kamiokande-II and the U.S. IMB neutrino detectors simultaneously captured the first neutrinos of extragalactic origin [9, 10, 11, 12], associated with supernova SN1987A in our nearby satellite galaxy, the Large Magellanic Cloud. In total, less than 20 individual neutrinos were detected from SN1987A, representing a faint but significant glimpse of the universe through the neutrino window.

Studies aimed at preparing for the construction of a high energy neutrino telescope in deep ocean water off the coast of Hawaii (DUMAND) began as early as 1976 and culminated in a proposal in 1988 [13]. Problems with the technology after the deployment of a prototype optical sensor [14] resulted in the project being canceled in 1995. Other efforts to construct ocean-based neutrino telescopes (NESTOR [15], ANTARES [16], NEMO [17], Baikal [18]) were forthcoming, but also met with significant delays and challenges associated with deployment in water.

Overcoming many of those challenges by instead deploying in ice, AMANDA-B10 was commissioned as the first operational neutrino telescope in 1997. AMANDA-B10 provided needed proof of the neutrino telescope concept by detecting neutrinos created above the Earth as byproducts of cosmic ray collisions with the Earth's atmosphere [19]. These observations provided a successful test of not only the AMANDA concept, but of particle physics at energies not accessible in the laboratory. The observed energy spectra and arrival distributions were consistent with simulations embodying the most current particle physics knowledge.

It has taken seven decades since the theoretical birth of the neutrino, but mankind now has the technology to at last take advantage of neutrinos to advance astrophysics. As yet no astrophysical source of high energy neutrinos has been identified, so any discussion of the properties of astrophysical sources of neutrinos is inherently speculative. In the present absence of a signal detection, an understanding of what a neutrino signal *might* look like is, however, possible based on our current understanding of particles and astrophysics. We begin by discussing the relevant properties of neutrinos themselves in §2.1. Then, theoretical predictions of astrophysical neutrino fluxes are discussed in §2.2, followed by brief descriptions of several of the various classes of suspected cosmic particle accelerators in §2.3.

2.1 Neutrino Properties

Somewhere in the universe, protons are accelerated to energies in excess of 10^{20} eV [4, 5], and are likely accompanied by high energy gamma rays resulting from the interaction of the accelerated protons with the intrinsic radiation of the source, or with photons of the cosmic microwave background (CMB),

$$\begin{aligned} p + \gamma &\rightarrow p + \pi^0 \\ &\qquad \longmapsto \pi^0 \rightarrow 2\gamma. \end{aligned} \tag{2.1}$$

But gamma rays are also produced by radiative processes involving accelerated electrons, such as Compton scattering, synchrotron emission, and bremsstrahlung. The detection of gamma rays is hence insufficient evidence that a source is responsible for the acceleration of UHE cosmic rays.

2.1.1 Astrophysical Neutrino Production

High energy neutrinos are known to be produced only by hadronic processes, most commonly pion or kaon decay,

$$
\begin{aligned}
&p + X \rightarrow \pi^{\pm} + Y \\
&\qquad\qquad \longmapsto \mu^{\pm} + \nu_{\mu}(\bar{\nu}_{\mu}) \\
&\qquad\qquad\qquad \longmapsto e^{\pm} + \nu_{e}(\bar{\nu}_{e}) + \bar{\nu}_{\mu}(\nu_{\mu}) \\
\\
&p + X \rightarrow K^{\pm} + Y \\
&\qquad\qquad \longmapsto \mu^{\pm} + \nu_{\mu}(\bar{\nu}_{\mu}) \\
&\qquad\qquad\qquad \longmapsto e^{\pm} + \nu_{e}(\bar{\nu}_{e}) + \bar{\nu}_{\mu}(\nu_{\mu}) \\
\\
&p + X \rightarrow K_L^{0} + Y \\
&\qquad\qquad \longmapsto \pi^{\pm} + \mu^{\pm} + \nu_{\mu}(\bar{\nu}_{\mu}) \\
&\qquad\qquad \longmapsto \pi^{\pm} + e^{\pm} + \nu_{e}(\bar{\nu}_{e}).
\end{aligned}
\tag{2.2}
$$

Neutrinos are produced in a cosmic source when accelerated protons interact with other protons, heavier nuclei, or the source's own radiation field. With roughly equal numbers of decays from π^0, π^+, and π^-, we would expect one neutrino produced for every γ. Thus the presence of neutrinos from a gamma source would allow us to distinguish between acceleration of electrons and hadrons, and the observed ν/γ ratio would allow us to probe the relative contributions of hadronic and electromagnetic processes to the acceleration mechanism.

2.1.2 Propagation and Oscillation

Since neutrinos feel only the Weak force, they easily escape from the region of production and propagate away in straight lines. In the standard model of particle physics prevalent in recent decades, all neutrinos were taken to be massless. However, since the 1998 announcement by the Super-Kamiokande collaboration [20] and subsequent confirmation by other experiments [21, 22], it has become accepted practice to account for non-zero neutrino mass and consequent oscillation between neutrino flavors.

Oscillations between mass eigenstates are observed in quarks and have long been theoretically well-described [23]. The theory of neutrino oscillations is described in the same way, using a using a mixing matrix to relate the flavor eigenstates to the mass eigenstates. Neutrino oscillations are often described, for simplicity, using a two-flavor approximation (see [24], for example). In this approximation,, valid when the $\nu_\mu \rightarrow \nu_e$ admixture is low, neutrino oscillations are described by two parameters, the difference in mass, Δm between the mass eigenstates, and a mixing angle, θ, such that the probability of a muon neutrino created with energy E_ν to later be observed as a muon neutrino after traveling a distance L is given by

$$P_{\mu\rightarrow\mu} = 1 - \sin^2(2\theta)\,\sin^2\left(1.27\,\Delta m^2/\mathrm{eV}^2 \frac{L/\mathrm{km}}{E_\nu/\mathrm{GeV}}\right). \tag{2.3}$$

For astrophysical neutrinos with $E_\nu > 1\mathrm{TeV}$, the wavelength of oscillation is much smaller than the typical cosmological distance between the source and the observer. Hence, we would expect an equipartition of the source flux, produced in an approximate ratio of $\nu_e : \nu_\mu : \nu_\tau = 1 : 2 : 0$ (as seen in Eqn. 2.2), to a ratio of $1 : 1 : 1$. Therefore, we must be cognizant of a possible missing factor of two when comparing muon neutrino flux upper limits at a detector on the Earth to source flux predictions not accounting for oscillations.

2.1.3 Interaction and Detection

Neutrinos, feeling only the Weak force, can not be seen directly. A neutrino's presence can only be experimentally deduced based on the detection of its interaction products, charged leptons. Neutrinos and anti-neutrinos interact in AMANDA via weak charged-current scattering,

$$\begin{aligned} \nu_l + N &\rightarrow l^+ + X \\ \overline{\nu}_l + N &\rightarrow l^- + X \end{aligned} \tag{2.4}$$

where N is the target nucleon (in the ice or bedrock below the detector) and l is the associated lepton: electron, muon or tau. The lepton is detected as it propagates in the ice leaving a wake of Cerenkov light. The cross sections for the interaction in Eqn. 2.4 are typically quite small, as shown in Fig. 2.1, requiring a large detection volume to provide reasonable detection rates.

If AMANDA is to serve as a telescope, it must have the ability to accurately resolve the trajectory of the lepton, which is nearly collinear with the incident neutrino. Electrons resulting from the interaction of ν_{e} typically range out after traveling less than a few meters in ice. Taus, on account of their short lifetime, also travel only a relatively short distance compared muons. A muon, having a greater mass than an electron ($m_\mu \simeq 207\, m_{\mathrm{e}}$) and a small nucleonic interaction cross section, typically travels hundreds to thousands of meters in ice, accompanied by energy deposition manifesting in optically detectable Cerenkov radiation. The trace-like signature provides a long lever-arm for the reconstruction of the muon track. Furthermore, the

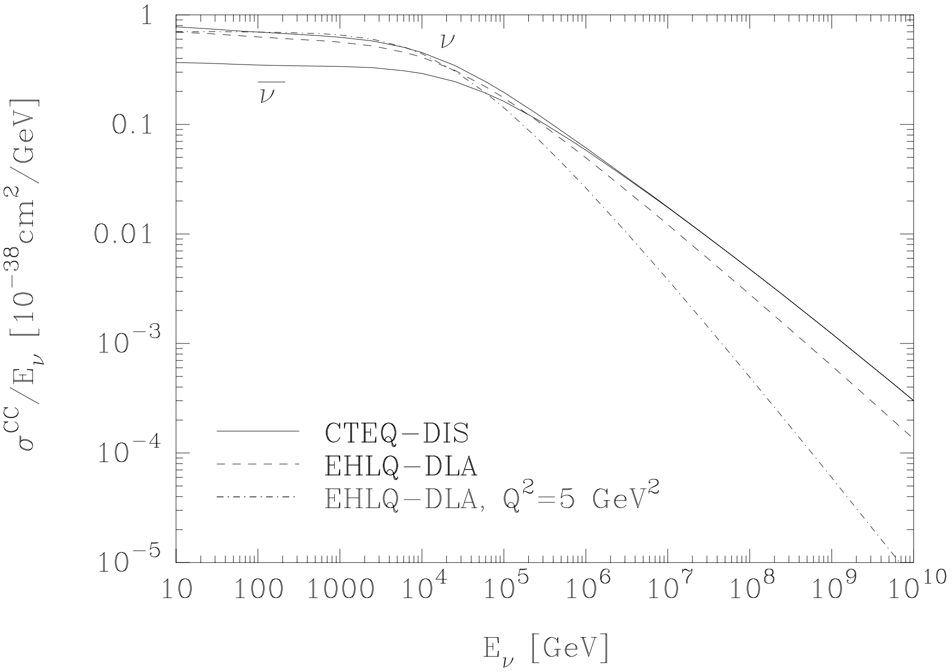

Figure 2.1: Muon neutrino and anti-neutrino interaction cross section vs. neutrino energy, E_ν. Solid curves are based on the CTEQ3 parton distributions; dashed and dot-dashed curves are based on older measurements. From [25].

long muon range greatly increases the effective detection volume, and thus enhances the detection probability for muon neutrinos over the other flavors. The detectability (probability of detection) of the muon goes as

$$P_\mu(E_\nu) \sim \sigma_{\rm CC}(E_\nu) \cdot \langle R(E_\nu) \rangle \tag{2.5}$$

where $\langle R(E_\nu) \rangle$ is the average range of the muon in ice (discussed further in §3.1.2).

At energies above the AMANDA-II threshold of $E_\nu >\sim 100\,\text{GeV}$, muons resulting from Eqn. 2.4 carry about half the neutrino energy, the other half carried by the hadronic cascade, X. The muon propagates in a near-straight line, having a mean deviation from the path of the incident neutrino of

$$\sqrt{\langle \theta^2_{\mu\nu} \rangle} \approx \sqrt{m_p c^2 / E_\nu}\ [\text{rad}] \tag{2.6}$$

or 1.75° for $E_\nu = 100\,\text{TeV}$ [24]. Because the probability of detection goes up with increasing energy, detected muons will tend to deviate less on average. Thus, AMANDA can resolve the incident path of a muon neutrino with resolution limited by Eqn. 2.6 and the resolution of the muon track reconstruction (described in Chapter 4), which works out to be $\sim 2°$ (see §7.1.2). Although the resolution pales in comparison to an optical telescope (with a typical resolution on the order of arc-seconds), we will see that the present resolution is sufficient to do neutrino astronomy.

2.2 Models & Flux Predictions

Theoretical models to predict fluxes of neutrinos fall into two general categories, *top-down* and *bottom-up*. Top-down scenarios involve neutrino generation via the decay of super-massive theoretical particles such as topological defects, super-symmetric particles, and WIMPs (weakly-interacting massive particles). Bottom-up scenarios involve the acceleration of charged particles to high energies, with neutrinos resulting from the interaction of accelerated hadrons with matter or radiation. Since we are interested primarily in astronomical sources of cosmic rays, only the latter will be discussed further here.

Most bottom-up models rely upon the early suggestion of Enrico Fermi [26, 27] that cosmic rays may be accelerated by scattering across magnetic "mirrors", created by shocks of charged particles associated with objects like supernovae remnants or the relativistic jets of active galaxies (AGN). Models relying on diffusive shock acceleration are shown (for example in [24]) to naturally result in fluxes following power-law energy spectra,

$$\frac{dN}{dE} \propto E^{-\alpha}, \tag{2.7}$$

typically with $\alpha = 2$, which motivates the choice of spectral index for our neutrino signal model, described in §5.1.2.

2.2.1 The Waxman-Bahcall Bound

If we assume there is a connection between the observed cosmic rays and neutrinos, it is possible to deduce a model-independent neutrino flux upper limit based upon cosmic ray observations [28]. As discussed earlier, the cosmic ray spectrum above $E_{\mathrm{CR}} \approx 3 \times 10^{18}$ is dominated by an extragalactic distribution of proton sources. Under this assumption, one can calculate the energy production rate of protons between the range of 10^{19} and 10^{21}eV, $\dot{\epsilon}_{\mathrm{CR}} \sim 5 \times 10^{44}\,\mathrm{erg\,Mpc^{-3}\,yr^{-1}}$ [29]. Then the generation rate of cosmic ray protons is given by

$$E_{\mathrm{CR}}^2 \frac{dN_{\mathrm{CR}}}{dE_{\mathrm{CR}}} = \frac{\dot{\epsilon}_{\mathrm{CR}}}{ln(10^{21}/10^{19})} \simeq 10^{44}\,\mathrm{erg\,Mpc^{-3}\,yr^{-1}}. \tag{2.8}$$

Let us assume that photo-meson interactions, resulting in neutrinos from the decay of charged pions, occur in these sources with some average efficiency, ϵ, before the protons leave the acceleration region. Since the fraction of energy carried by the neutrino is independent of the proton energy, the resulting neutrino energy spectrum would follow proton generation spectrum. One can then use the cosmic ray generation rate to predict the present density of resulting muon neutrinos,

$$E_{\nu}^2 \frac{dN_{\nu}}{dE_{\nu}} = 0.25\,\epsilon t_{\mathrm{H}} E_{\mathrm{CR}}^2 \frac{dN_{\mathrm{CR}}}{dE_{\mathrm{CR}}}, \tag{2.9}$$

where $t_{\mathrm{H}} = 10^{10}\,\mathrm{yr}$ is the Hubble time. The factor 0.25 arises because photo-meson interactions result in neutral pions (and thus no neutrinos) half of the time; the left over half of the energy is shared between muon-neutrinos and electron-neutrinos (see Eqn. 2.2). We then define the maximum muon neutrino intensity (obtained with $\epsilon = 1$),

$$I_{\mathrm{max}} = \eta E_\nu^2 \frac{dN_\nu}{dE_\nu}, \tag{2.10}$$

by introducing the parameter η to account for the possible neutrino contributions of unobserved sources at high redshift, and the effect of redshift in neutrino energy. This parameter is of order unity and varies between $0.6 < \eta < 3$ for different models of neutrino energy evolution with redshift. The maximum flux of muon neutrinos expected from a correlation with cosmic rays, i.e with $\epsilon = 1$, is then given by the Waxman-Bahcall upper bound:

$$E_\nu^2 \Phi_{\nu_\mu}^{\mathrm{WB}} = \frac{1}{2} I_{\mathrm{max}}, \tag{2.11}$$

with approximately equal fluxes expected for ν_μ and $\nu_{\bar{\mu}}$. The Waxman-Bahcall bound for the given range of η is shown graphically in Fig. 2.2.

2.3 Cosmic Accelerators

The Waxman-Bahcall bound is a model-independent upper limit on the total integrated flux from all neutrino sources produced in connection with cosmic rays. Specific models also exist to predict neutrino fluxes from particular classes of objects. This section briefly discusses a few of these classes of objects.

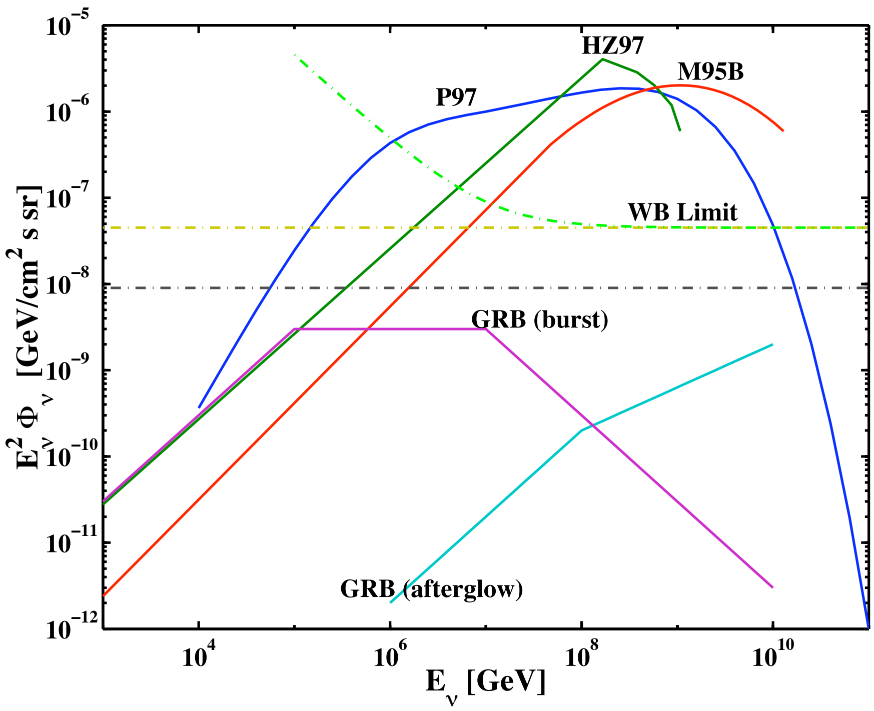

Figure 2.2: The Waxman-Bahcall upper bound on muon neutrino flux intensities ($\nu_\mu + \bar{\nu_\mu}$), derived as shown in the text. The dot-dash line gives the upper bound corrected for neutrino energy loss due to redshift and for the maximum known evolution. The lower line is obtained assuming no evolution. The solid curves show the predictions of the AGN jet models of Mannheim (M95B), Protheroe (P97), and Halzen and Zas (HZ97). From [30].

2.3.1 Active Galactic Nuclei.

To date, TeV γ-emitting blazars are the only confirmed extragalactic accelerators of particles to TeV energies. If a significant portion of the observed TeV photon flux is due to photo-pion production in the jets, then we would expect the corresponding neutrino flux to be of the same magnitude as the gamma ray flux. The Waxman-Bahcall bound would seem to reject this hypothesis, since if neutrinos are routinely produced at a rate comparable to the observed γ-rays, the total flux of neutrinos produced in AGN jets would exceed the Waxman-Bahcall bound [28].

Models also exist for neutrino production in the cores of AGN. If protons are accelerated in the core-region of AGN, the soft photon density in the region must be sufficiently high in order for photo-pion production to occur readily [31]. Under such conditions, TeV gamma radiation does not escape the core, but lower energy radiation in the GeV range does. So while optically-thin TeV blazars may not be the most likely candidates for neutrino production, blazars with substantial GeV gamma-flux may be. The neutrino flux prediction of the core model is compared to the sensitivity of AMANDA-II and other detectors in Fig. 2.3.

2.3.2 Microquasars.

Microquasars are galactic objects thought to consist of an accreting compact object (neutron star or small black hole) fed by companion gas giant. These objects produce radio-observable jets similar to those seen from AGN (also known as quasars), and the mechanisms for the accretion disk and jet formation are thought to be similar to those at play in AGN. With microquasars we have an observational advantage in that they are much closer, in our own galaxy, than AGN.

Some microquasars exhibit persistent radio emission while others radiate intermittently or periodically. The observed radiation is consistent with synchrotron radiation from shocked electrons. During a major ejection event, characterized by an initial rise in X-ray radiation, part of the inner accretion disk is thought to be ejected leading to the formation of an electron-proton jet [32].

A model for neutrino production in e-p microquasar jets has been proposed in [33]. In this model, protons may be accelerated by relativistic shocks in microquasar jets up to an energy of $\sim 10^{16}$eV, and the interaction of these shocked protons with synchrotron photons would lead to 1-100 TeV neutrinos. Using observed microquasar jet parameters, one can make neutrino flux predictions for specific microquasars [32]. The microquasar SS433 is one of the most promising candidates, resulting in a prediction of $252\,\mathrm{yr}^{-1}\,\mathrm{km}^{-2}$ neutrino induced muons in a neutrino detector, which may be marginally detectable by AMANDA-II.

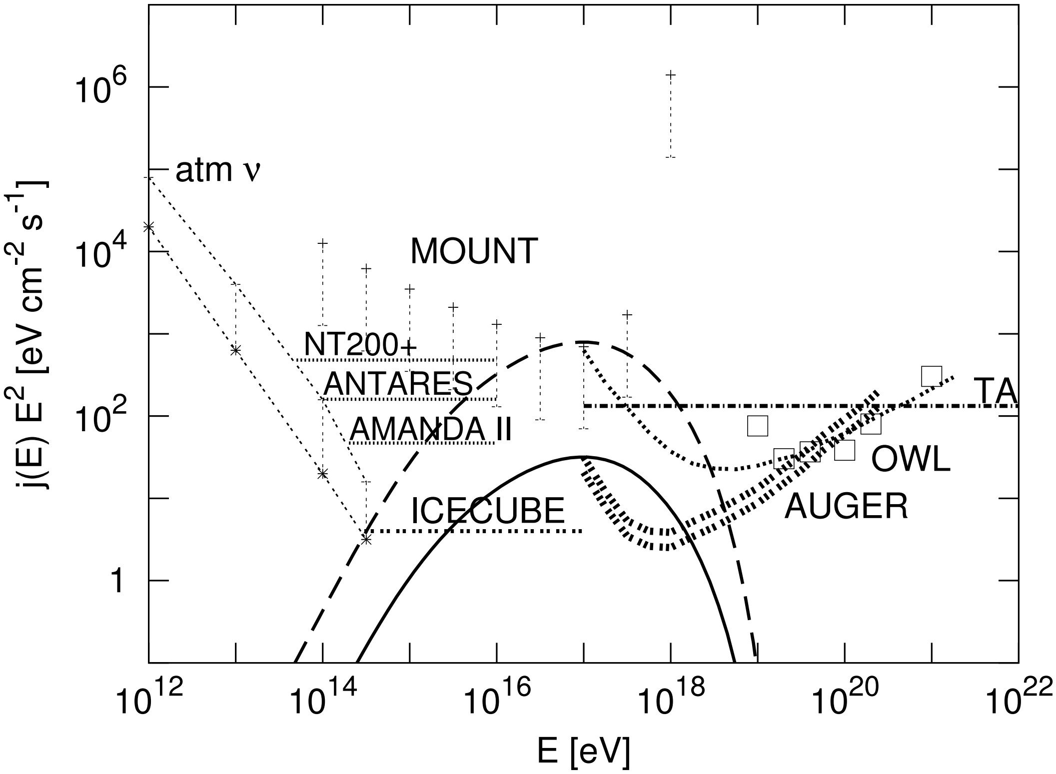

Figure 2.3: Neutrino flux predictions for a typical GeV blazar made using a core-production model. Also shown are the sensitivities of the existing AMANDA-II detector and the Auger [34, 35, 36, 37] air shower array, as well as expected sensitivities of the planned air shower/fluorescence detectors Telescope Array (TA) [38] (dashed-dotted line) and MOUNT [39], the space-based OWL [40] (squares), and water Cerenkov detectors Baikal NT200+ [41], ANTARES [42], and ice-based IceCube [43]. From [31].

2.3.3 The Cygnus-OB2 Region.

An OB region is a cluster of young stars all near the same age. Cygnus-OB2 is a globular cluster in the Milky Way galaxy containing some 2600 OB-type stars, with a total mass of 10^5 solar masses within a compact diameter of about 60 kpc. It is the largest known OB2 cluster in the galaxy and containing some of the most luminous stars of the Milky Way. Located at a distance of 1.7 kpc, it has an angular extent of about 2° in the sky at R.A. $20^h\,33^m$, Dec. $+41^\circ\,12'$ [44].

It has been suggested that turbulent solar winds in such regions might actually be more efficient nucleonic accelerators than lone SNRs [45]. The HEGRA telescope recently detected an extended source of TeV γ-rays near the Cygnus-OB2 region [46]. Follow-up observations in x-ray and radio wavelengths suggest that the gamma rays are indeed the result of nucleonic acceleration in this region [47]. It's proximity and intensity make it a prime candidate for detection in neutrinos.

2.3.4 Transient Sources

One of the most promising candidate sources of high energy neutrinos are Gamma Ray Bursts (GRBs), discovered serendipitously in the 1960s by American *Vela* spy-satellites monitoring for Soviet nuclear tests [48]. The question of the spatial origin of GRBs remained unsettled until the launch of the Burst and Transient Source Experiment (BATSE) on-board the Compton Gamma Ray Observatory satellite. BATSE observed about 8000 GRBs from its launch in 1991 until it was de-orbited by NASA in 2000. The observed isotropy in arrival direction of BATSE detections implies GRBs are extragalactic in origin [49].

GRBs are characterized by a short and intense emission of non-thermal $1\,\mathrm{keV}$ –

1 MeV photons, lasting milliseconds to seconds. At cosmological distances, the observed flux corresponds to a total energy output of 10^{51} to 10^{53} erg per burst. The BATSE detection rate of about 1 per day implies a rate of about one GRB per galaxy per million years [50].

The rise time of the observed light curves suggests that GRBs are associated with the formation of compact objects, most likely black holes. The collapse is thought to be accompanied by a highly relativistic "fireball" of optically-thick electron-positron plasma [50]. The observed gamma rays are produced in optically-thin regions, perhaps by the interaction of the fireball with the external interstellar medium (ISM). Recent observations of x-ray, optical, and radio afterglows associated with GRBs have been taken as evidence to support this model [51, 52].

The total power radiated by GRBs is of the same order of magnitude as the power present in UHE cosmic rays [50], suggesting that GRBs could be a source of the highest energy particles observed above the "ankle" of the cosmic ray spectrum (see Fig. 1.3).

Searches for neutrinos coincident with the GRBs using AMANDA greatly benefit from the spatial and temporal localization of each GRB as provided by the BATSE data, so the GRB analyses are conducted independently of searches for sources of continuous emission. To date, no neutrinos have been detected in association with the BATSE GRB detections [53].

2.3.5 Hidden Sources

All of the aforementioned classes of sources are suggested based on observed photon emission, but as already discussed (in §1.1), we cannot rely on photons to reveal phenomena masked by intervening matter, or existing at the greatest cosmological distances. The history of astronomical discovery is ripe with examples of serendipitous discoveries, from Galileo's first glimpses of the four largest moons of Jupiter, to the first detection of GRBs. As the sensitivities of neutrino telescopes continue to improve, we should not be surprised if new phenomena are revealed.

Chapter 3

AMANDA-II

Over the last decade, the Antarctic Muon and Neutrino Detector Array has evolved from an uncertain proposal into a pioneering instrument of neutrino astrophysics. We begin this chapter by describing the underlying principle of optical Cerenkov radiation detection in §3.1. The geometrical design and layout of AMANDA-II are treated in §3.2. Operation, calibration, and performance are discussed in §3.3 and §3.4.

3.1 Detection Principle

As described previously, the presence of a neutrino must be deduced based on the appearance of a charged lepton from a neutrino-nucleon interaction (Eqn. 2.4). Most relevant to a search for point sources is the reconstruction of the long, tracing signatures of muons as they propagate and emit detectable Cerenkov light.

3.1.1 Optical Cerenkov Light Detection

Relativistic muons propagate in ice with velocity $v \simeq c$, whereas photons propagate in ice with velocity $v = c/n$, where $n = 1.33$ is the index of refraction in ice. When a charged particle travels through a medium with velocity greater than the velocity of light in the medium, a cone of Cerenkov light is emitted. Cerenkov radiation is a well-understood classical electromagnetic shock phenomenon, analogous to sonic shock waves produced when an object (such as a supersonic jet) travels at a speed greater than the speed of sound. The Cerenkov light propagates outward in a cone whose opening angle,

$$\theta_{\mathrm{c}} = \cos^{-1}(1/n\beta) = 41^{\circ} \tag{3.1}$$

where $\beta \simeq c/n$, and can be derived using a geometric argument illustrated by Fig. 3.1.

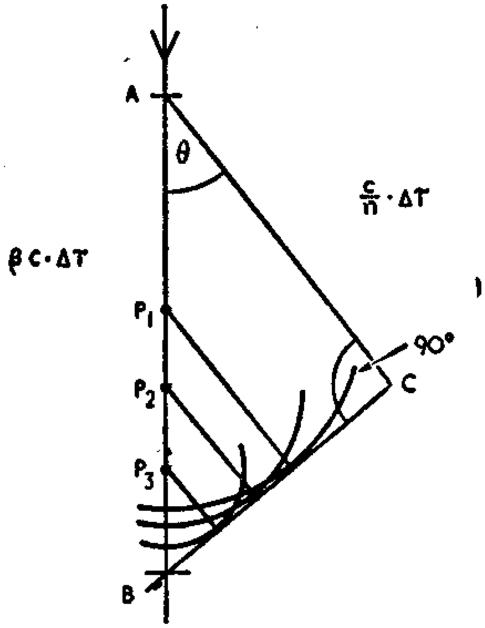

Figure 3.1: The geometric derivation of the Cerenkov angle, Eqn. 3.1. The relativistic muon propagates along path AB. With Cerenkov light wavefronts propagating spherically outward with speed $v = c/n$ from each point along AB, a conical shock-wave, with 2D cross-section BC, is formed by the superposition of the spherical wavefronts.

The intensity of the Cerenkov light is given by the Frank-Tamm formula [54],

$$\frac{d^2N}{dx\,d\lambda} = \frac{2\pi\alpha z^2}{\lambda^2}(1 - \frac{1}{\beta^2 n^2}), \tag{3.2}$$

where z is the charge of the particle. For an icebound Cerenkov detector, the effective wavelength range is $310\text{nm} < \lambda < 500\text{nm}$. Within this wavelength range, a minimum ionizing muon effectively emits $dN/dx \sim 200/\text{cm}$ quanta of radiation, sufficient for detection at a distance of tens to hundreds of meters from the muon track depending on the optical properties of the fiducial volume.

The Cerenkov light is detected by a three-dimensional array of photomultiplier tubes (PMTs), and the path of the muon is deduced based on the pattern of photon arrival times, as depicted in Fig. 3.2. To ensure an accurate muon track reconstruction, the PMTs must have a temporal resolution on the order of a few nanoseconds to achieve a spatial resolution of less than a few meters.

3.1.2 Stochastic Muon Energy Loss

The total energy loss of a muon in ice is about $2\,\text{GeV/m}$ [55]. Cerenkov light represents only a small fraction of the energy deposited by the muon as it propagates. Most of its energy is lost through ionization of the detection medium. Muons are also subject to stochastic energy losses due to bremsstrahlung, electron-positron pair production, and hadronization of nuclei [56]. The relative importance of each process is illustrated in Fig. 3.3. The total energy loss of the muon may be parameterized by

$$-\frac{dE}{dx} = \alpha(E) + E\,\beta(E). \tag{3.3}$$

In ice, $\alpha(E) \approx 0.2\,\text{GeV}\,\text{m}^{-1}$, representing continuous losses, and $\beta(E) \approx 3.4 \times 10^{-4}\,\text{m}^{-1}$, representing stochastic energy deposition, are roughly constant over the

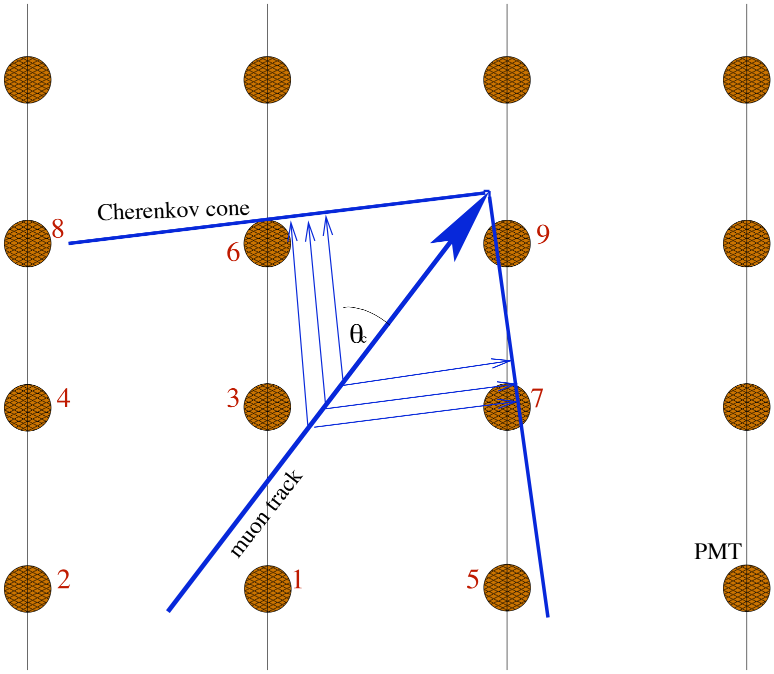

Figure 3.2: Cerenkov light detection by an array of PMTs. In this two-dimensional depiction, the given numbers indicate the order in which individual PMTs observed light from the unscattered Cerenkov cone. This timing information is used to deduce the trajectory of the muon track.

relevant range of energies [55]. Stochastic losses become the dominant mode of energy deposition around $E = 600\,\text{GeV}$.

Stochastic energy deposition is characterized by bright, discrete bursts of Cerenkov light produced by the interaction products. Due to the large forward momentum of the muon, particles produced as a result of stochastic losses are largely constrained to the angular trajectory of the muon, and the resulting Cerenkov light emission peaks around the Cerenkov angle of the muon. Our simulations include this higher-order distortion of the Cerenkov cone [57], but the main effect is to alter the intensity of the Cerenkov radiation.

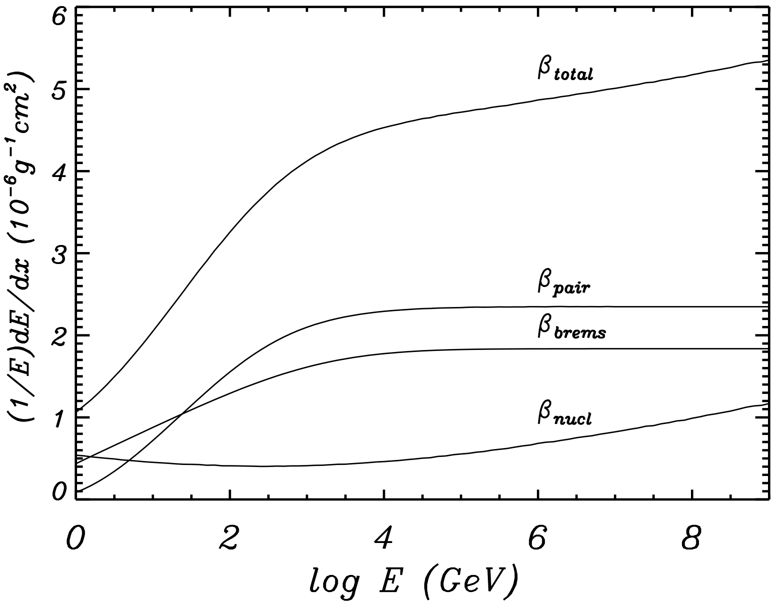

Figure 3.3: The relative contributions to the linear coefficient of muon energy loss (β in Eqn. 3.3) from pair production, bremsstrahlung and nuclear hadronization in rock. The value of dE/dx scales with density, and is thus lower in ice. From [56].

Solving Eqn. 3.3 for the range of a muon with initial energy E_0 yields

$$R_\mu(E_0) \approx \frac{1}{b} \ln \left(\frac{bE_0}{a} + 1 \right) \tag{3.4}$$

As seen in Fig. 3.4, a simulation of muon propagation reveals that the analytic solution systematically overestimates the muon range at higher energies.

3.2 Detector Design

3.2.1 Optical Modules

An AMANDA optical module (OM) consists of a light-sensitive 8" Hammamatsu photomultiplier tube encased within a glass pressure vessel, pictured in Fig. 3.5. The photo-sensitive area of the PMT is adjoined to the glass housing by an optically

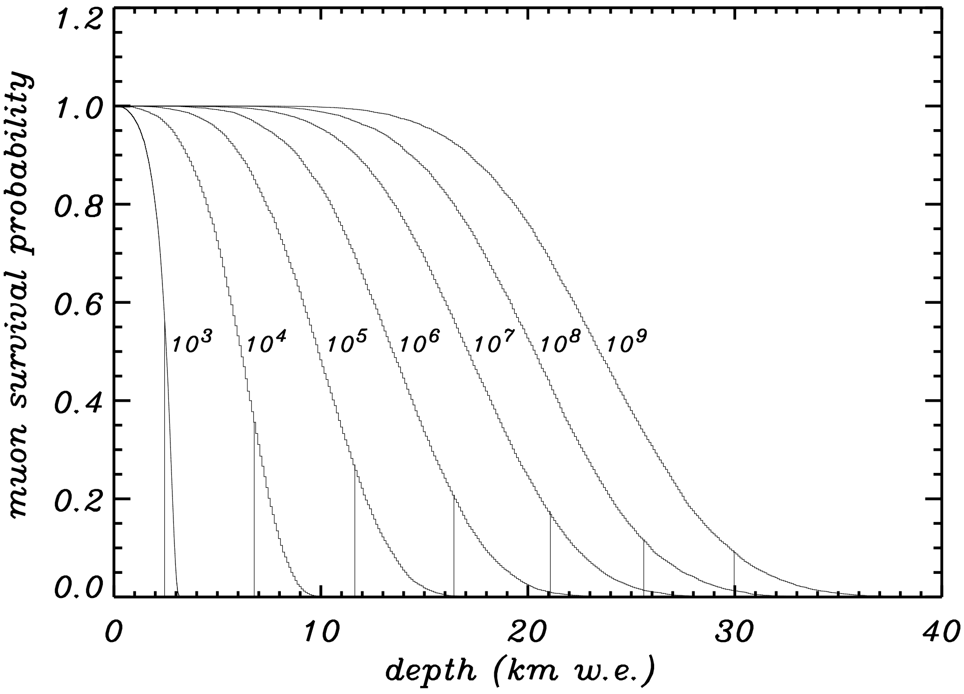

Figure 3.4: The muon survival probability in rock vs. the muon range (measured in kilometers of water equivalent) and initial muon energy (in eV). The vertical lines indicate the values of the analytic solution to Eqn. 3.4. From [56]

conducive gel, and the glass housing is made of purified glass to ensure low noise from radioactivity. The PMTs are run at high gain and have dark noise rates ranging between $\sim 500\,\mathrm{Hz}$ and $1\,\mathrm{kHz}$.

Several evolutions of OM technology have been deployed during construction of AMANDA-II. Four methods to transmit the PMT pulse to the surface have been tested, including coaxial cable, twisted pair, fiber optic, and digital transmission. Each method presents its own set of advantages and drawbacks, which are contrasted in Table 3.1. Digital optical modules (DOMs), were the last to be deployed during the completion of the AMANDA-II array. Each DOM contains its own data acquisition electronics and has the capability to digitize and record PMT waveforms for

Technology	Dispersion	X-talk	Cable bulk	Reliability	Cost
Coaxial	-	+	-	+	+
Twisted-pair	-	-	+	+	+
Fiber optic	+	+	-	-	-
Digital	+	+	+	+	-

Table 3.1: A comparison of advantages and drawbacks associated with each of the four OM technologies. From left to right, a rating of "+" indicates the positive traits of little or no pulse dispersion, no electrical cross-talk, manageable cable bulk, deployment reliability, or affordability.

asynchronous electrical transmission to the surface. Further refined DOM technology will be employed in the future IceCube neutrino observatory (discussed in §8.2.1).

3.2.2 Geometry

The price-tag of a neutrino telescope is proportional to the number of optical detectors deployed. A compact layout of sensors would provide good angular resolution and a low energy threshold, but would be limited in detection volume, such as in the case of the Super-K detector [58]. To increase the detection rate of rarer high-energy events, we must deploy our limited number of sensors more sparsely, sacrificing (to some extent) the angular resolution and increasing the energy threshold.

AMANDA-II consists of a three-dimensional array of 670 OMs deployed at regular intervals along 19 cables, or "strings," between depths of 1500 and 2000 m, as portrayed in Fig. 3.5. The strings are spaced along three concentric circles separated by 30 to 60 m, the outermost circle having a diameter of 200 m. On the inner four strings, the OMs are vertically spaced by intervals of 20 m, with 10 m spacing between most of the OMs on other strings. It is found that a muon track must be at least $\sim 100\,\mathrm{m}$ in length to result in enough photon detections to ensure an accurate track reconstruction. The minimum-ionizing muon energy deposition rate of $\sim 0.2\,\mathrm{GeV\,m^{-1}}$ (Eqn. 3.3) thus implies a detectable energy threshold of $E_\mu >\sim 50\,\mathrm{GeV}$, or $E_\nu >\sim 100\,\mathrm{GeV}$.

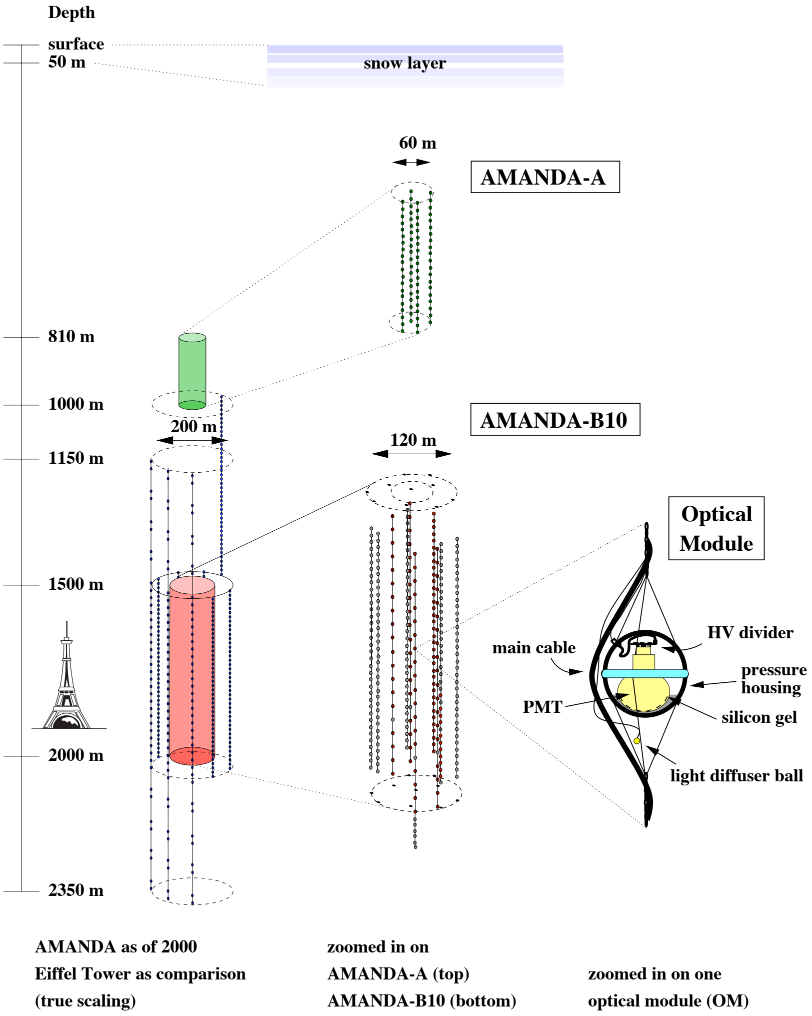

Figure 3.5: The schematic of the AMANDA-II layout.

3.2.3 Ice Properties

The success of muon track reconstruction relies in part on the extent of our knowledge of the optical properties of the fiducial ice. The relevant properties have been studied extensively using *in situ* light sources [59]. The fiducial volume is found to contain dust layers which contain a record of past climate change, as evidenced by the measured scattering length vs. depth shown in Fig. 3.7. The AMANDA OM spacing corresponds roughly to the average scattering length $\sim 20\,\mathrm{m}$ for Cerenkov photons in the fiducial ice. The absorption length is found to be on the order of $100\,\mathrm{m}$. The measured optical properties of the ice are modeled in the detector simulation, which is discussed further in §3.4.1.

The situation is reversed for underwater detectors such as Baikal and Antares, where the scattering length is longer than the absorption length. This implies the potential for better angular resolution. However, the longer photon absorption length in ice increases the effectiveness of calorimetry and leads to better energy resolution in AMANDA. In this sense, under-ice and underwater detectors are complementary instruments.

3.3 Detector Operation

3.3.1 Data Acquisition

Electrical or optical signals are transmitted to the surface and amplified by Swedish amplifiers (SWAMPs), digitized by discriminators, and then counted by the digital multiplicity adders (DMADD). The time digital converter (TDC) records the leading (LE) and falling edge time of each PMT pulse that satisfies a preset amplitude threshold. The TDC has a buffer depth of 8 pulses and time window of $32\,\mu s$. When the detector is triggered, a stop signal is sent to the TDC and pulses in the buffer are read out. The LE time and time-over-threshold (TOT) is recorded for each pulse, and the largest amplitude (assigned by the analog to digital converter, or ADC) in the buffer is assigned to the first pulse. Most hits in AMANDA correspond to just one pulse; if there are multiple hits in a channel, the first is most likely to have the largest amplitude. The detector is triggered when a certain pre-set number of channels (OMs) register photon hits within a given time window. The "majority trigger", requires hits on at least 24 OMs within a time window of $2.1\,\mu s$.

When the TDC is stopped, read out and then reset, the DAQ experiences a certain amount of "dead-time", when new data cannot be recorded. The fraction of dead-time experienced must be subtracted from the total acquisition time to yield the detector's effective live exposure time. The dead-time is determined by plotting the distribution of the time between events, Δt above a cut-off time of t_{cut} (chosen to be 10 ms), which perfectly follows an exponential parameterization,

$$f(x;\tau) = \frac{1}{\tau} e^{-x/\tau} \tag{3.5}$$

where $x = \Delta t - t_{\text{cut}}$. The ideal trigger rate (no dead-time) is then given by $R_{\text{ideal}} = 1/\hat{\tau}$ where $\hat{\tau}$ is the mean of the distribution. Comparing to the observed trigger rate, R_{obs}, we may estimate the dead-time fraction, D, as

$$D = \frac{R_{\text{ideal}} - R_{\text{obs}}}{R_{\text{ideal}}} = 1 - R_{\text{obs}}\hat{\tau} \tag{3.6}$$

The result is independent of the arbitrary choice of t_{cut} within the range $5\,\text{ms} < t_{\text{cut}} < 25\,\text{ms}$ [60]. For the year 2000, the dead-time fraction is estimated at 16.8% [61].

3.3.2 Seasonal Calibration

Each austral summer, adjustments and upgrades are made to the AMANDA electronics. As part of this cycle of routine maintenance, characteristic hardware settings for each channel are recorded for use in the detector simulation. Most of the yearly calibration effort is spent measuring the signal delay time, or t_0, for each OM. The t_0 values depend not only upon the length of cable between the OMs and the surface, but also upon the time for the signal to be processed by the DAQ electronics. Since the DAQ hardware or settings often changes from year to year, the t_0 calibration must be performed every year after DAQ upgrades take place.

Another calibration value essential to the proper modeling of detector performance is is the relative threshold of the PMT pulse discriminator, typically measured in fractions of a photo-electron (p.e.). The pulse discriminator is set at a fixed value measured in millivolts, but the number of millivolts corresponding to one p.e. varies by channel and from year to year with changes in the DAQ electronics. These values are often not measured each year, but, as described in appendix A, can be extracted later by examining the ADC and TOT distributions for each channel.

3.3.3 Electrical Cross-talk

Strings 6-10 communicate with the counting house via twisted-pair cables, which introduces the possibility that signals from one PMT may be picked up in the cable of another, registering false hits. Pulses resulting from cross-talk are easily distinguishable from real hits in a plot of ADC (amplitude) vs. TOT (pulse width), demonstrated in Fig. 3.6.

Cross-talk is an unsimulated effect, so if we wish to compare our data to the the results of a simulation we must remove the erroneous cross-talk hits from the data at a relatively early stage in the analysis. A cross-talk hit filter has been developed which rejects hits that fall to the left of a fit to the edge of the ADC-TOT region

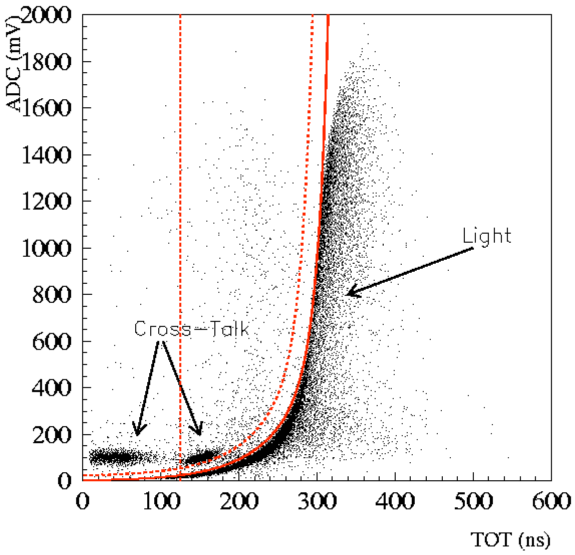

Figure 3.6: The identification of cross-talk hits in a plot of ADC vs TDC. for the hits on a given OM. From [62]

corresponding to real hits.

3.4 Performance

Having described the operating principles and practical design of AMANDA-II as a particle detector, we now focus on the performance characteristics vital to its operation as a neutrino telescope, namely the ability to detect and accurately pin-point astrophysical neutrino sources. Taking on such a task in the absence of an artificial calibration beam, or a naturally occurring "standard candle" of high energy neutrinos, our understanding will necessarily rely upon computer simulations of both the neutrinos and the detector's response. Here we will concentrate only on the detector's response to simulated leptons (especially muons), leaving a description of the neutrino signal simulation for §5.1.2.

3.4.1 Detector Simulation

Muon (and tau) propagation is simulated using a new java program dubbed *Muon Monte Carlo* (MMC) [63]. The code is very efficient, precise, and incorporates all of the latest measured cross sections for the lepton energy loss processes described in §3.1.2. Propagation of Cerenkov photons is simulated using the program *Photon Transport and Detection* (PTD). The program tabulates photon survival probabilities vs. photon trajectory in a coordinate system compatible with the detector simulation, AMASIM, which simulates the detector hardware.

Unfortunately, the optical properties of the fiducial ice are not uniform with depth, which complicates the photon propagation simulation. The PTD software works by tabulating photon survival probabilities under one given set of ice properties at a time. This means that individual photons may not be tracked continuously between regions having different optical properties. The situation is approximately modeled by separately tabulating photon survival probabilities for thin layers of ice ($\sim 10 - 25\,\mathrm{m}$ thick) with the average optical properties at that depth, as illustrated in Fig. 3.7. Each Cerenkov photon is then assumed to propagate under the conditions in the layer in which it is detected. This approximation suffices quite well for "direct photons," which are detected near the muon track, but can lead to problems when examining late arriving photons which may have crossed more than one vertical layer. If the actual measurements of absorption are used as the input for the layered simulation, disagreements are found when comparing predictions from the simulation with atmospheric muon observations. In particular, the simulation predicts a higher number of muon events exhibiting higher channel multiplicities (the number of of channels triggered per event).

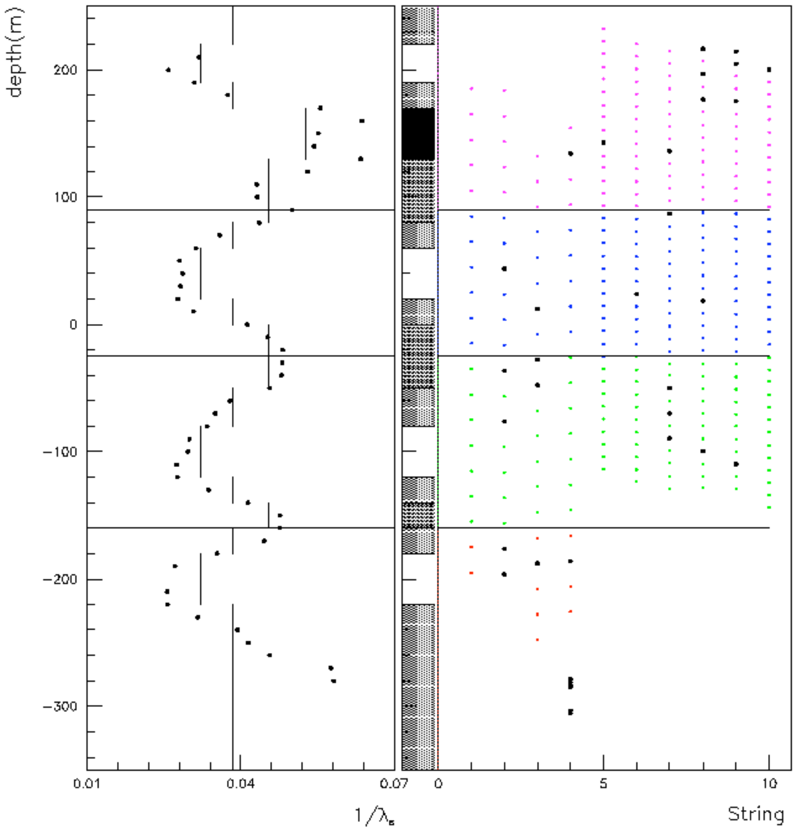

Figure 3.7: The effective (inverse) scattering length, $1/\lambda_s$ (m^{-1}), vs. depth in detector coordinates. The locations of OMs on the first 10 strings of AMANDA are shown on the right. The vertical bar describes how the ice properties are included in one version of the detector simulation; the shaded boxes correspond to regions where the ice is simulated with different fixed values of λ_s as indicated by the vertical lines in the left inset. Modified from [64].

A more detailed examination reveals that these discrepancies originate from a disagreement in the number of "late" hits (from highly scattered photons), with more late hits predicted than observed, suggesting that the model underestimated the effective absorption. Given the limitation of the photon transport simulation, as well as other unsimulated effects such as scattering by the refrozen "hole-ice", it is no surprise that these discrepancies arise. To correct the problem, a more sophisticated photon propagation code, PHOTONICS, is being developed. In the meantime, the layered-ice model has been improved by calibrating the optical properties of each layer to the *effective* absorption lengths seen by photons traveling across all ice layers. This is achieved by correcting the assumed absorption by the ratio of late photon hits predicted vs. observed in the down-going muon data. The resulting *Muon Absorption Model* (MAM) achieves excellent agreement in the previously problematic distributions [65].

3.4.2 Experimental Lepton Signatures

The experimental signature of a muon event is displayed in Fig. 3.8(a). Based on comparisons to simulation, the event shown is likely a muon resulting from the interaction of an upgoing atmospheric neutrino, obtained from the final search sample of this analysis (described in §7.1). The event shown in Fig. 3.8(b) is characteristic of an electromagnetic shower, most likely originating outside the detector from the decay of a down-oing atmospheric muon. The electron ranges out in less than a few meters, producing a bright, point-like emission quasi-spherically propagating Cerenkov light.

A tau neutrino interaction is characterized by bright flash of light from the hadronic cascade at the interaction vertex of the tau, and a second hadronic cascade upon the tau's decay. Even though the lifetime of the tau is relativistically dilated, at energies $E < 10\text{TeV}$ the tau travels a short distance of only 10s of meters before decaying, and would be hard to distinguish from an electromagnetic shower. At energies above $\sim 1\,\text{PeV}$, the tau will travel a few hundreds of meters, emitting a faint

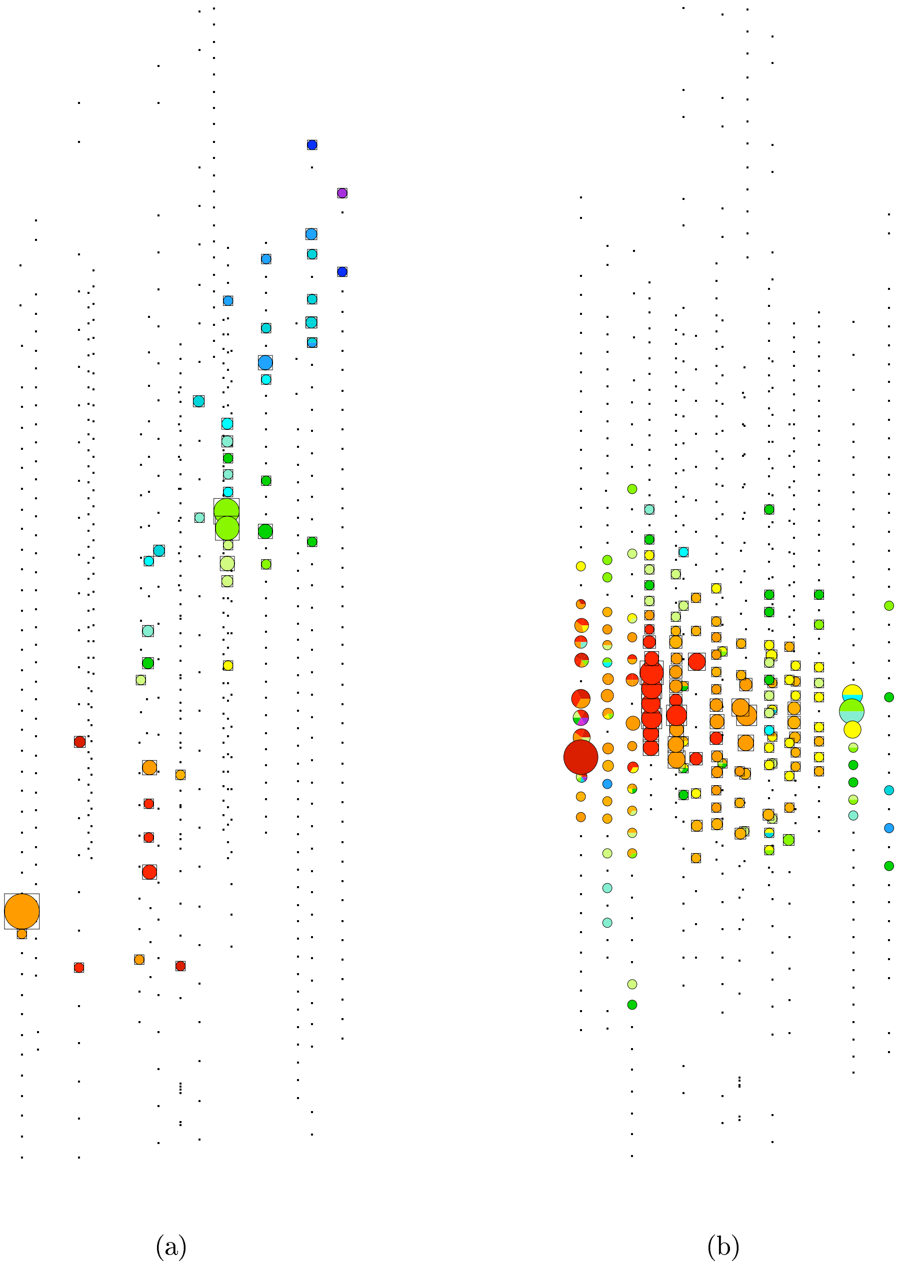

(a) (b)

Figure 3.8: Experimental signatures of a muon track (a), and an electron-positron shower resulting from a high energy electron (b) recorded with AMANDA-II in the year 2000. The color indicates the relative timing, with red hits recorded first and purple hits recorded last. The size of the bubbles is proportional to the number of observed photo-electrons detected.

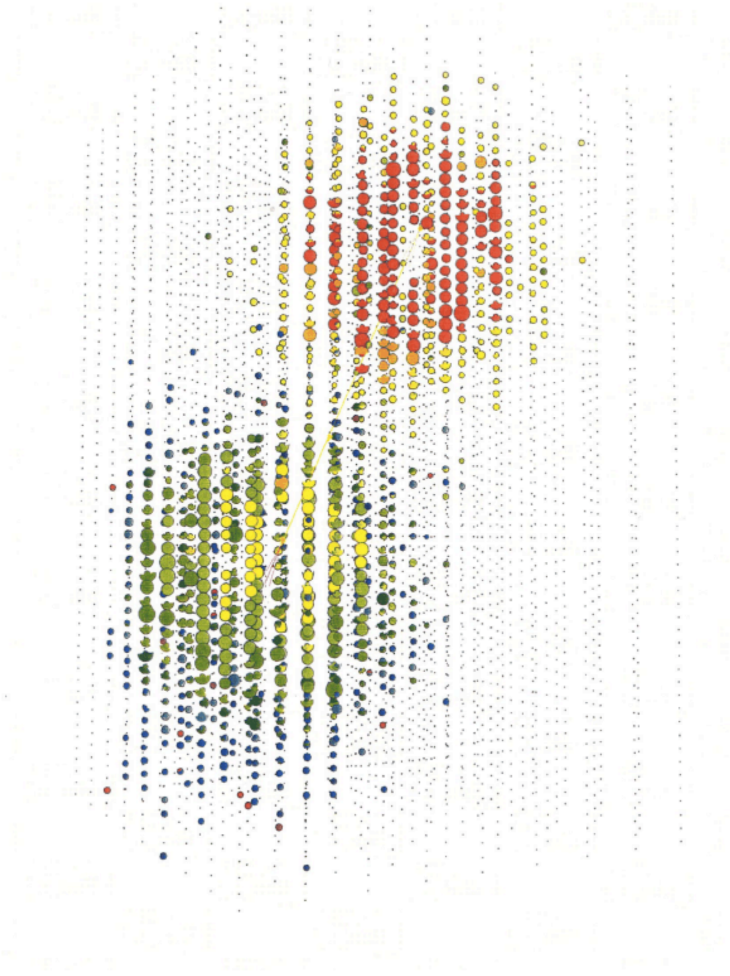

Figure 3.9: The characteristic "double-bang" signature of a 10 PeV tau-neutrino interaction in the future IceCube detector. From [64].

Cerenkov cone, before producing a second flash of light upon its decay. This characteristic "double-bang" can not be contained within the AMANDA volume, but would be possible to distinguish in the future IceCube neutrino observatory, illustrated in Fig. 3.9.

3.4.3 Angular Pointing Offset

Of particular importance for a point-source search is the detector's angular pointing resolution, as it defines what a "point" sources will look like in AMANDA. Simulations suggest that a neutrino signal may be reconstructed with resolutions between 1°and 3° depending on declination and quality cuts (see §7.1.2). However, simulation does not allow us to test for the existence of a systematic pointing offset. We are afforded the unique opportunity to test the absolute pointing accuracy in one particular direction using down-going muons triggered in coincidence with the South Pole Air Shower Experiment (SPASE) [66], located on the surface above AMANDA at a declination of 88°. Both SPASE and AMANDA independently reconstruct the directions of muons from down-going cosmic ray showers.

By comparing the results of the two reconstructions, muon events were found to be systematically mis-reconstructed too steeply (i.e. with higher zenith angle) by less than 1°. AMANDA-II shows improvement over the smaller 10-string array, AMANDA-B10, which demonstrated an absolute pointing error of up to 1.5° [67]. The effect of systematic offsets of 1° or less were studied, with simulations revealing the loss of signal in a typical bin (in the search optimized in §7.2) to be less than 5%.

Chapter 4

Maximum Likelihood Reconstruction & Background Rejection

A good understanding of the reconstruction methods used by AMANDA is helpful before an experimental search for point-sources is conducted. Atmospheric muons trigger AMANDA at a rate of $\sim$ 100 Hz whereas up-going atmospheric neutrinos trigger the detector at rate of only 10 s per day. This means that the reconstruction must not only be accurate; it must be robust if we are to have any hope of achieving a background rejection of better than 10^{-6}.

This analysis takes advantage of a relatively new technique – Bayesian reconstruction – which directly accounts for the known atmospheric muon background to help assess the overall quality of each event. This chapter describes the maximum likelihood reconstruction techniques used in the point-source analysis with emphasis on understanding the power of the Bayesian technique via an exploration of the likelihood-space.

4.1 Likelihood Functions

First, some definitions. As was shown in Fig. 3.1, muons emit Cerenkov photons in a cone with angle $\theta_c = 41°$. Each triggered OM registers the arrival time, t_{arr}, of the first photon hit in an event. Under the assumption of a given track hypothesis H, we may then define t_{geo} as expected geometric arrival time of a photon traveling a distance d from the muon track to the OM,

$$t_{\mathrm{geo}} = \frac{dn}{c}. \tag{4.1}$$

For a photon arriving at and triggering an OM at time t_{arr}, we define the *time residual*,

$$t_{\mathrm{res}} = t_{\mathrm{arr}} - t_{\mathrm{geo}}. \tag{4.2}$$

Photon hits with small time residuals are called *direct hits*, and are assumed to be nearly unscattered. It is possible, even if the track hypothesis is good, to obtain negative residuals, or early hits, either due to an uncertainty in t_{arr} of σ_{PMT} due to the finite timing resolution (nominally 10-15 ns) of the photomultiplier tube, or due to noise hits. Using these definitions, one can define a simple likelihood function,

$$\mathcal{L} = 1 - \frac{1}{N_{\mathrm{hit}}} \sum_{i}^{N_{\mathrm{hit}}} \frac{t_{\mathrm{res}}^2}{\sigma_{\mathrm{PMT}}^2}. \tag{4.3}$$

We may then vary the track hypothesis H such as to maximize $\mathcal{L}$. This would be equivalent to geometric χ^2 minimization.

4.1.1 Timing Likelihood

In practice, the simple χ^2 minimization technique demonstrates poor angular accuracy and little rejection power. This is because in reality the Cerenkov photons are absorbed and randomly scattered by the ice, so the expected arrival time is smeared into a probability distribution of expected time residuals, $P(t_{\text{res}})$, shown in Fig. 4.1. A more useful likelihood function can then be constructed as

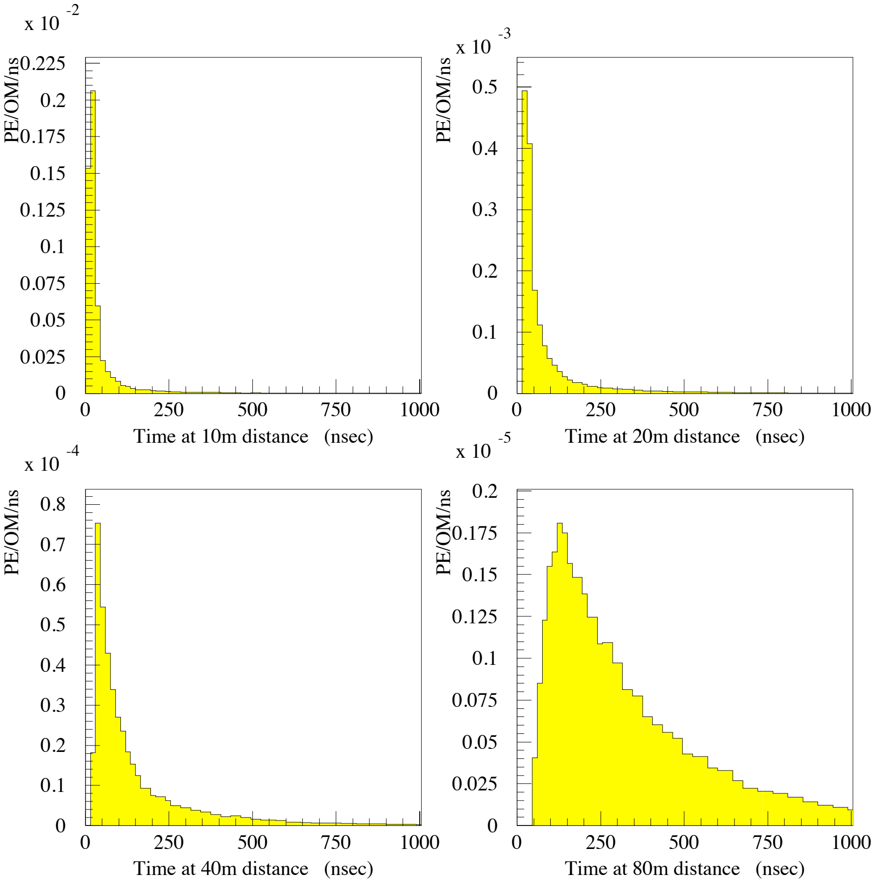

Figure 4.1: The expected distribution of time residuals for a given OM at various distances from a simulated minimum ionizing muon. The photon density is given in terms of photoelectrons (p.e.). From [68].

$$\mathcal{L}(R|H) = \prod_{i}^{N_{\text{hit}}} P_i(t^i_{\text{res}}|d_i, \eta_i). \tag{4.4}$$

where $\mathcal{L}(R|H)$ is taken to be the likelihood to observe a response R of the detector to track hypothesis H. The function P is more generally a function of the distance d_i from and OM orientation η_i relative to the trajectory of the muon track hypothesis.

A detailed photon propagation simulation is used to tabulate values of $P_i(t^i_{\mathrm{res}}|d_i, \eta_i)$ at various distances and orientations relative to a muon track [69]. The raw output of the photon tables is not usually used directly, but rather is parameterized by a smoothly varying analytic expression called the *Pandel function* [70]. Unfortunately, it was not known until recently [71] how to convolve the uncertainty σ_{PMT} into the Pandel function, and for this reason the function diverges near $t_{\mathrm{res}} = 0$. To overcome this difficulty, a kludge is used to "patch" the function with a third degree polynomial and half-Gaussian of width σ_{PMT} near the origin [72]. Despite the crude approach, the Pandel function works quite well with the available minimizers, and the absolute value of the likelihoods calculated using the patched Pandel function compare well with likelihoods computed using the raw output of the photon tables in the vicinity of the likelihood minimum.

4.1.2 Other Likelihood Functions

It should be noted that the timing likelihood function introduced in the previous section is a simplification of what should be possible: a more general likelihood function taking into account all, or at least more of, the available information. In the timing likelihood, information such as the amplitude (ADC) and length (TOT) of the individual PMT pulses is not used. Furthermore, the product in Eqn. 4.4 extends only over *hit* OMs, but we should not forget (especially in AMANDA) that null observations can also lend useful information. We might therefore more generally write

$$\mathcal{L}(R|H) = \prod_i^{N_{\mathrm{om}}} \prod_j \mathcal{L}_{ij}(R_j|H) \tag{4.5}$$

where we have accounted for the likelihoods of all possible OM-wise observables, j. For example, one may seek to incorporate the probability of an OM to *not* be hit, which is also calculable using the photon densities appearing in Fig. 4.1.

The number of observables j we may successfully incorporate into a useful likelihood function is limited by the precision with which the individual likelihood functions, $\mathcal{L}_{ij}(R_j|H)$, are parameterized. As noted in Appendix F of the thesis of T. DeYoung [64], if only small imprecisions exist in the likelihood function, they will be greatly compounded to high powers by Eqn. 4.5. Indeed, efforts to incorporate the *no hit* probability into the likelihood fail, perhaps for this reason. By summing over all modules, especially those far from the track hypothesis, we are using the tails of the distributions of $P_i(t^i_{\text{res}}|d_i, \eta_i)$ where the Pandel-based parameterizations may be seen to differ from the PTD tabulation by nearly a factor two as close as 50 m from the muon track.

4.1.3 Photon Table Likelihood Functions

To further investigate the problem, likelihood functions calculated directly from the output of the PTD tables have been implemented. If our table-based likelihood function is to be minimized, it must vary smoothly in all parameters. For this reason the multidimensional, binned output of the tables must be interpolated. A simple linear interpolation in each dimension was coded into the PTD reader, and an interface between the reader and reconstruction program RECOOS were implemented. The resulting table-based reconstruction was useful in elucidating the problematic behavior of the Pandel function when calculating likelihoods of the most unlikely tracks. Unfortunately, the overall performance of the table-based reconstruction was not as robust as when using the Pandel parameterization. Even with linear interpolation of the PTD output, the resulting table-based likelihood-space might not have been smooth enough to compete with the smooth, analytic Pandel likelihood.

4.1.4 Minimization

In AMANDA, we currently assume that all muon events are through-going, so a track hypothesis is fully defined by a vertex (x, y, z) and a trajectory (θ, ϕ). Usually after seeding with a fast first guess, the track parameters are systematically varied to search for the track hypothesis with the maximum likelihood. In practice, one *minimizes* $-\log(\mathcal{L})$, so that the products appearing in Eqns. 4.4 and 4.5 become an easier-to-handle sum. Two minimizers are commonly used in AMANDA data analysis, Powell's method, and the Simplex method [73]. Both only work when the likelihood function varies smoothly with small changes in the hypothesis. For this reason, likelihood functions based on analytical parameterizations (such as the Pandel function) usually deliver the best performance. Both minimization methods also have a tendency to occasionally become trapped in regions containing local minima. To overcome this behavior, the minimization is often repeated several times seeded with a "grid" of random first-guesses.

4.2 Likelihood-space

To better our understanding of likelihood minimization, it is instructive to investigate the shape of the likelihood-space for a typical event. Shown in Fig. 4.2 is an up-going muon event taken from the final search sample of this analysis. We are most interested in the behavior of the likelihood versus the track trajectory (θ, ϕ) of the hypothesis, so we compute the likelihood of various randomly chosen trajectories, while minimizing out the track vertex (x, y, z). A projection of the resulting two-dimensional likelihood-space onto the θ-axis is shown in Fig. 4.3. The most likely up-going hypothesis (with reconstructed $\delta \simeq 52°$) corresponds to the sharp, global minimum on the right side of the plot. The best down-going hypothesis (obtained

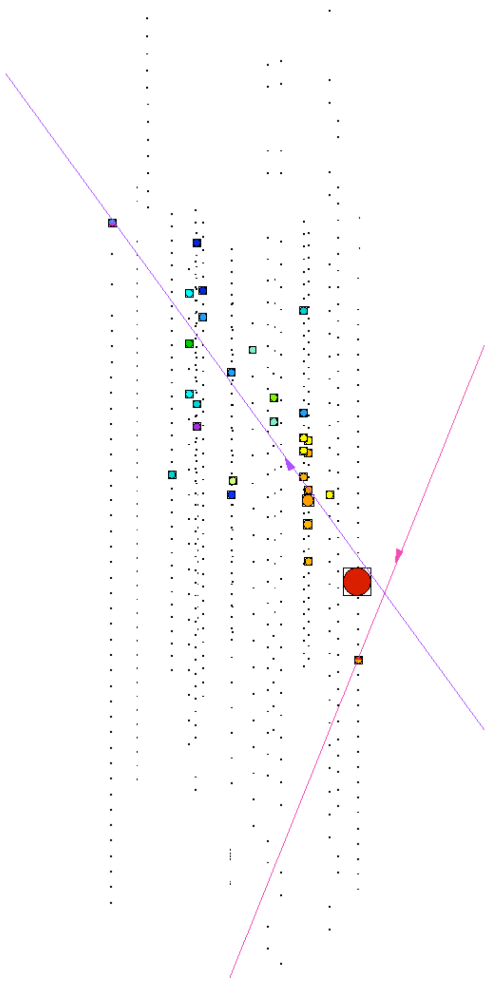

Figure 4.2: Shown is a typical up-going muon event from the final sample of this analysis. Red hits were recorded first and purple hits last. The purple line indicates the most likely up-going track hypothesis; red indicates the most likely down-going hypothesis.

from a search restricted to $\delta < 0$) corresponds to the local minimum near $\delta = -55°$. The quality of the event is evidenced by both the sharpness of the global minimum, as well as the large difference in $\log \mathcal{L}$ between the best up-going and best down-going hypotheses.

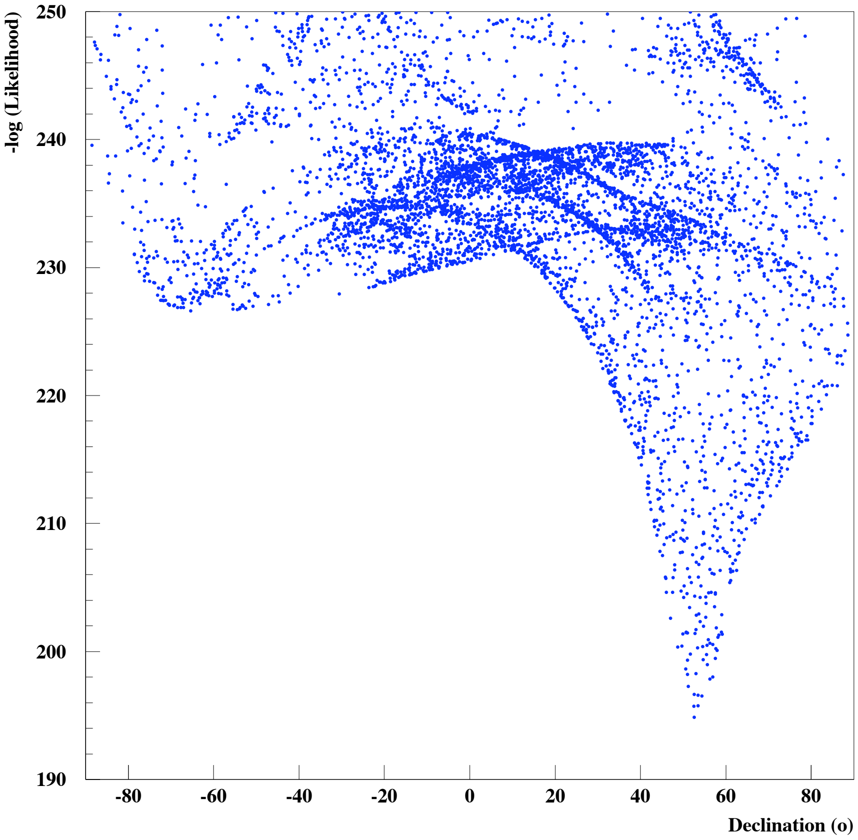

Figure 4.3: A projection of $-\log \mathcal{L}$ for the event pictured in Fig. 4.2, as described in the text.

4.2.1 Bayes' Theorem

It is a common misperception that the track hypothesis $\hat{H}$, having the maximum likelihood $\mathcal{L}(R|\hat{H})$ (or minimum in $-\log\mathcal{L}$) is the most likely track hypothesis to have produced the given data R. It *sometimes* is, but in reality $\mathcal{L}(R|\hat{H})$ contains no information about the likelihood of $\hat{H}$, but rather the likelihood to observe R taking $\hat{H}$ *as a given.* Of course, what we are really after is the probability that $\hat{H}$ describes the actual muon that resulted in the observed response, R.

Suppose we knew, hypothetically, that a given track hypothesis H' is not physically allowed. Then we should be able to say, even if $\mathcal{L}(R|H')$ is large, that $\mathcal{L}(H'|R) = 0$. To say that H' is "not physically allowed" indicates that we have outside information which we would like to incorporate into our likelihood assessment. In AMANDA, all track hypothesis are physically allowed, but more generally we know that hypotheses naturally occur with varying probability $P(H)$. It is well-established that down-going muons from cosmic rays trigger the detector much more frequently than up-going neutrino-induced muons. If our reconstruction mistakenly identifies just one per million atmospheric muons as up-going, our background rejection would fail. In the context of likelihood-space, if the difference in $\mathcal{L}(R|H)$ between the best up-going and best down-going hypotheses is small, it might seem unclear as to whether the event should be considered an up-going neutrino-induced muon, or a down-going atmospheric muon.

The question is, how do we mathematically incorporate our prior knowledge into our likelihood assessment? To find the answer, we draw upon the realm of conditional probabilities and inference logic, which has as one of it's cornerstones a theorem written by the 18th century mathematician Rev. Thomas Bayes:

$$\mathcal{L}(H_{\mathrm{i}}|R) = \frac{\mathcal{L}(R|H_{\mathrm{i}})P(H_{\mathrm{i}})}{\int_H \mathcal{L}(R|H')P(H')dH'}. \tag{4.6}$$

The theorem expresses the *posterior probability* $\mathcal{L}(H_{\mathrm{i}}|R)$, the likelihood of the hypothesis accounting for our prior knowledge. In AMANDA, down-going hypotheses essentially receive an additional weight according to their relative frequencies, which is dependent only on zenith: $P(H) = P(cos\theta)$, appearing in Fig. 4.4. The posterior probability is normalized by an integration over all allowed hypothesis.

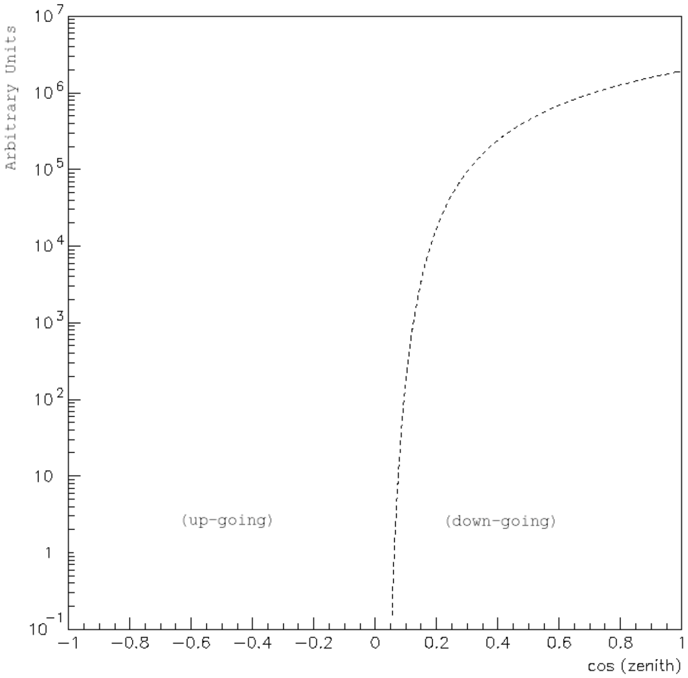

Figure 4.4: The shape of the atmospheric muon prior $P(\cos\theta)$, expressing the relative frequency of different track hypotheses as measured at the center of AMANDA. In practice, the normalization is left to vary freely as a cut-parameter (as described in §4.2.2).

The Bayesian technique is especially useful in assessing the directionality of

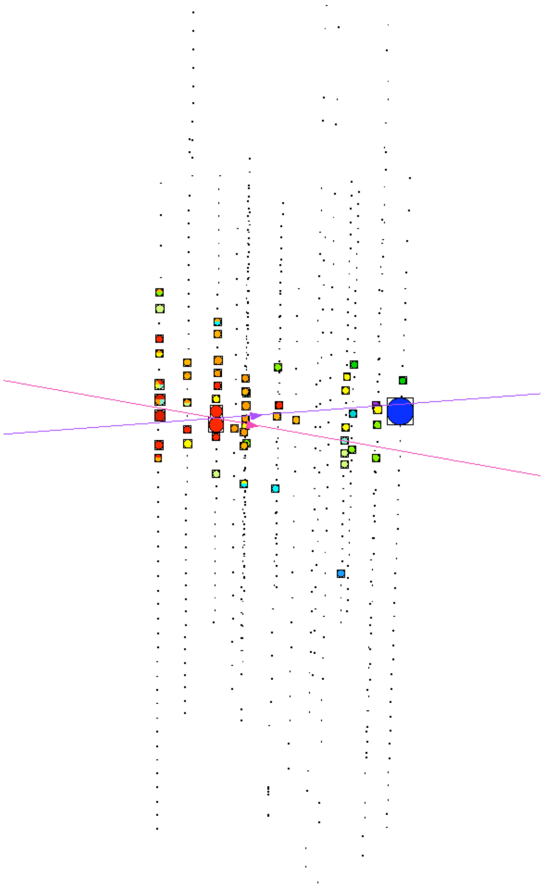

Figure 4.5: Shown is a near-horizontal muon event in AMANDA-II from the year 2000. The purple line indicates the most likely up-going track hypothesis; red indicates the most likely down-going hypothesis.

near-horizontal events, like the one shown in Fig. 4.5. Certainly by eye it is difficult to conclude whether this event is up-going or down-going. An inspection of the likelihood-space of this event, portrayed in Fig. 4.6, demonstrates the incorporation of the atmospheric muon prior. Shown in blue is the unbiased timing likelihood, $\mathcal{L}(R|H)$. Several broad local minima may be discerned in this projection, with similarly broad global minimum near $\delta = +7°$. Overlaid in red is the posterior likelihood with atmospheric muon prior, $\mathcal{L}(R|H)P(H)$. For $\delta > 0$, the two likelihoods map out identical surfaces, because the $P(H)$ is nonzero only for $\delta < 0$. A rather sharp discontinuity appear to be present at $\delta = 0$, due to the sharp onset of $P(H)$. The fact that the red surface reaches lower than the blue at negative declination suggests that we might better consider this event more likely a down-going atmospheric muon. Notice that at the highest negative declinations the two surfaces are the same, just vertically offset. The Bayesian technique essentially gives the down-going hypotheses a handicap, or preference, which varies by declination.

4.2.2 Up/down Probability

Under the hypothesis that all track are either up-going neutrino-induced muons or down-going atmospheric muons, we can compare the probability that an observed pattern of hits was actually up-going (or down-going) by appropriately integrating the likelihood space:

$$\begin{aligned} P_{\mathrm{up}} &\sim \int_{-1}^{0} \mathcal{L}(R|H(\theta))\, P(\cos\theta)\, d\cos(\theta) \\ P_{\mathrm{down}} &\sim \int_{0}^{1} \mathcal{L}(R|H(\theta))\, P(\cos\theta)\, d\cos(\theta). \end{aligned} \tag{4.7}$$

Here we have left out the normalization (which is the same as in Eqn. 4.6) because what we are really interested in is the *ratio* $P_{\mathrm{up}}/P_{\mathrm{dwn}}$, in which the normalizations cancel. In practice, it would be CPU intensive and impractical to perform the integrations of Eqn. 4.7 for every event. However, if we assume that the minima in the regions of the best up/down-going hypotheses are sharply peaked (keep in mind that plots such as in Fig. 4.3 are plotted on a log scale), we can roughly approximate the ratio $P_{\mathrm{up}}/P_{\mathrm{dwn}}$ by the ratio of the best up/down likelihoods. Hence, we define the *likelihood ratio*:

$$\mathrm{LR} = \frac{\mathcal{L}(R|\hat{H}_{\mathrm{up}})}{\mathcal{L}(R|\hat{H}_{\mathrm{dwn}})P(\hat{H}_{\mathrm{dwn}})}, \tag{4.8}$$

where $\hat{H}_{\mathrm{up}}$ corresponds to the track hypothesis with the best up-going likelihood, and likewise $\hat{H}_{\mathrm{dwn}}$ corresponds to the track with the best down-going likelihood.

We should now have a sense that the LR is a sort of measure of the quality of the event, suggesting we should investigate the utility of the LR as a cut parameter. This is achieved by using the normalization of $P(H)$ as the cut. We may require the events we retain to be all the more convincing by essentially pretending the down-going muon background rate is higher, or relax our standards by pretending the background rate is lower. Taking this approach also allows us to avoid issues of uncertainty in the likelihoods of track hypotheses far from the $-\log\mathcal{L}$ minimum. The LR does indeed turn out to be very useful cut parameter, as will be demonstrated in §6.4.1.

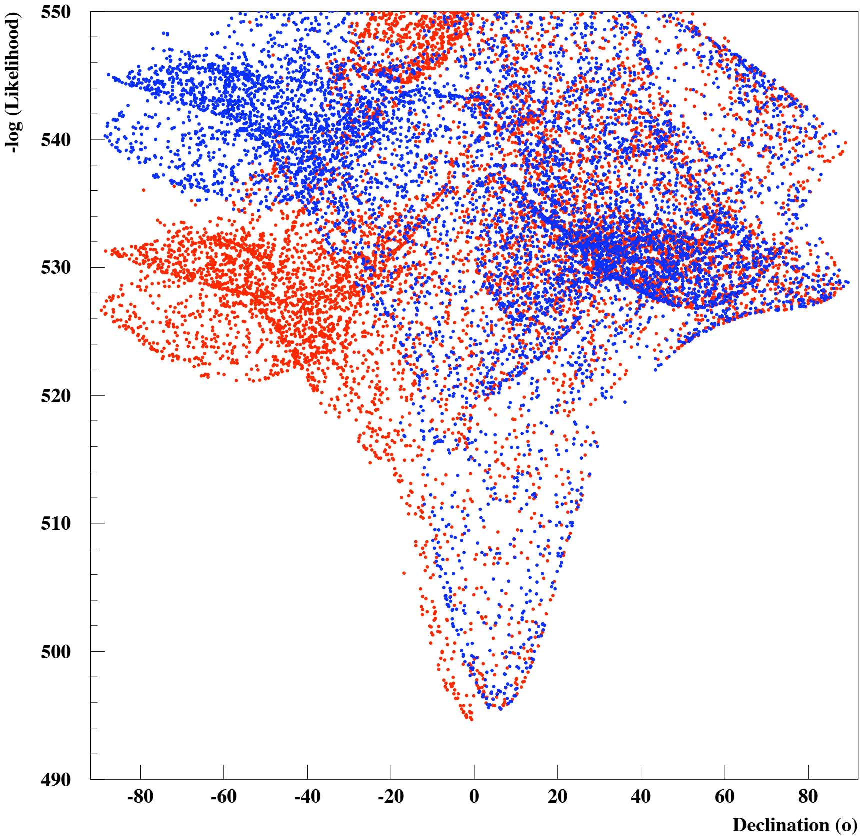

Figure 4.6: A projection of $-\log \mathcal{L}(R|H)$ (blue) for the event pictured in Fig. 4.5. The red projection is the posterior likelihood, $-\log \mathcal{L}(H|R)$, which includes the atmospheric muon prior for $\delta < 0$.

Chapter 5

Point-source Search Techniques

This chapter describes the statistical methods used to optimize and quantify the results of our search for neutrino point-sources. As described in the last chapter, AMANDA can resolve the direction of a neutrino event with a median angular resolution of $\sim 2^\circ$ (depending on declination), and observes a random uniform background of atmospheric neutrinos in the northern hemisphere. An extraterrestrial point-source of neutrinos would manifest as an excess of events above an expected background of atmospheric neutrinos occurring within a bin of angular width on the order of the detector's angular resolution.

As explicitly demonstrated in the next chapter, AMANDA can use muon track observables to distinguish classes of atmospheric neutrino background from the signal hypothesis. This allows us to choose a search sample as a subset of events where we have suppressed the passing rate of the expected background while simultaneously maximizing retention of the hypothetical signal. This goal is the same whether we wish to obtain the maximum significance on an event excess, or if we wish to place the most restrictive flux upper limits on our signal hypothesis.

A search for neutrino point-sources was conducted previously using data collected with the AMANDA-B10 detector in the year 1997 [67] revealing no significant point-source excesses. Given the increase in effective area of AMANDA-II over B10, we would expect at most an improvement of a factor $\sim 4\,\mathrm{or}\,5$ in sensitivity with one year of AMANDA-II data, so a neutrino point-source just under the detection threshold of AMANDA-B10 would be only marginally detectable in AMANDA-II. This motivates the choice to optimize the analysis to obtain the best (most restrictive) flux upper limits on our chosen signal model, which is described in §5.1. We will use the Feldman-Cousins unified approach to confidence interval construction in order to avoid issues of flip-flopping and under-coverage, and choose a method to incorporate systematic uncertainty into an upper limit in §5.2. Lastly, the motivation to conduct a blind analysis to prevent the introduction of human bias is discussed in §5.3.

5.1 Search Optimization

Our analysis strategy depends on our intended scientific goal, as generally outlined in Table 5.1. For the measurement of atmospheric neutrinos, the central technique is the separation of up-going events from down-going atmospheric muons, relying on the reconstructed declination (δ) to reject events with $\delta < 0°$. Atmospheric neutri-

Analysis goal	Up/down	Energy	Spatial origin	Time
Atms. ν	+			
Diffuse	+	+		
Point-Source	+	+	+	
Transient (GRB)	+	+	+	+

Table 5.1: Comparison of general methods of background rejection available depending on the physics goal (searches for atmospheric neutrinos, point-sources, diffuse flux, and transient sources), as described in the text.

nos follow an energy spectrum $dN/dE \sim E^{-2.7}$, whereas astrophysical neutrinos are expected to appear with a harder spectral index, closer to $dN/dE \sim E^{-2}$. Therefore, astrophysical neutrinos may be distinguished from atmospheric neutrinos by placing a cut on the neutrino energy. In the search for diffuse astrophysical flux, for example, the $N_{\rm ch}$ observable (number of OM channels reporting in an event) is used as a rough calorimetric indicator of event energy. When performing a search for point-sources, we have the added ability to further reject the background by using spatially localized search bins. Going one step further, a search for transient sources (GRB) achieves the best rate of background rejection by searching for events coincident with the times associated with independent GRB observations.

5.1.1 Background Measurement

In a search for point-sources incident from specific directions in the sky, we can estimate the expected background in a given search bin by looking off source. Again, we take advantage of our special location at the South Pole; since the detector response varies only with declination, the background may be estimated by calculating the average number of events per steradian in the same band of declination as the search bin. With the ability to exactly measure the background, a search for point-sources has a large advantage over other analyses (diffuse search, for example) which must rely on simulations to predict the background. Signal simulation is however necessary if we want to optimize the search to quantitatively constrain a specific signal model.

5.1.2 Signal Simulation

AMANDA simulation is carried out in successive steps, starting with the neutrino signal generation and ending with the detector's response. The simulation of muons, Cerenkov photons, and the detector hardware was discussed in §3.4.1. Here, the neutrino signal simulation will be described.

A Monte Carlo generator dubbed NUSIM is used to simulate neutrino propagation through the Earth and interaction in or near the detector [74]. The Earth is largely transparent to most neutrinos above AMANDA's energy threshold, so in order to achieve computational efficiency, the simulation forces all generated neutrinos to interact, and then employs numerical weighting techniques to assess, on an event-by-event basis, the probability that the given interaction would actually occur. For the interaction of a muon neutrino of a given energy, the resulting muon energy is chosen from the appropriate distribution. The neutrino interaction point is then chosen at random within a distance to the detector determined by the maximum range of a muon with the given energy. The simulated muon event carries a numerical weight, the product of the probability that the neutrino survived its trip through the Earth, and the probability that it would have actually interacted as forced. The survival probability accounts for all relevant physics affects such as absorption, flavor oscillation, and neutral current regeneration. Simulated neutrinos are typically generated following an E^{-1} energy spectrum, but additional numerical weights may be applied to achieve an arbitrary spectrum.

The NUSIM generator is used to simulate two categories of neutrinos for this analysis: atmospheric neutrinos, and hypothetical point-sources. Atmospheric neutrinos will later serve as a source of calibration for the overall detector sensitivity (in §7.1.1) and to help understand the behavior of the cut parameters (in §6.4.1).

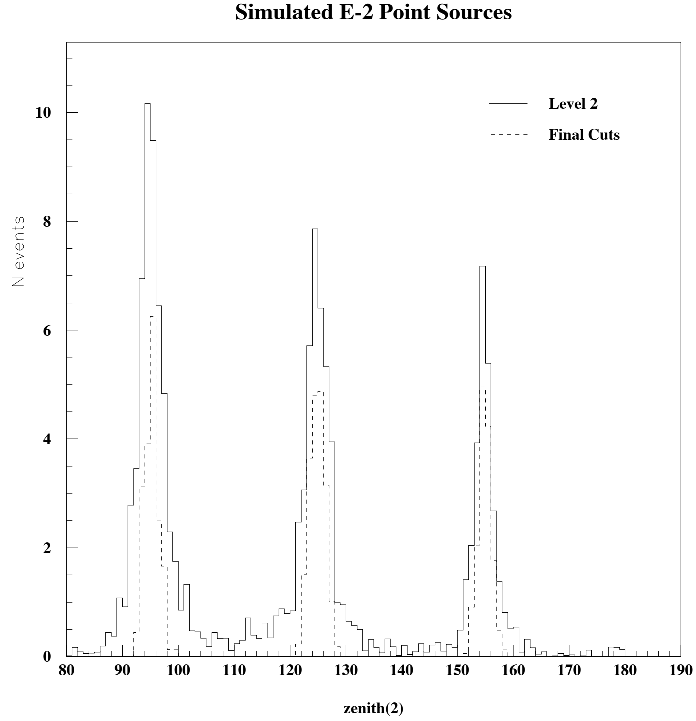

Figure 5.1: Reconstructed zenith distributions of three simulated E^{-2} sources with intermediate (solid) and final cuts (dashed).

The point-source neutrino signal is simulated by restricting the angular generation range of NUSIM to a single declination at a time. What appears as a point-source in the sky appears as a "line-source" in detector coordinates, fixed in zenith and smeared out evenly across all azimuths. Based on the discussions in §2.2, we choose E^{-2} as our nominal signal energy spectrum. point-sources are simulated every 5° in declination in the range $-10^\circ < \delta < 90^\circ$. For illustration, the zenith distributions of three simulated point-sources are shown in Fig. 5.1. The figure demonstrates how the neutrino angular resolution varies with cut level. Also seen is the effect of increasing neutrino absorption in the Earth from the horizon ($\theta = 90°$) to the detector zenith ($\theta = 180°$).

5.2 Upper Limits and Confidence Intervals

The task of this section is to provide a framework in which we can evaluate the unknown strength of a neutrino signal which could be present in the data. In a given angular search bin, we expect either no signal, or a very small one, on top of a mean background of b events, leading to an observation of n_{obs} events. Since the expected signal is small, we are inclined to state our result in terms of an upper limit, $\mu(n_{\text{obs}}, b)$, on the unknown mean number of signal events.

An upper limit is a special case where the classical confidence interval, (μ_1, μ_2), but with $\mu_1 = 0$ and $\mu_2 = \mu$. In general, the confidence interval is taken to be a member of a set of intervals, $[\mu_1, \mu_2]$, obtained in an ensemble of identical measurements such that the set satisfies

$$P(\mu_{\text{true}} \in [\mu_1, \mu_2]) = \alpha \tag{5.1}$$

where α is the stated confidence. In other words, the true value μ_{true} will fall within the set of confidence intervals $[\mu_1, \mu_2]$ with frequency α. If Eqn. 5.1 is satisfied, the set of intervals is said to have the correct "coverage" for the stated confidence level (C.L.).

Classical confidence interval construction according to the method of Neyman [75] occasionally delivers undesirable results in the analysis of small signals with Poissonian background. For example, an observation of 0 events on an expected background of 3 leads to an upper limit of 0 on the number of signal events, and the confidence interval is the empty set. Furthermore, if one decides whether to quote a detection rather than an upper limit based on the experimental results, a practice dubbed "flip-flopping," the resulting confidence intervals will not always have the correct coverage [76]. These troublesome behaviors led Feldman and Cousins to propose an approach to confidence interval construction which unifies the construction of upper limits with that of two-sided intervals.

5.2.1 Feldman-Cousins Unified Ordering

Suppose we want to construct confidence intervals for a Poissonian process with known background, b. Then the probability to make an observation of n events due to a given mean signal strength, μ, on top of the known mean background is

$$P(n|\mu, b) = (\mu + b)^n \exp(-(\mu + b))/n!. \tag{5.2}$$

Proceeding in the usual frequentist fashion, for each value of the unknown signal mean, μ, we construct an acceptance interval, (n_1, n_2), horizontally in the μ vs. n plane such that the total probability contained in the interval satisfies

$$\sum_{n=n_1}^{n_2} P(n|\mu, b) \geq \alpha \tag{5.3}$$

By convention, we replace the equality of Eqn. 5.1 with an inequality due to the discrete nature of the Poisson distribution. This condition leads to over-coverage, and thus *conservative* upper limits. After conducting the experiment and making a measurement, n_{obs}, a (vertical) confidence interval, (μ_1, μ_2), is constructed as the union of all values of μ for which the corresponding acceptance regions, $[n_1, n_2]$, contain n_{obs}.

Besides the limitation imposed by Eqn. 5.3, we are unconstrained as to which values of n to include within the acceptance intervals $[n_1, n_2]$, and it is in this choice

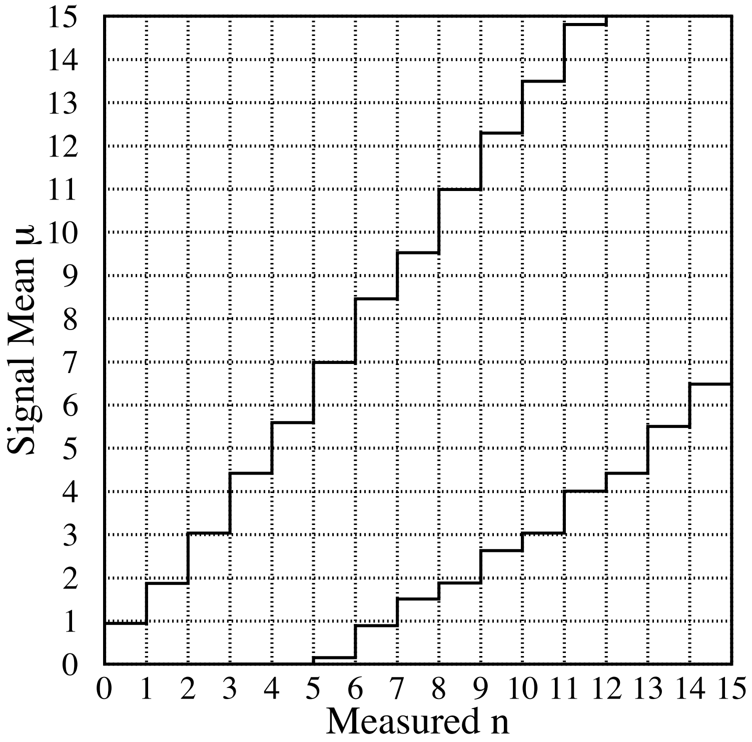

Figure 5.2: Confidence belt based on the Feldman-Cousins ordering approach, for 90% confidence intervals for an unknown signal in the presence of Poissonian background with known mean $b = 3$. From [76].

that the method of Feldman and Cousins differs from the classical approach. Following the classical prescription, we are forced to make a choice, *before conducting the experiment,* whether to present central confidence intervals by making the choice $P(n < n_1|\mu) = P(n > n_2|\mu) = (1-\alpha)/2$, or to present upper limits by choosing $P(n < n_1|\mu) = 1-\alpha$. We must choose to present upper limits *or* central intervals and stick with that choice, or else we face the coverage problems associated with flip-flopping. Alternatively, the Feldman-Cousins method uses a likelihood ratio technique [76] to decide which values of n to include in the acceptance intervals. Let us define

$\hat{\mu}$ as the value which maximizes $P(n_{\text{obs}}|\mu)$. We then compute the ratio

$$R = P(n|\mu)/P(n|\hat{\mu}) \tag{5.4}$$

for each possible value of n for our given b. Using the Feldman-Cousins prescription, the possible values of n to include in the acceptance interval are then chosen in decreasing order of R. Once the acceptance intervals are defined for all values of μ, the confidence interval (μ_1, μ_2) is constructed as described previously.

An example of the resulting unified confidence intervals for $b = 3$ is portrayed in Fig. 5.2. As seen in the figure, the Feldman-Cousins ordering approach transitions automatically from upper limits to two-sided confidence intervals, thus eliminating the possibility of flip-flopping, and the problem of empty confidence intervals.

5.2.2 Model Rejection Potential

To degree to which AMANDA can rule out a given signal model is assessed through the model rejection potential [77], defined as

$$MRP = \mu(n_{\text{obs}}, b)/n_{\text{sig}} \tag{5.5}$$

where $\mu(n_{\text{obs}}, b)$ is the upper limit on the number of signal events (obtained using Feldman-Cousins ordering, 90% C.L.) in a given search bin above the measured mean background b, and n_{sig} is the number of signal events predicted by the simulation of a reference flux, $\Phi_0(E)$. A flux upper limit is then obtained as the product of the MRP and $\Phi_0(E)$.

Individual limits on specific sources are subject to statistical fluctuation, so in order to assess the overall performance of the detector, it is useful to define $\bar{\mu}_{90}(b)$ as the average upper limit (90% C.L.) obtained in a bin with mean background, b, in the case of the null hypothesis (i.e., the true value of $\mu = 0$). We can then obtain the detector *sensitivity*, defined as the the average flux upper limit (90% C.L.) obtained if there are no signal events:

$$\bar{\Phi}_{90}^{\mathrm{lim}} = \Phi_0(E) \times \bar{\mu}_{90}(b)/n_{\mathrm{sig}}. \tag{5.6}$$

It should be noted that a neutrino point-source with strength of the same order as $\bar{\Phi}_{90}^{\mathrm{lim}}$ would not be identified as a detection, so Eqn. 5.6 might be more aptly called the *exclusion potential.* Since a signal detection is deemed unlikely based on the limits obtained in previous point-source searches with AMANDA, we will optimize our present search to achieve the best (lowest) sensitivity on our E^{-2} signal model.

5.2.3 Systematic Uncertainty Incorporation

Until recently, the inclusion of systematic uncertainties in the calculation of confidence intervals has been an overlooked topic. In cases of small signals with Poissonian background, the effect of uncertainty is often (perhaps too easily) assumed to be dwarfed by the effect of the inherent imprecision in the stated confidence level allowed by Eqn. 5.3 when constructing discrete acceptance intervals. We should avoid making this assumption here. Astrophysical measurements at high energies are often very difficult to make, so a reasonable description of the effects of uncertainties would be very useful to help assess the relative performance of different detectors. Though there is no fully frequentist (nor universally accepted) approach to including uncertainty in confidence intervals, there is general agreement that for two experiments with comparable sensitivity, limits quoted by the one with less systematic uncertainty should be more restrictive. The particle physics community has largely adopted a semi-

Bayesian approach of systematic uncertainty inclusion proposed in 1992 by Cousins and Highland [78]. Following this approach, systematic uncertainty arising due to the existence of a nuisance parameter is included by integrating over a probability density function (PDF) describing our prior knowledge of the nuisance parameter, while the unknown signal strength, μ, is treated in frequentist fashion.

In the present search for point-sources, we will be confronted with an uncertainty, σ_ϵ, in our signal efficiency, ϵ, arising due to uncertainties in interaction cross-sections and imperfect modeling of the detector in the Monte Carlo simulation. Following a frequentist approach paralleling that of §5.2.1, we will construct confidence intervals in the $\mu - \epsilon_s$ plane, and define $\hat{\epsilon_s}$ as the best (measured) estimate of the signal efficiency. Then a PDF describing the uncertainty in the signal efficiency may be denoted by $P(\epsilon_s|\hat{\epsilon_s}, \sigma_{\epsilon_s})$, which gives the likelihood of hypothesis ϵ_s given the measurement $\hat{\epsilon_s}$ and our knowledge of the uncertainty σ_{ϵ_s}. By integrating over the all possible values of ϵ_s, we find the likelihood to obtain an observation of n events for a given signal hypothesis, μ, and measured background, b:

$$\mathcal{L}(n|\mu, b, P(\epsilon_s|\hat{\epsilon_s}, \sigma_{\epsilon_s})) = \int_{\epsilon'_s} \mathcal{L}(n|\mu, b, \epsilon'_s) P(\epsilon'_s|\hat{\epsilon_s}, \sigma_{\epsilon_s}) d\epsilon'_s. \tag{5.7}$$

In practice, the integration is performed numerically using a Monte Carlo simulation to evaluate $P(\epsilon_s|\hat{\epsilon_s}, \sigma_{\epsilon_s})$.

To complete the confidence interval construction, we must define an ordering principle. As usual, we are free to choose any scheme as long as it results in proper coverage by satisfying Eqn. 5.3, and displays the correct intuitive behavior discussed above. We choose a hybrid frequentist-Bayesian likelihood ratio test [79] with

$$R = \frac{\int_{\epsilon'_s} \mathcal{L}(n|\mu, b, \epsilon'_s) P(\epsilon'_s|\hat{\epsilon_s}, \sigma_{\epsilon_s}) d\epsilon'_s}{\mathcal{L}(n|\hat{\mu}, b, \hat{\epsilon_s})} \tag{5.8}$$

where the acceptability of a given choice of n to include is evaluated by comparing the likelihood of such an observation after integration over uncertainties to the hypothesis of the best fit, $\{\hat{\mu}, \hat{\epsilon_s}\}$. The choice of which n to include in the acceptance interval for a given μ is then made in decreasing order of R, which naturally leads to unified confidence intervals in μ. The correct coverage and intuitive behavior of the method is demonstrated in [80, 79]. The statistical uncertainty in the measured background (b) is also accounted for in parallel fashion.

5.3 Blindness

Before choosing how to optimize our analysis to achieve the best sensitivity, we must take certain measures to guarantee that the final results of our search are as free from human bias as possible. In the present case, we wish to avoid the artificial enhancement or suppression of background events arriving from any given direction or directions in the sky. The most obvious way to protect the data would be to somehow randomize the arrival direction of each event before cuts are developed, and before a list of specific candidate sources to study is compiled. A practical blindness protection scheme must accomplish this goal while leaving unhindered the ability to study the background and systematic detector effects.

Given our detector's special location at 90° South latitude, an astrophysical point-source would circle the detector at fixed zenith, and events detected at a given azimuth are mapped to their true Right Ascension solely as a function of the Earth's rotation and revolution about the sun. Thus, randomizing the arrival time of each event is a viable way of hiding the arrival directions while at the same time preserving the ability to investigate zenith-dependent systematics.

One would also like to investigate time-dependent systematics. Since most observed time-dependent effects happen on a time scale of days or more, little hindrance is posed to such an investigation by randomizing only the time of day of detection, leaving the day of arrival intact. Since the Earth spins on its axis approximately once per calendar day, randomizing just time of arrival within the day of detection maps the true Right Ascension into the set of all possible Right Ascensions.

This procedure is implemented using a simple perl script to replace the arrival time of each recorded event with a randomly chosen time within the same day, while saving the true arrival time to be restored after the analysis and cuts have been finalized.

Chapter 6

Data Collection & Processing

This chapter describes how an anticipated neutrino signal of astrophysical origin is separated from a seemingly overwhelming background of down-going atmospheric muons, and then distinguished from a background of lower-energy atmospheric neutrinos.

Data reduction is carried out in successive stages, where the goal at each stage is to maximize the E^{-2} signal passing rate and minimize the background passing rate by imposing cuts on parameters which demonstrate good separation power between signal and background. Before background rejection begins, the quality of the data is assessed, as outlined in §6.1. The next stages of large-scale data reduction are described in §6.2 & §6.3, with the selection of final cuts described in §6.4.

6.1 Preprocessing

While running smoothly in data-taking mode throughout most of the austral winter, AMANDA-II occasionally exhibits hardware instabilities, such as spikes in the noise rates of individual OMs and anomalous ADC and/or TDC behavior. The detector behavior is monitored by the winter-overs stationed at the South Pole (and now by the collaboration in the northern hemisphere) in near real-time [81]. The winter-overs are alerted to anomalous detector behavior, track down the cause, and make any necessary repairs or hardware adjustments. Most anomalies are isolated and affect the overall detector performance only slightly, but threaten adverse consequences for the physics analyses to follow. For example, a noisy channel might over-contribute to the trigger, effectively reducing the the trigger multiplicity requirement. The physics consequence would be to alter the N_{ch} distribution (number of OMs reporting during an event), which has critical importance, especially in the search for diffuse neutrino fluxes. These unsimulated detector anomalies must therefore be identified and cleaned from the data before physics analysis begins. A detailed characterization of the 2000 data and description of the pre-processing is given in [61] and summarized below:

- *File cleaning.* AMANDA records data into files, each corresponding to ~ 10 minutes live-time. On rare occasions the detector suffers a catastrophic change in noise or ADC/TDC rates, making entire files of data unusable. Removing the associated files reduces the size of the sample by 2.9%.

- *OM selection.* Channels exhibiting anomalous noise, ADC or TDC rates must be identified and tagged for exclusion from the trigger, or in especially bad cases, excluded from the analysis (reconstruction) entirely, to ensure a good match between experiment and detector simulation.

- *Software re-trigger.* The data are re-triggered offline, removing events that experimentally satisfied the trigger due to hits on the anomalous channels tagged in the previous step. Application of the software re-trigger reduces the size of the sample by 17.4%.

The data analyzed here were collected in the months of February through November, 2000 with a total acquisition time of 254.2 days. After file cleaning, hit cleaning, and factoring in a detector dead-time of 16.8% (see §3.3.1), the effective detector livetime for this analysis is 197.0 days. Atmospheric muon events triggered the detector at a rate on the order of ~ 60 Hz, yielding a trigger-level sample comprising 1.4×10^9 events.

6.2 Low-level Filters

The next step in data processing is to begin substantial size reduction of the sample by throwing away the most obvious down-going atmospheric muons. This is achieved using a fast reconstruction algorithm called the *direct walk-II.* The direct walk (DW) algorithm identifies track elements by joining pairs of direct hits. Track candidates are then derived from the track elements by requiring track-like properties and imposing minimum quality standards. The algorithm is described in detail in [82]. A cut of $\theta_{\rm DW} > 70°$ is placed on file-cleaned sample to yield the level 1 sample. At this stage, a Pandel muon fit (§4.1.1) with 16 random starts is applied, and a cut on the reconstruction result applied at $\theta_{\rm pandel} > 80°$ is imposed, yielding the level 2 sample. Level 1 and 2 passing rates for data and neutrino signal Monte Carlo are

Cut level	Cut applied	Passing Rates	
		Data (events)	Signal
Trigger		1.4×10^9	1.000
Level 1	$\theta_{\rm DW} > 70°$	1.4×10^7	0.91
Level 2	$\theta_{\rm pandel} > 80°$	5.6×10^6	0.86

Table 6.1: Summary of data and signal passing rates for low level filters.

given in Table 6.1.

6.3 Level 3

The processing already described is generally applied to the data for all analyses to follow. At level 3, we begin to process the data specifically for the point-source analysis. Our first task at this stage is to “scramble” (randomize) the reconstructed Right Ascension of each event to prevent subsequent bias in the analysis. This is achieved according to the prescription described in §5.3.

As described in §3.3.3 several strings of the AMANDA-B10 sub-detector communicate with the counting house via twisted pair cables. These cables are susceptible to electrical cross talk which creates artificial hits. The cross-talk filter of §3.3.3 is applied at this stage of the analysis, and the sample is re-reconstructed without using the identified cross-talk hits. After this reconstruction about 35% of the level 2 event sample now reconstructs as downgoing, and is this thrown out, as can be seen in the zenith distribution shown in the top left of Fig. 6.1. The cleaning has only a marginal effect on the signal passing rate. The effect of cleaning noisy channels is also demonstrated by the $N_{\rm ch}$ distribution, before and after cleaning, shown in the top right of the figure. As we would expect, the distribution shifts to the left after cross-talk elimination. Finally, at the bottom in the figure is the likelihood ratio (LR), before and after cleaning. As discussed in §4.2.2, events with a higher LR correspond to a higher quality, and it is seen in the figure that events rejected at this stage are from the lower end of the LR distribution.

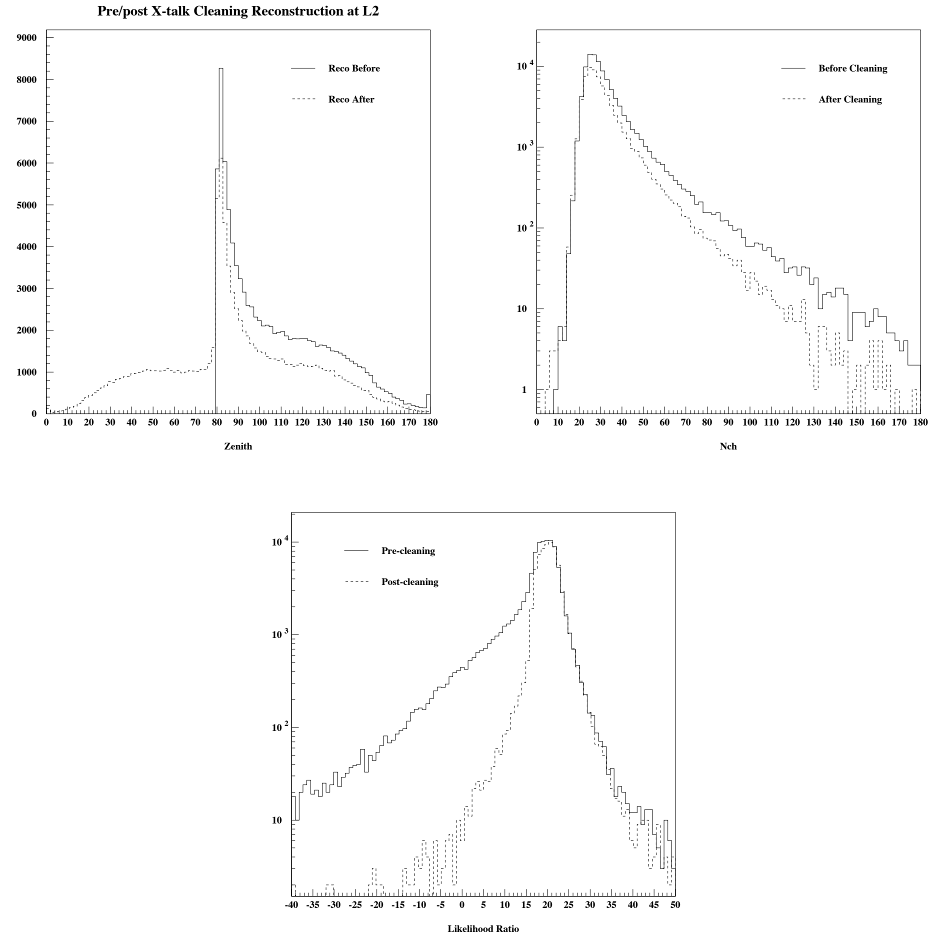

Figure 6.1: Zenith, $\mathrm{N}_{ch}$and likelihood ratio distributions of level 2 events before and after the application of cross-talk cleaning. About 35% of level 2 events are rejected.

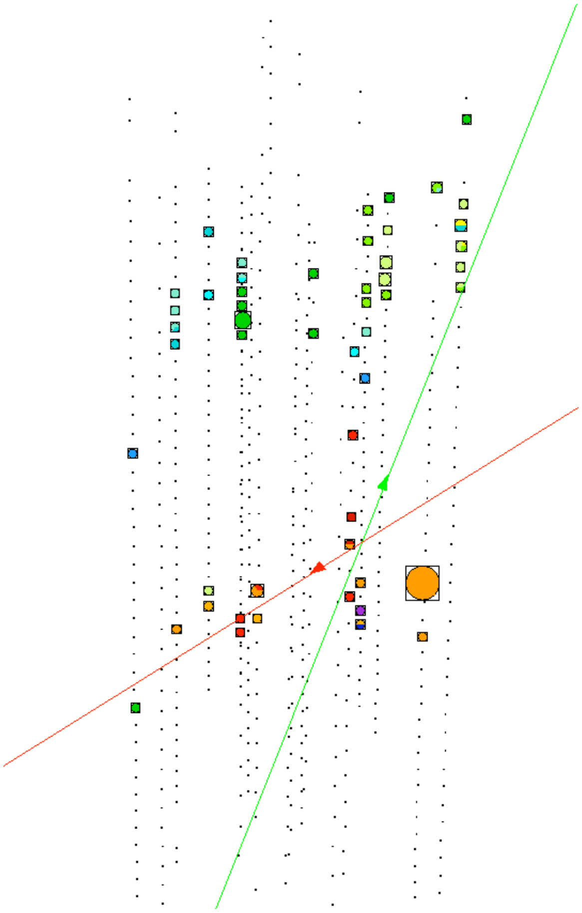

Figure 6.2: An example of a coincident muon event where the two tracks are seperable by eye. The Bayesian downgoing fit (shown in red) finds one of two tracks.

6.3.1 Coincident Muon Rejection

Muons from independent air showers triggering AMANDA coincidentally, though triggering the detector at a rate < 1 Hz, have been known to persist to high cut levels. An example of a coincident muon event is shown in Fig. 6.2. The two coincident muon tracks are clearly seperable by eye in this event. As usual, red and orange hits arriveed first, indicating that the first down-going muon resulted in the track seen at the bottom of the detector, followed by another leaving a seperate, apparently down-going track, in the upper half of the array. The timing reconstruction, shown as the green line, not knowing how to handle a multiple-muon hypothesis, is fooled into thinking this is an up-going event. Meanwhile, the Bayesian reconstruction, when restricted to search only the down-going solutions, accurately traces one of the distinct muon tracks. This observation was initially used to develop a coincident muon event filter based on the difference in the number of direct (nearly unscattered) hits between the standard up-going and Bayesian down-going fits. Since the Bayesian fit often does correctly fit one of the two coincident muons, this fit is more likely to have a higher number of direct hits. A filter was developed, based on this principle, which is seen to reduce the coincident muon background by $\sim 50\%$ while retaining more than 95% of the E^{-2} signal. This cut has been used in other analyses, but we have chosen not to use it here, instead favoring a cut on cylindrical smoothness. Topological smoothness variables measure of how evenly hits are distributed along the track hypothesis. By convention, a perfectly smooth track corresponds to $S = 0$, while those events that are front-loaded with hits (more hits early on) have $S < 0$ and events with too many events at the end of the track have $S > 0$ Also evident in Fig. 6.2 is that hits for coincident muon events tend to be clumped into distinct, isolated bunches resulting in poor smoothness. At this stage of the analysis, an optimized cut is placed on the z-cylindrical smoothness parameter, $|S_{\mathrm{zyldirc}}| < 0.36$ (the smoothness distribution is pictured in Fig. 6.4).

6.4 Final Cuts

Up to this point, we have been concerned primarily with removing known classes of unsimulated background and throwing away only the most obvious down-going events. The post-level 3 background consists primarily of atmospheric muons that have "faked" the detector into thinking they are up-going, as well as up-going atmospheric-neutrino-induced muons. It is now our task to find event quality parameters which behave differently in distributions of both classes of background vs. the expected signal.

6.4.1 Signal Seperation

The hunt for efficient combinations of cut-parameters can be tedious. There are literally hundreds of observables and derived quality parameters defined for use in AMANDA analyses. Most of the parameters are non-orthogonal in cut-space, meaning they often cut away largely overlapping subsets of events. The trick is to find a few nearly orthogonal parameters which show complimentary and efficient background rejection across the whole sky. One narrows down the list of possible combinations of parameters to try based in part on intuition gained from studying many distributions and combinations of observables, as well as with our physics knowledge of the background and signal. To reject atmospheric muon fakes, we might tend to look for parameters that indicate a good quality of reconstruction. To seperate atmospheric neutrinos from astrophysical neutrinos, we will likely utilize parameters related to the neutrino energy.

We begin by investigating the likelihood ratio (LR) introduced in Chapter 4. Likelihood ratio distributions for level 3 data and astrophysical E^{-2} signal are contrasted in Fig. 6.3. As can be seen in the figure, the LR can almost single-handedly remove the majority of the background while retaining a very large fraction of the signal. We know that the LR is not a perfect cut-parameter because it compounds

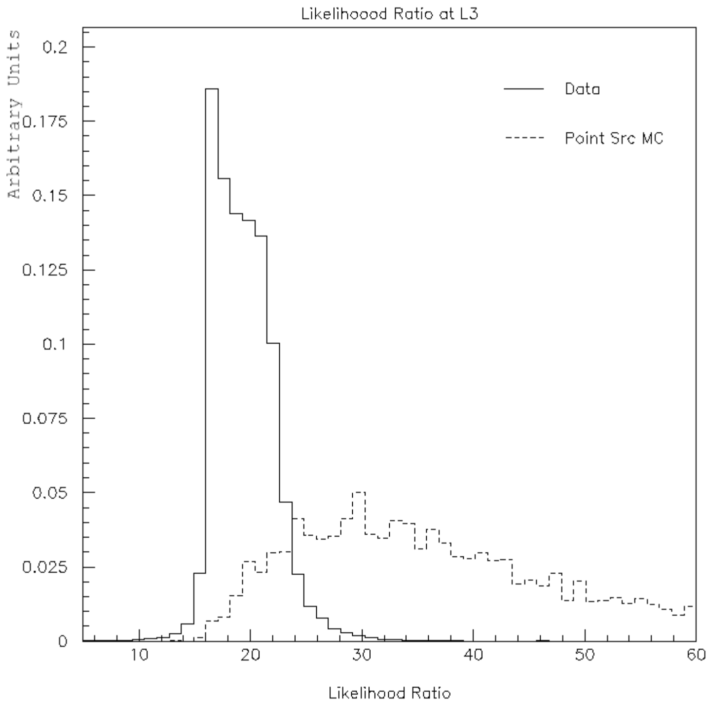

Figure 6.3: The signal seperation power of the likelihood ration (LR) is demonstrated by the contrast between distributions of the level 3 data sample and the expected E^{-2} signal.

inaccuracies found in the tails of the Pandel function, as explained in §4.1.2. Fortunately, several other useful and/or complimentary quality parameters have also been found.

Shown in Fig. 6.4 are six additional quality parameters. The plots show the distributions of data and atmospheric neutrino simulation in each of the given parameters at level 3. First is the cylindrical smoothness, described in the previous section. The smoothness acts as a track quality parameter, good tracks have lower values of $\mid S_{\mathrm{zyldirC}} \mid$. Next is the track length, L_{dirB}, measured in meters from the first direct (unscattered) hit to the last direct hit. Longer tracks tend to recontruct better, so

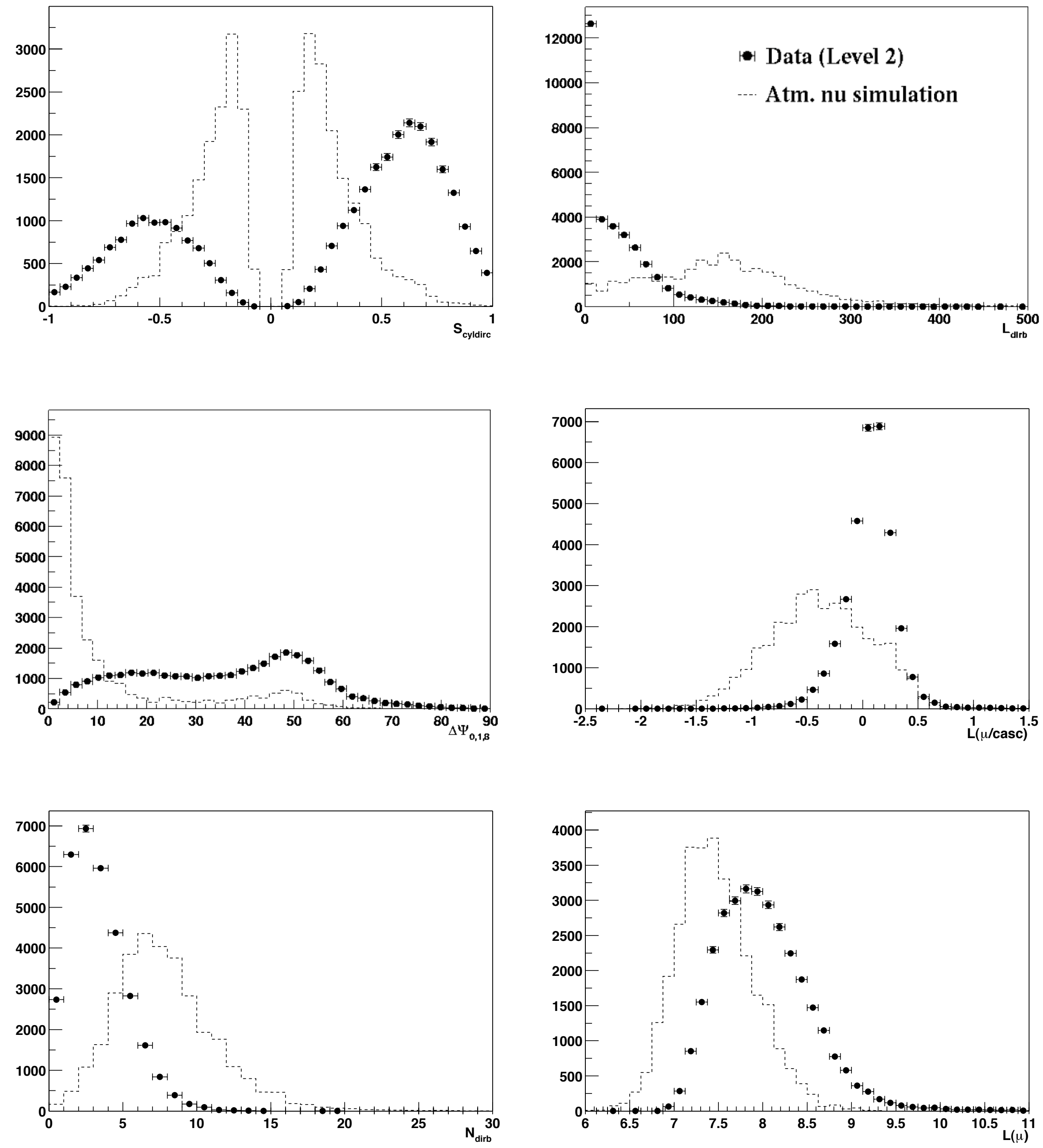

Figure 6.4: Distributions of the NN input variables at level 2, as described in the text

this is one measure of event quality. In the middle left of Fig. 6.4 is plotted $\Delta\Psi_{0,1,8}$, the RMS angular difference in trajectory amoung three diffrent reconstructions, the Direct-Walk-II (0), and the usual Pandel-timing likelihood reconstruction applied before (1) and after (8) the application of cross-talk cleaning (the numbers indicating the corresponding reconstruction indicies). A cut on this parameter would be aimed at retaining well-reconstructed events of high quality by passing only events whose trajectories have remained consistent. At the middle right of Fig. 6.4 is plotted the ratio of the likelihoods of the cascade and muon (timing) reconstructions. The cascade fit attempts to recontruct quasi-spherical events resulting from electromagnetic cascades like the one pictured in Fig. 3.8(b). Events with lower values of $\mathcal{L}_{\mu/\mathrm{casc}}$ are more likely to be muon events rather than cascades. A cut on this parameter is thus an overall quality cut, and helps remove one of the known remaining classes background. Next is N_{dirB}, the number of direct hits per event. Events with more direct hits reconstruct better, so this parameter also measures the quality of reconstruction. The number of direct hits is also partially correlated with the total number of hit channels and thus the energy of the event. Finally is the likelihood of the standard Pandel-timing fit.

6.4.2 Cut Optimization

Having identified several potentially useful quality parameters, how are we to combine cuts on these parameters in order to achieve an optimal search sample? It would be cumbersome to search for the optimum set of cuts in a seven-dimensional cut-space (the number of useful quality parameters we've identified). The situation would be simplified if we combined several of our quality parameters into one. This is accomplished using a neural network (NN) with 6 input variables, 1 hidden layer of 6 units, and one output unit. We have chosen to train the NN to distiguish signal from background using the six quality parameters featured in Fig. 6.4 as input. The NN output unit is designated Q_{NN}, or the "Neural Network Quality." Ultimately, we will optimize cuts on the LR and the Q_{NN} in concert.

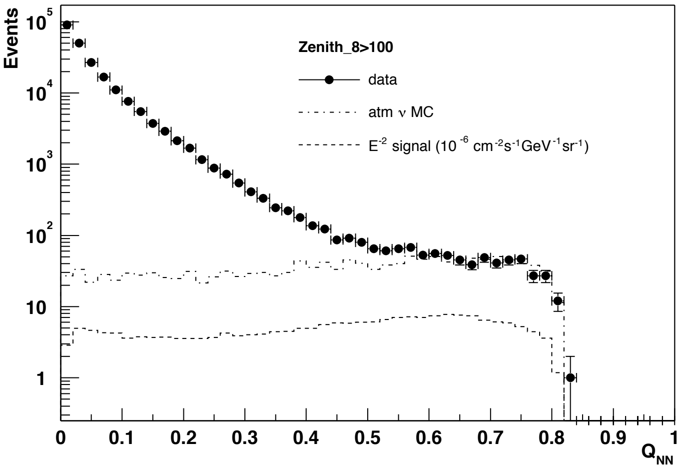

Figure 6.5: NN output parameter Q_{NN} for data, atmospheric neutrino simulation and E^{-2} signal simulation.

The NN was trained using downgoing muons simulated with CORSIKA and neutrino signal sampled from an E^{-2} spectrum. The output varies in the range $0 < Q_{\mathrm{NN}} < 1$, with $Q_{\mathrm{NN}} = 1$ being signal-like, and $Q_{\mathrm{NN}} = 0$ more like background. Level 3 distributions of Q_{NN} for data, atmospheric neutrinos, and E^{-2} signal neutrinos are shown in Fig. 6.5.

All of the cuts used up to level 3 have been applied uniformly over the whole sky, but the quality cut parameters we have investigated show behavior that varies with zenith angle. For example, the parameter L_{dirB}, or the distance between the first and last direct hits recorded in an event, may not generally exceed the width of the detector at a given angle, ranging from 200 m (the width of the detector) for near-horizontally reconstructed events, to well over 500 m (the longest diagonal of the cylindrical detector). Furthermore, the various quality parameters listed above show zenith-dependent efficiencies. For this reason, we are motivated to chose different combinations of cut strengths for different declination regions. In each region, we wish to reject background and retain signal in order to attain the best model rejection potential (MRP), as proffered in §5.2.2. We have at our disposal the point-source simulation introduced in §5.1.2, in which we generated an E^{-2} signal every 5° in declination. We may therefore conduct our search independently in declination each band containing a simulated source. The circular search-bin radius may also be left to vary as a free "cut" parameter vs. declination. At this point in the analysis, the data are still "blinded", but we may still obtain a background expectation in each band by multiplying the average number of events per steradian in the declination band by the solid angle subtended by an optimized search bin for the given band. The optimal cuts on NN quality, likelihood ratio, and search bin radius are then chosen to attain the best MRP on then astrophysical neutrino simulation.

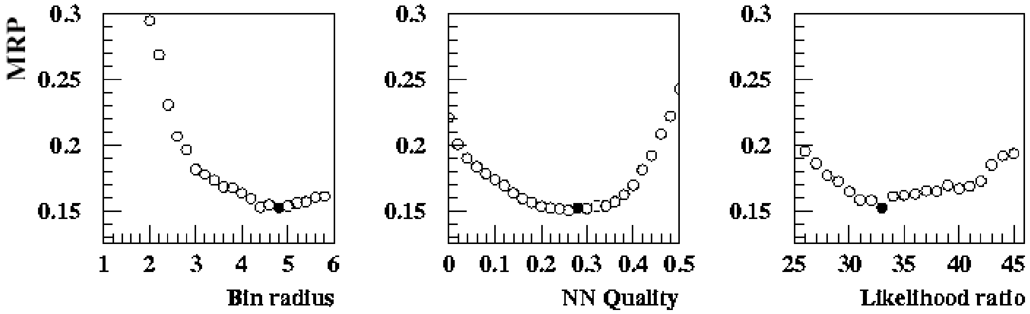

Figure 6.6: The selection of optimal cuts on the circular search bin radius, NN quality, and likelihood ratio for the declination band centered about $\delta = 20^{\circ}$ is illustrated. Plotted is the model rejection potential (MRP) vs. the cut parameter with all other final cuts fixed.

The choice of optimum cuts for the 5° band of declination centered about $\delta = 55^{\circ}$

is demonstrated, for example, in Fig. 6.6. In the case that several global minima occur, or if the global minimum is "bumpy" due to the precision of the signal simulation, the set of cuts closest to the minimum with the largest signal passing rate is chosen. The final cuts for the entire analysis are summarized in Tbl. 6.2.

Dec. [°]	Bin [°]	LR	Q_{NN}	n_{bg}	n_{sig}	μ_{90}	$\bar{\Phi}_{90}^{\mathrm{lim}}$
-5°	2.8°	25	0.38	11.19	8.66	6.16	7.10
0°	4.6°	28	0.40	3.84	15.93	4.02	2.52
5°	4.6°	33	0.34	0.99	18.60	3.26	1.75
10°	4.0°	32	0.28	1.91	19.14	3.44	1.79
15°	4.8°	38	0.22	1.41	22.65	3.92	1.73
20°	4.8°	33	0.28	2.74	22.80	4.05	1.78
25°	4.8°	41	0.22	1.16	17.82	3.15	1.77
30°	4.4°	35	0.30	2.02	21.43	4.11	1.92
35°	3.6°	35	0.30	1.46	19.63	3.26	1.66
40°	3.6°	34	0.32	1.56	18.48	3.65	1.97
45°	3.8°	33	0.30	2.13	21.49	3.83	1.78
50°	3.0°	41	0.32	0.86	18.28	3.08	1.69
55°	3.2°	40	0.34	1.27	17.99	3.53	1.96
60°	3.0°	40	0.44	1.15	15.49	3.34	2.15
65°	3.2°	47	0.44	0.83	13.55	3.04	2.24
70°	2.6°	39	0.50	0.93	13.84	2.82	2.04
75°	3.8°	49	0.58	1.15	15.57	3.82	2.45
80°	2.8°	38	0.50	1.62	12.39	3.23	2.60
85°	4.0°	21	0.62	3.21	12.82	3.76	2.93

Table 6.2: Shown are the optimized cuts on the search bin radius, likelihood ratio (LR), and NN quality (Q_{NN}). The resulting 90% C.L. average neutrino flux upper limits ($\bar{\Phi}_{90}^{\mathrm{lim}}$) given in units of 10^{-7} $\mathrm{GeV}^{-1}\,\mathrm{cm}^{-2}\,\mathrm{s}^{-1}$, calculated using Eqn. 5.6. The optimized cuts for $\delta = -5°$ are applied to all events with $80° < \delta < 87.5°$, and the cut for $\delta = 85°$ to events with $172.5° < \delta < 177.5°$. The intermediate cuts are applied to events falling in 5° bands centered on the given declination.

Special rules apply for the background estimate above $\delta > 85°$ where, due to the small number of search bins needed to cover lessening solid angle, the background estimate could be affected by the presence of events from an astrophysical source. Tbl. 6.3 demonstrates stability of the background estimate at high declinations. This behavior allows us to choose the cuts and background estimate for the single search bin at the detector's zenith by attaining the background estimate using the event density of the adjacent region $75^{\circ} < \delta < 85^{\circ}$, leading to a background estimate of 2.3 events within a search bin of radius 3.4°.

Declination	n_{obs}	Events/sr
$75^{\circ} < \delta < 85^{\circ}$	39	205
$80^{\circ} < \delta < 85^{\circ}$	15	209
$75^{\circ} < \delta < 87.5^{\circ}$	44	211
$80^{\circ} < \delta < 87.5^{\circ}$	20	223

Table 6.3: The number of observed events (n_{obs}) with final cuts in the given ranges of declination.

By applying the final cuts of Tbl. 6.2, we are left with a blinded final sample of events. The expected average flux upper limits (90% and 99% C.L.) are shown in Fig. 6.7. The average flux upper limits rise at the horizon ($\sin\delta = 0$) as the background begins to rise steeply. The rise near the detector's zenith ($\sin\delta = 1$) occurs as the expected signal decreases slightly due to neutrino absorption in the Earth. Uncertainty is included in the plot according to the methods described in §5.2.3. We can see the effects of the discrete ordering in the confidence belt contruction, as was previously discussed.

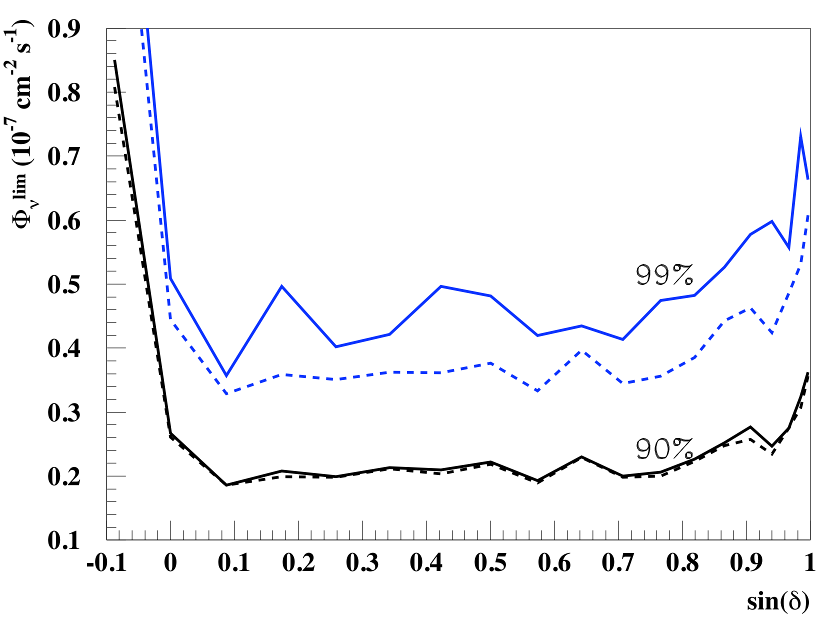

Figure 6.7: Average 90% and 99% C.L. upper limits vs. declination (90% and 99% C.L.) expected for the optimized cuts, with and without the inclusion of systematic uncertainty.

Chapter 7

Experimental Results

This chapter presents the experimental results of this analysis. The selection of cuts for the final point-source search sample was described in the previous chapter. Before unblinding the data, a scheme for conducting the all-sky search for excesses is devised and optimized. The data are then unblinded, the search conducted, and the results evaluated in §7.2. Upper limits on the flux of muon neutrinos from specific astrophysical candidate sources are presented in §7.3. The overall sensitivity of the analysis is generalized by a discussion of the neutrino and muon effective areas versus energy in §7.4.

7.1 Sample Assessment

With the application of the cuts given in Tbl. 6.2, a final sample comprising 699 events above $\delta > 0^\circ$ is achieved. Before unblinding the sample and conducting the search for excesses, the quality of the data and systematic uncertainty is assessed. As demonstrated by the zenith distribution of the final sample compared to the atmospheric neutrino expectation, shown in Fig. 7.1, the sample is dominated by atmospheric neutrino background above a zenith of $\theta > 95^\circ$. Atmospheric muons dominate below.

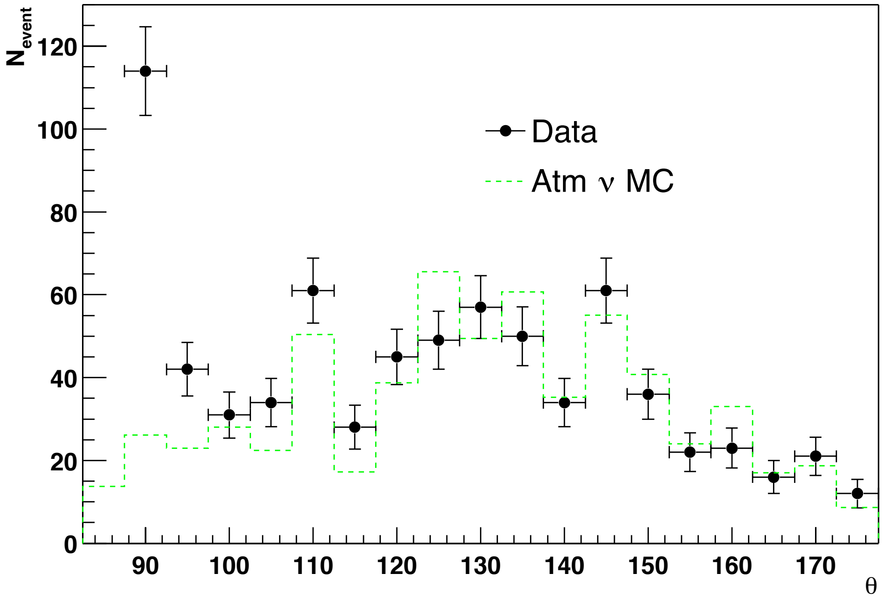

Figure 7.1: Comparison of data events and atmospheric neutrino MC after final cuts.

7.1.1 Signal Normalization & Systematic Uncertainty

Final distributions of the NN quality parameters appear in Fig. 7.2. Here we see that the final data sample is in good agreement with the atmospheric neutrino expectation, indicating that we have largely removed all other backgrounds to our search for astrophysical sources. It is perfectly acceptable to have some remaining non-simulated background; it is only important that we can precisely quantify the background through measurement.

Given the good agreement seen, we may safely believe that our simulations correctly describe the response of the detector, but with the presence of systematic effects

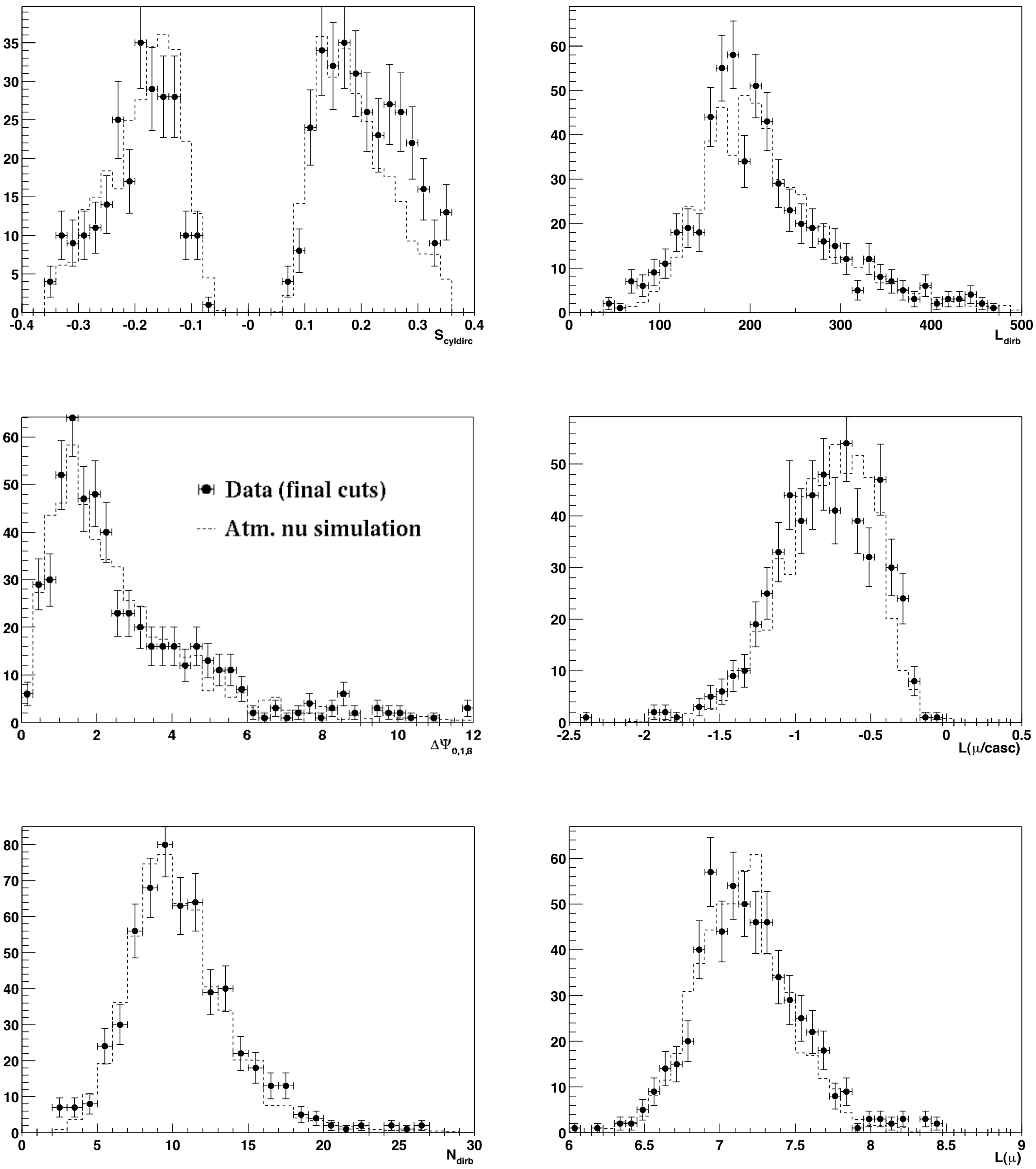

Figure 7.2: Comparison between distributions of data and atmospheric neutrino expectation in the six NN input variables at the final cut level.

(such as those arising from an approximate simulation of the fiducial ice properties) we can not be confident in the absolute rate of events predicted by the simulation. In order to place the most accurate limits on our model, we must experimentally calibrate the overall efficiency of the simulation.

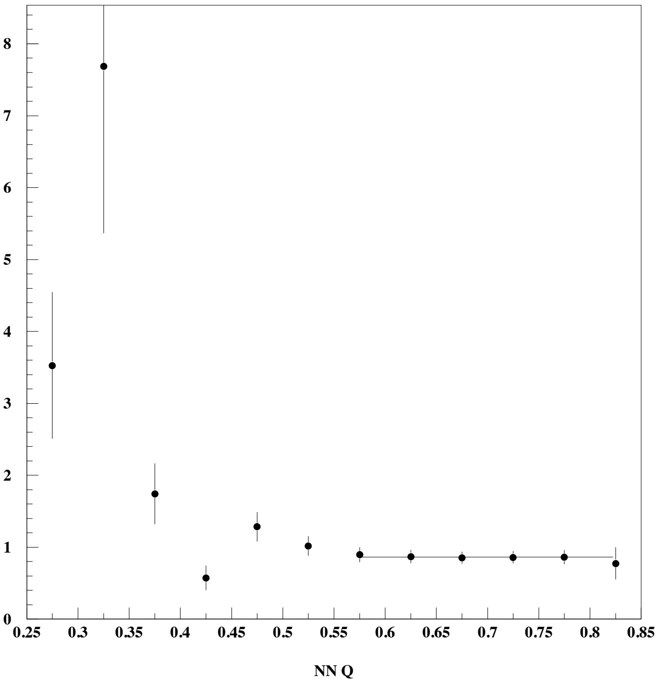

Figure 7.3: A comparison of data and atmospheric neutrino simulation after even tighter cuts: $\theta > 100°, | S_{\text{zyldirC}} |< 0.36, L_{\text{dirB}} > 150, \log \mathcal{L}_{\text{up}} - \log \mathcal{L}_{\text{dwn}} > 35$, applied uniformly over the sky. Plotted is the ratio of the number of data events to simulated atmospheric neutrino events differentially in NN quality, Q_{NN} The error bars on the data points are statistical based on the number of data events.

Atmospheric neutrinos provide us with the experimental calibration source we need. To calibrate, we want to make sure we are comparing a pure sample of atmospheric neutrinos to the expectation from simulation under the same sets of cuts. This is done by strengthening the cuts until a constant ratio of data to simulated events is encountered. A highly pure experimental sample of atmospheric neutrinos is produced using a tight set of additional quality cuts ($\theta > 100°, | S_{\text{zyldirC}} |< 0.36, L_{\text{dirB}} > 150, \log \mathcal{L}_{\text{up}} - \log \mathcal{L}_{\text{dwn}} > 35$) applied to the final sample. This data are then compared to the atmospheric neutrino expectation as shown in Fig. 7.3. The ratio of the number of data to simulated events flattens out above a NN quality $Q_{\mathrm{NN}} > 0.55$. In this region, we determine the signal efficiency of the simulation by fitting a straight line to the ratio of data to simulated events across the remaining NN qualities. We arrive at an overall efficiency of 0.86, to be applied to the predictions from both atmospheric and astrophysical neutrino simulation. Having normalized atmospheric neutrino expectation to the data, we must carry forward the theoretical uncertainty on the atmospheric neutrino flux of $\pm 25\%$ [83] (the effect of which was seen in Fig. 6.7).

7.1.2 Angular Pointing Resolution

Of particular importance for a point-source search is detector's the angular pointing resolution, as it defines what a "point" source will look like in AMANDA. Unfortunately, no calibration source of beamed high energy neutrinos is available, so a detailed investigation of the angular pointing resolution vs. declination must be conducted using simulations. The distribution of space angle difference between the true neutrino trajectory (from our E^{-2} simulation) and the reconstructed trajectory for a source at Dec. 55° is shown in Fig. 7.4. The median pointing resolution at this declination is determined to be 1.7° from this plot. The median space-angle resolution for the final sample is plotted vs. declination on the left in Fig. 7.5. The exhibited behavior is a function of both the detector response and the specific set of quality cuts of we have chosen. With nearly twice the diameter of the AMANDA-B10 sub-detector, the 19-string AMANDA-II array demonstrates an improvement in angular resolution (from about $\sim 3.5°$ in B10 [84]), especially near the horizon (Dec. 0°) due to a larger lever arm.

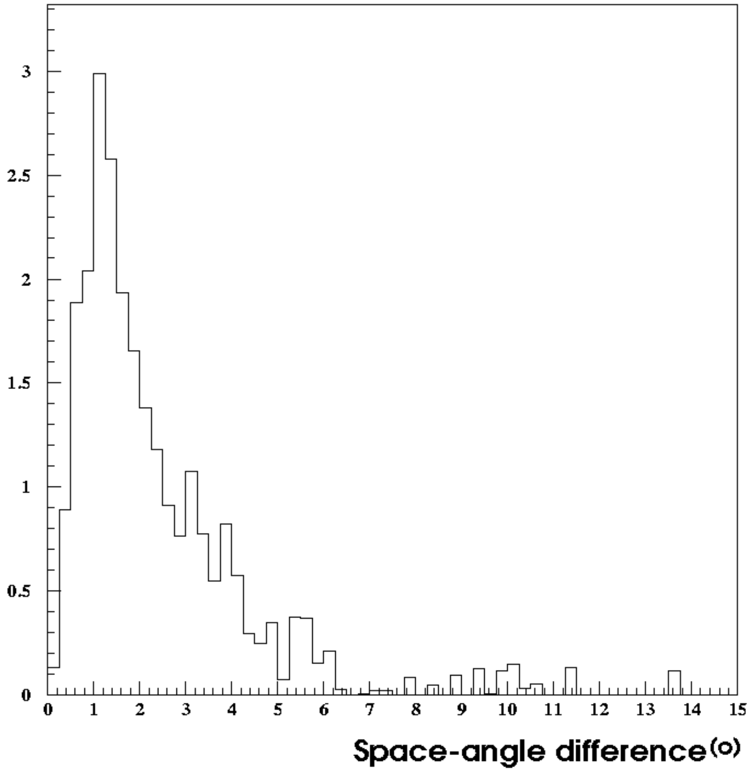

Figure 7.4: Absolute space-angle difference between the reconstructed and true trajectory of simulated astrophysical neutrinos simulated at Dec. 55°.

On the right in Fig. 7.5, one can see the median resolution averaged over all northern declinations rises from 2.5° to 3.5° with energy from 100 GeV to 10^8 GeV. As the energy of of an event rises, the number of OMs reporting multiple photon hits increases, as well does the total number of channels (N_{ch}) fired. In the case of such bright events, the track hypothesis can actually become less constrained than for lower multiplicity events. This is because the reconstruction calculates photon arrival-time probabilities assuming only one hit is observed. When multiple hits are observed, the probability distribution for the first of N photons deviates from the single hit timing

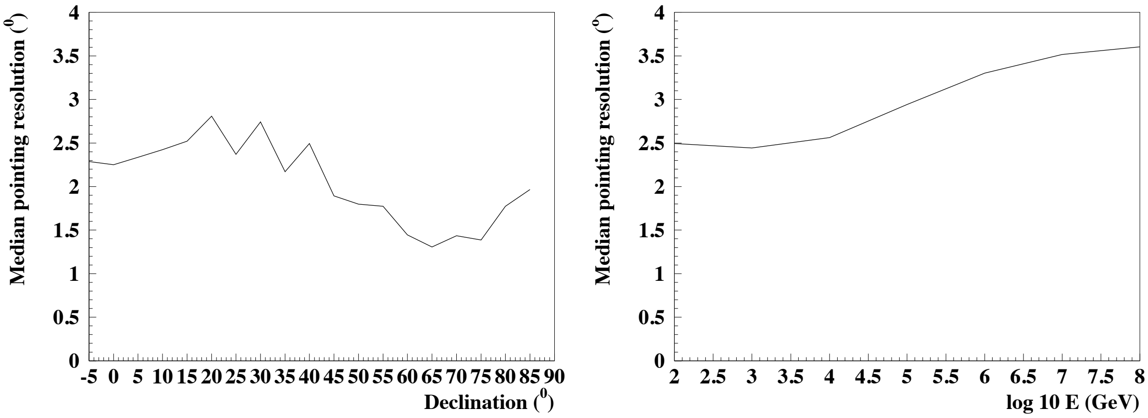

Figure 7.5: AMANDA-II median angular pointing resolution is shown vs. Declination for a simulated astrophysical neutrino signal with spectrum $dN/dE \sim E^{-2}$ (left), and the average resolution over all northern declinations vs. neutrino energy (right).

distribution.

7.2 Binned Search for Excesses

The next step before unblinding the data is to prepare a strategy to search the sky for unknown neutrino point-sources. In this section, we will optimize a rectangular search grid and develop the statistical tools needed to quantify the significance of any excesses that may appear. Once everything is in place, we will unblind the sample and conduct the search.

7.2.1 The Significance Test

To aid in the quantitative evaluation of an excess, we define the following significance statistic: $\xi = -\log_{10}(P_{\mathrm{c}})$, where P_{c} is the chance probability of observing n_{obs} due to a random upward fluctuation of the expected background, n_{bgd}, in a given search bin, evaluated using binomial statistics. To decide whether or not an excess is an actual neutrino signal, the distribution of significances must be compared to what would be observed in the case of a purely random background. For this purpose, a "toy" Monte Carlo model is devised. The experimental data sample is used to generate $N_{\mathrm{mc}} = 10,000$ samples with randomized R.A., preserving the experimentally observed declination. Once the search grid and procedure is optimized, the resulting experimental significances are compared to the distribution of significances resulting from repeating the search on the N_{mc} randomized samples.

7.2.2 Search Grid Configuration & Optimization

Before unblinding, a search grid of rectangular bins with zenith-dependent bin sizes, appearing in Fig. 7.6, is constructed between $-5° < \delta < 85°$. The size of each bin is selected based on a polynomial fit of the optimized search bin radius vs. declination as determined during the simultaneous optimization of all final cuts, described in §6.4.2.

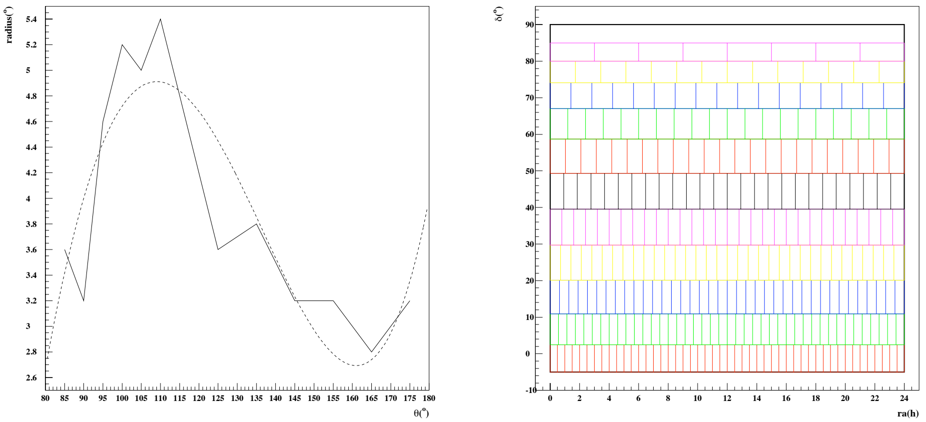

Figure 7.6: Optimized bin size and the polynomial fit used to determine the bin widths for the grid search (left). The initial grid-search configuration, "grid 0" (right).

If a point-source of neutrinos happened to be centered on one of the boundaries between bins, an experimental excess would be split between two or more bins, resulting in a lower significance than if the source were centered in a bin. For this reason, the grid is shifted multiple times to cover the boundaries of the original configuration. Shifting the grid increases the chance of observing an excess from a source at an unknown location in the sky. However, each time the grid is shifted, the statistical trials penalty increases, decreasing the overall significance of any given excess. The natural course of action would be to find the optimum balance between the number of search grids and the trials penalty.

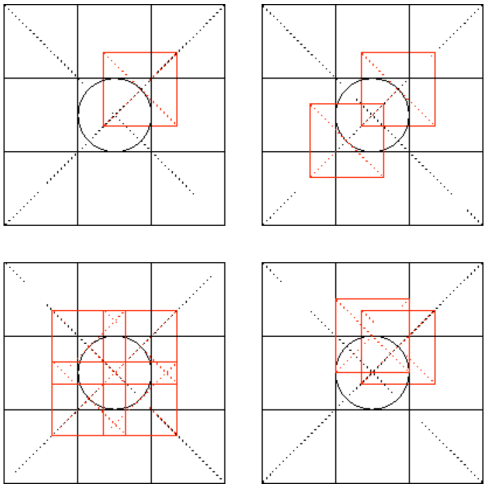

Figure 7.7: The relative positioning of N shifted grids is defined, as described in the text.

Before performing this optimization, we must chose how to configure the shifted grids relative to one another. A circle is drawn with center at the center of a reference bin and radius equal to the optimized search bin radius, as depicted in Fig. 7.7. For example, for $N = 2$ (one original grid and one shifted grid), the shifted grid is obtained by moving the bin center on a the circle at at an angle of 45°. For $N = 3$ (two shifts), the next grid, is found by rotating the first shifted grid around the circle by 180°. For an arbitrary number of shifts, the $N-1$ shifted grids have reference bins centered on this circle, seperated by $(360°/N)-1$.

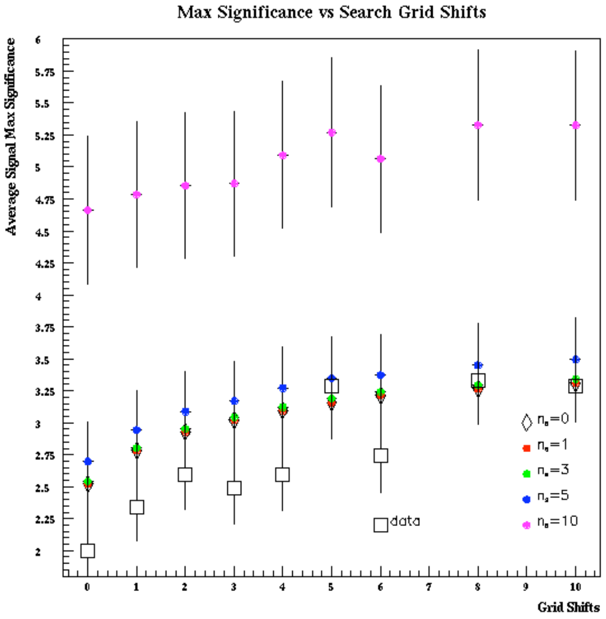

Figure 7.8: Shown are the average values (over $N_{\rm mc} = 10,000$ samples) of maximum significance found when including simulated signals of various strengths, $N_{\rm sig}$, as a function of the number of grid shifts. For this calculation, the number of background in the sourch bin is fixed at $N_{\rm bgd} = 2$. The error bars are the RMS of the maximum significance distributions. Also shown is the maximum significance obtained from the scrambled experimental sample.

Next, the minimum number of shifts, $N_{\rm shift}$, needed to maximize the significance of an excess is determined. Suppose we expect a single point-source in the sky which we are to identify using our significance test. To see how such a signal would appear above the random background, we simulate the appearance of a signal of $N_{\rm sig} = 1, 3, 5, 10$ events, spatially distributed according to a point spread function determined from the full neutrino simulation, on top of the N_{mc} randomized samples. The signficance of the bin resulting with the largest excess from the simulated signal is compared to the distribution of maximum significance found when performing the grid search on each of the N_{mc} randomized samples. The signal significance is investigated as a function of the number of grid shifts.

The results are shown in Fig. 7.8. The average values of maximum significance increase both with increasing source intensity at a fixed number of grid shifts, and with increasing number of grid shifts at a given source intensity. After four shifts the maximum significance obtained increases only marginally, leading to a choice of $N = 5$ (corresponding to four shifts).

7.2.3 Results

Now that our search algorithm has been optimized, the data are ready to be unblinded by restoring the reconstructed R.A. for each of the final experimental events. The unblinded sample is shown as a skyplot in Fig. 7.9. Our first glace at the skyplot reveals a mostly even distribution of background events, with perhaps one possibly significant excess near $\delta = 40^\circ$ and 21 h R.A. Of course, we do not want to rely just on our eyes, because they can be fooled by the projection we have used.

Performing the all sky search with $N = 5$, we find the largest excess, observed at about $68^\circ\,\mathrm{Dec.}, 21.1\mathrm{h}\,\mathrm{R.A.}$, to be 8 events observed on an expected background of 2.1. As planned, the significance of this excess is determined by noting how often a larger excess appears in our collection of N_{mc} randomized samples. Figure 7.10 is a plot of our significance test statistic ξ, computed for the largest excess seen in each of the random samples. By integrating the distribution above the largest experimentally

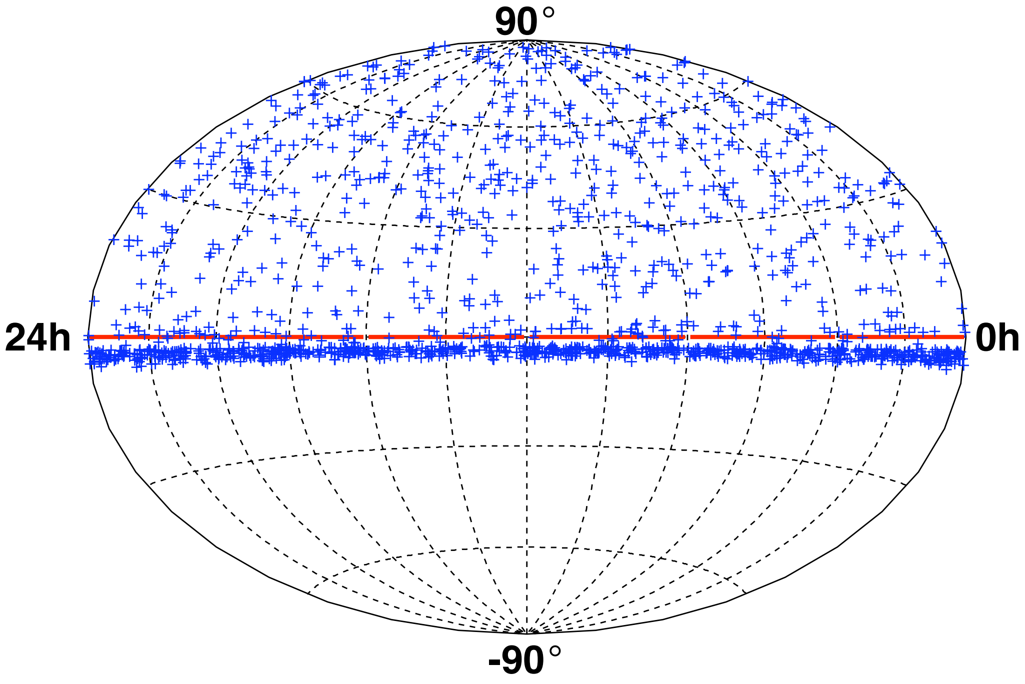

Figure 7.9: Unblinded skyplot in equatorial coordinates of the final search sample.

observed excess, having a significance $\xi = \log_{10}(P_c) = 3.17$, we find that the largest excess has a chance probability of 51% to be a random upward fluctuation of the background.

7.3 Flux Upper Limits

In the absence of a signficant signal detection, flux upper limits may be placed on known interesting celestial objects falling into the theoretical categories discussed in §2.3. With the sensitivity achieved in this analysis, AMANDA-II may be able to rule out some theoretetical models, while others predict fluxes that may be marginally detectable. Before unblinding the data, a list of candidate sources to investigate was

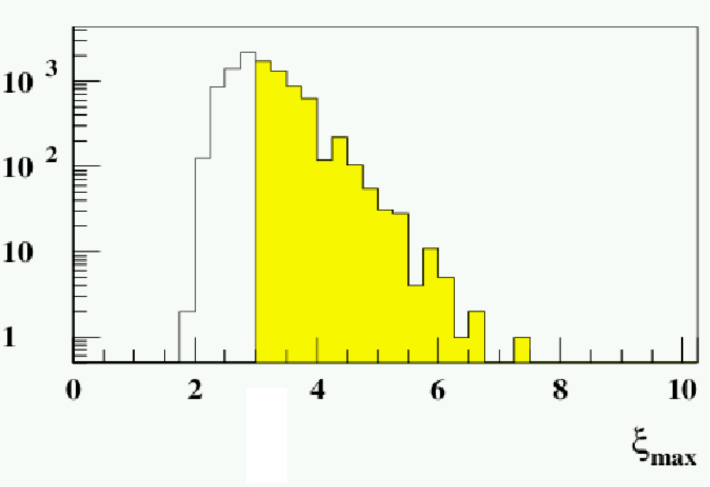

Figure 7.10: Distribution of maximum signifance, $\xi = \log_{10}(P_c)$, found by performing 10,000 repetitions of the grid search on samples randomized in R.A. The vertical line with shaded area to the right indicates ξ of the highest experimentally observed significance. The total probability contained in the shaded area is 51%

compiled. The aim of the candidate source selection is not to increase the chances of a signal detection, but to provide flux upper limits on sources of interest to the astrophysics community. The list includes all northern hemisphere TeV γ-emitting blazars, as well as GeVγ-emitting blazars likely to be neutrino loud [31]. All presently known microquasars in the northern hemisphere are included, as well as four γ-loud supernovae remnants, the Crab, Cassiopia A, SGR 1900+14 and Geminga. Finally, the 2 strongest EGRET sources, the closest quasar NGC 1275 and the two UHECR triplets observed in AGASA/Haverah Park data [85, 86] are included.

Limits are calculated as usual according to Eqn. 5.6. A circular search bin of optimal radius for the given declination band is centered on each candidate source. The background is measured by looking off-source in the same band of declination and the number of events expected from the signal model is determined by simple linear interpolation between the fixed sources already simulated.

The entire list of neutrino flux upper limits appears in Table 7.1. Between the current search and previous searches, AMANDA holds the most restrictive limits currently published on the sources presented.

Candidate	Dec. [°]	R.A. [h]	n_{obs}	n_b	Φ_μ^{lim}	Φ_ν^{lim}
Blazars						
Markarian 421	38.2	11.07	3	1.50	3.0	3.5
Markarian 501	39.8	16.90	1	1.57	1.5	1.8
1ES 1426+428	42.7	14.48	1	1.62	1.4	1.7
1ES 2344+514	51.7	23.78	1	1.23	1.6	2.0
1ES 1959+650	65.1	20.00	0	0.93	0.9	1.3
QSO 0528+134	13.4	5.52	1	1.09	2.5	2.0
QSO 0235+164	16.6	2.62	1	1.49	2.0	1.7
QSO 1611+343	34.4	16.24	0	1.29	0.7	0.8
QSO 1633+382 lat	38.2	16.59	1	1.50	1.5	1.7
QSO 0219+428	42.9	2.38	1	1.63	1.4	1.6
QSO 0954+556	55.0	9.87	1	1.66	1.3	1.7
QSO 0716+714	71.3	7.36	2	0.74	2.9	4.4
Microquasars						
SS433	5.0	19.20	0	2.38	1.0	0.7
GRS 1915+105	10.9	19.25	1	0.91	2.9	2.2
GRO J0422+32	32.9	4.36	2	1.31	2.9	2.9
Cygnus X1	35.2	19.97	2	1.34	2.2	2.5
Cygnus X3	41.0	20.54	3	1.69	3.0	3.5
XTE J1118+480	48.0	11.30	1	0.92	1.7	2.2
CI Cam	56.0	4.33	0	1.72	0.6	0.8
LS I +61 303	61.2	2.68	0	0.75	1.0	1.5
SNR, magnetars & miscellaneous						
SGR 1900+14	9.3	19.12	0	0.97	1.4	1.0
Crab Nebula	22.0	5.58	2	1.76	2.6	2.4
Cassiopeia A	58.8	23.39	0	1.01	0.9	1.2
3EG J0450+1105	11.4	4.82	2	0.89	4.2	3.2
M 87	12.4	12.51	0	0.95	1.3	1.0
Geminga	17.9	6.57	3	1.78	3.7	3.3
UHE CR Triplet	20.4	1.28	2	1.84	2.4	2.3
NGC 1275	41.5	3.33	1	1.72	1.4	1.6
Cyg. OB2 region. [46]	41.5	20.54	3	1.72	2.9	3.5
UHE CR Triplet	56.9	12.32	1	1.48	1.4	1.9

Table 7.1: 90% upper limits on candidate sources. The number of events observed within the search bin is denoted by n_{obs}, and n_b is the number of expected background events determined by measuring the background off-source in the same declination band. Limits are for an assumed E_ν^{-2} spectral shape, integrated above $E_\nu = 10\,\mathrm{GeV}$, and presented in units of $10^{-15}\mathrm{cm}^{-2}\,\mathrm{s}^{-1}\,(\Phi_\mu)$ and $10^{-8}\mathrm{cm}^{-2}\,\mathrm{s}^{-1}\,(\Phi_\nu)$.

7.3.1 Limit Variation with Spectral Index

We have assumed as our baseline signal model an E^{-2} signal spectrum. Of course this is only speculation based our current best understanding of how high-energy astrophysical neutrinos may be produced. Of course we don't really know with what spectral index the first detected neutrino point-source will appear. The best way to place limits on a model with a different spectral index would be to reoptimize the cuts under the new hypothesis. Short of that approach, limits on other spectra are still calculable, even though they may not be optimal.

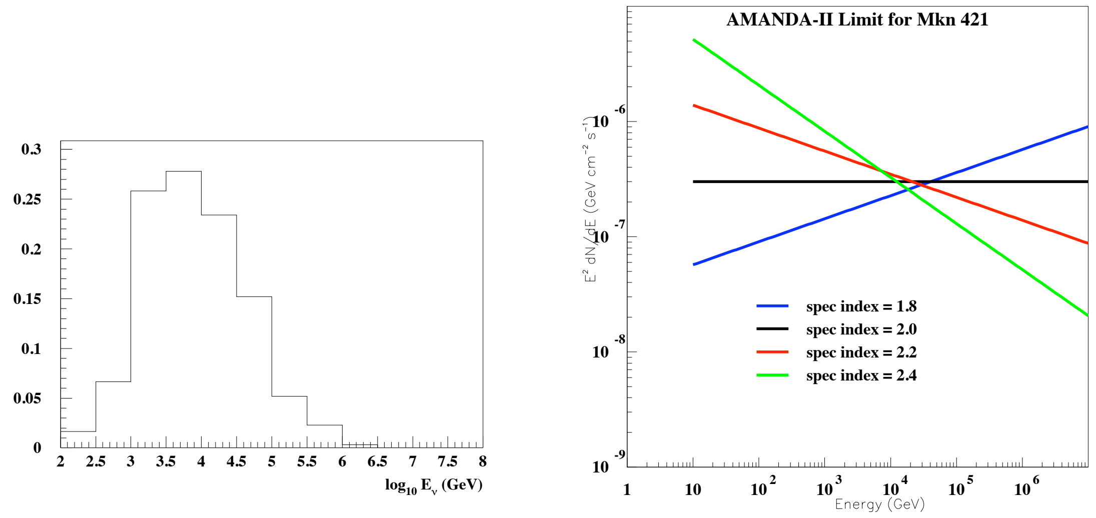

Figure 7.11: The energy distribution of neutrino events expected from the blazar Markian 421 for an $E_\nu^{-\alpha}, \alpha = -2$ signal hypothesis (left), and variation of the AMANDA-II flux upper limit with spectral index, α. The limits for different spectra converge near the most probable energy, $E_\nu \sim 10$TeV.

It is worth looking at an example in detail. Shown in Fig. 7.11 are the limits obtained in this analysis on the blazar Markarian 421 for different assumed signal spectra. All of the limits converge to near $E_\nu \sim 10\,\mathrm{TeV}$, where the energy response of AMANDA is the best, as seen in the left in the figure. Such a plot is easy to produce by reweighting our signal simulation to the desired spectral index, but for the independent reader, an estimation of a limit for a spectral index other than 2 is possible using a plot of the neutrino effective area.

7.4 Effective Area

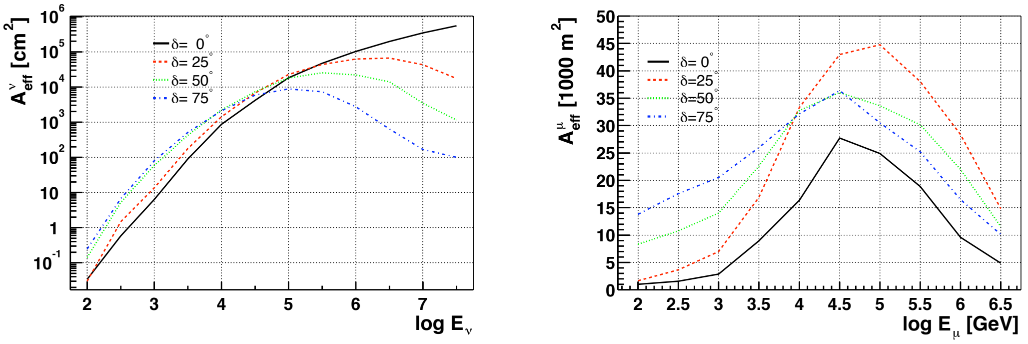

Figure 7.12: Neutrino and muon effective areas vs energy at different declinations (δ). E_μ is the muon energy at closest approach to the center of the detector.

The most general way to assess the performance of the analysis is through an examination of the neutrino effective area, shown in Fig. 7.12. The neutrino effective area is defined as

$$A_\nu^{\mathrm{eff}}(E_1, E_2) = A_{\mathrm{gen}} \frac{n_{\mathrm{sig}}}{n_{\mathrm{gen}}} \tag{7.1}$$

where A_{gen} is the area of the signal generation plane, n_{gen} is the total number of signal neutrinos generated in the range $E_1 < E_\nu < E_2$, and n_{sig} is the number of simulated signal events surviving the final cuts. We may understand the effective area as the size of a perfect detector in which all particles passing through it are detected. In theory, one can use the effective area to calculate a signal expectation for an arbitrary source spectrum, $d\Phi/dE_\nu$ by

$$n_{\rm sig} = T_{\rm live} \int_{E_1}^{E_2} A_\nu^{\rm eff}(E'_\nu) \frac{d\Phi}{dE'_\nu} dE'_\nu \tag{7.2}$$

where $T_{\rm live}$ is the detection live-time. The effective area thus carries the neutrino interaction probability as well as the energy response of the detector all in one.

Also shown in Fig. 7.12 is the muon effective area, which contains only the response of the detector to muons. To obtain a signal expectation using the muon effective area, one must account for the neutrino interaction and muon range seperately. The muon effective area is useful to make comparisons to other detectors such as large cosmic-ray air-shower arrays. Note that at high energies the neutrino area at $\delta = 0^\circ$ exceeds the areas at larger declinations while the muon area for horizontal events is the smallest in the whole energy range. This is due to neutrino absorption in the earth which is included in the definition of neutrino effective area.

The cuts of this analysis have been optimized for an assumed E^{-2} neutrino spectrum, and the results are also primarily presented for this spectrum. Limits for other spectra can be obtained by calculating a signal expectation using the neutrino effective area as in Eqn. 7.2, although for the reader, the precision of such a calculation is limited by interpolation between the given curves for different declinations.

Chapter 8

Conclusions & Future Outlook

The first year of data collected with the completed AMANDA-II neutrino telescope has been analyzed and the northern sky searched for spatially coincident excesses from astrophysical neutrino sources. The search sample is consistent with a randomized background of terrestrial atmospheric neutrinos, with no statistically significant point-source excesses found. AMANDA-II is currently the world's most sensitive neutrino detector, attaining average flux upper limits (90% C.L.) as low as

$$E_\nu^2 \frac{d\Phi_\nu}{dE_\nu} = 2 \times 10^{-7}\,\mathrm{GeV\,cm^{-2}\,s^{-1}} \tag{8.1}$$

with 197 days effective live-time.

8.1 Markarian 501 & the ν/γ Ratio

In Fig. 8.1, the muon neutrino flux upper limit on the AGN blazar Markarian 501 obtained in this analysis (Table 7.1) is compared to the intrinsic gamma ray spectrum at the source in the year 1997 when the blazar was in a flaring state and one of the loudest gamma-ray sources in the sky.

As can be seen in the figure, the intrinsic gamma ray spectrum is not well described by a power law, but rather the spectral index varies between $-1.7 < \alpha <$

−2.2 in the energy regime shown. The AMANDA-II neutrino flux upper limit is shown for two different spectral indicies, $\alpha = -2$ and $\alpha = -1.8$, to give some sense of how the upper limit varies with spectral index.

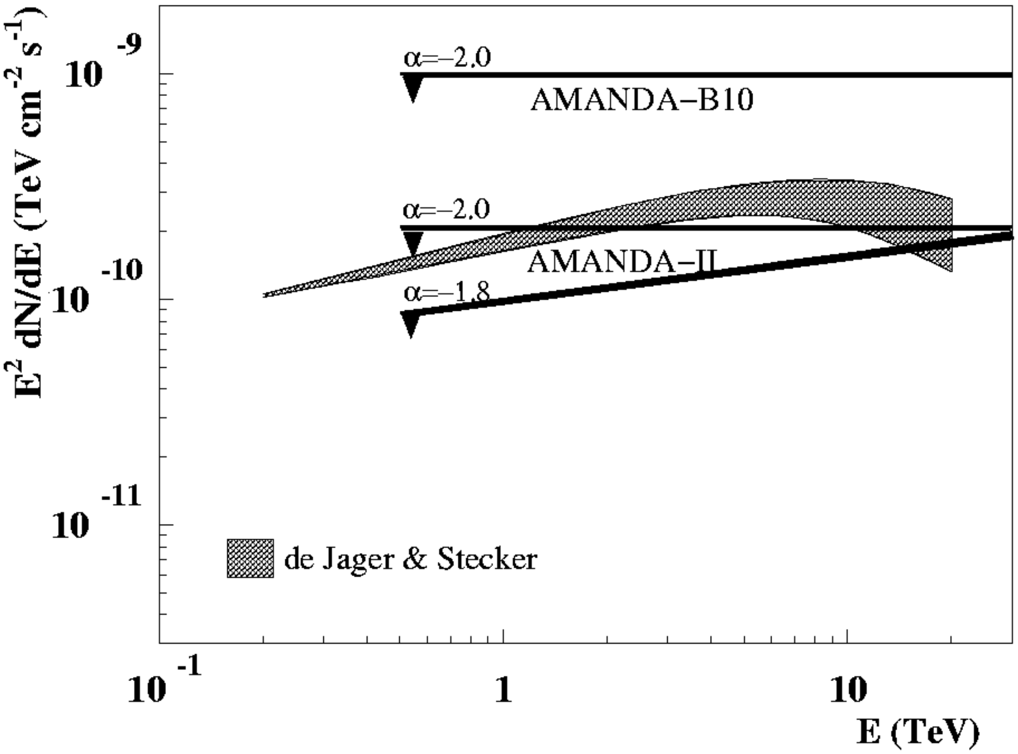

Figure 8.1: The AMANDA-II average flux upper limit (90% C.L.) (197 days live-time) for two assumed spectral indicies (α) is compared to the intrinsic γ-ray flux of Markarian 501 as observed in 1997 by the HEGRA system of air Cerenkov telescopes after correction for IR absorption by de Jager and Stecker [87]. The shaded area is bounded by two curves corresponding to different models of galactic luminosity evolution. For comparison, the AMANDA-B10 result [67] is also shown.

Also shown in Fig. 8.1 is the flux limit obtained in 1997 with the AMANDA-B10 sub-detector [67], demonstrating an improvement in sensitivity due to increased detection volume and improved background rejection.

As AMANDA's sensitivity continues to improve, so does its physics diagnostic potential. As demonstrated by the case of Markarian 501, AMANDA-II has improved over it's predecessor, AMANDA-B10, to reach the important benchmark of sensitivity to neutrino flux of the same magnitude as the gamma ray flux from one of the loudest suspected sites of cosmic ray acceleration. With more exposure time, AMANDA-II may soon be able to probe the ν/γ production ratio of several suspected sites of cosmic ray acceleration.

8.2 Outlook

The AMANDA-II database has quadrupled since the first year of data presented here was collected in 2000. Data collected in years 2001-2003 are now being processed and should improve the average neutrino sensitivity by a factor 2 to 3.

Future searches for neutrino excess may also benefit from a recently developed un-binned search technique [88]. By using the width of the muon track reconstruction in likelihood space (discussed in Chapter 4), the technique allows one to evaluate the relative contributions of each event to the significance of detection at all points in the sky, eliminating the need for a search bin configuration and shifting of bins at the expense of trials penalties. The technique also has the potential to more accurately pinpoint the locations of any excesses which may appear.

AMANDA-II has also benefited from recent hardware upgrades, most notably the added capability to read out entire pulse waveforms using a transient waveform recorder (TWR) system installed on 576 OM channels. The TWR is designed to extend the dynamic range of the OMs by a factor 100, and can handle large muon trigger rates with virtually no dead-time. Information may be extracted from individual waveforms to aid in energy resolution and background rejection, especially for the analysis of UHE events.

8.2.1 IceCube

As first predicted in the 1960s, it is likely that an effective detection area on the order of a kilometer square will be needed to collect astrophysical neutrinos at a sufficient rate to do astronomy [89]. As demonstrated by Fig. 2.2, AMANDA-II does not have sufficient effective area to detect sources which are expected to appear at or below the Waxman-Bahcall flux upper bound. The planned km^2 IceCube array will most likely be the first neutrino telescope to attain a sensitivity below this limit.

The IceCube array, to be deployed over 2004-2010, will comprise 4800 digital optical modules on 80 strings at depths between 1400 m and 2400 m, instrumenting a cubic kilometer of fiducial volume. The DOMs will be spaced at approximately 100 m intervals along the strings, leading to an energy threshold of $E_\nu > 10\,\mathrm{TeV}$. A simulated muon track in the completed array is pictured in Fig. 8.2. Simulations predict IceCube will attain a sensitivity to point sources of $E^2 d\Phi_\nu/dE_\nu < 1 \times 10^{-9}\,\mathrm{GeV\,cm^{-2}\,s^{-1}}$ with three years live-time.

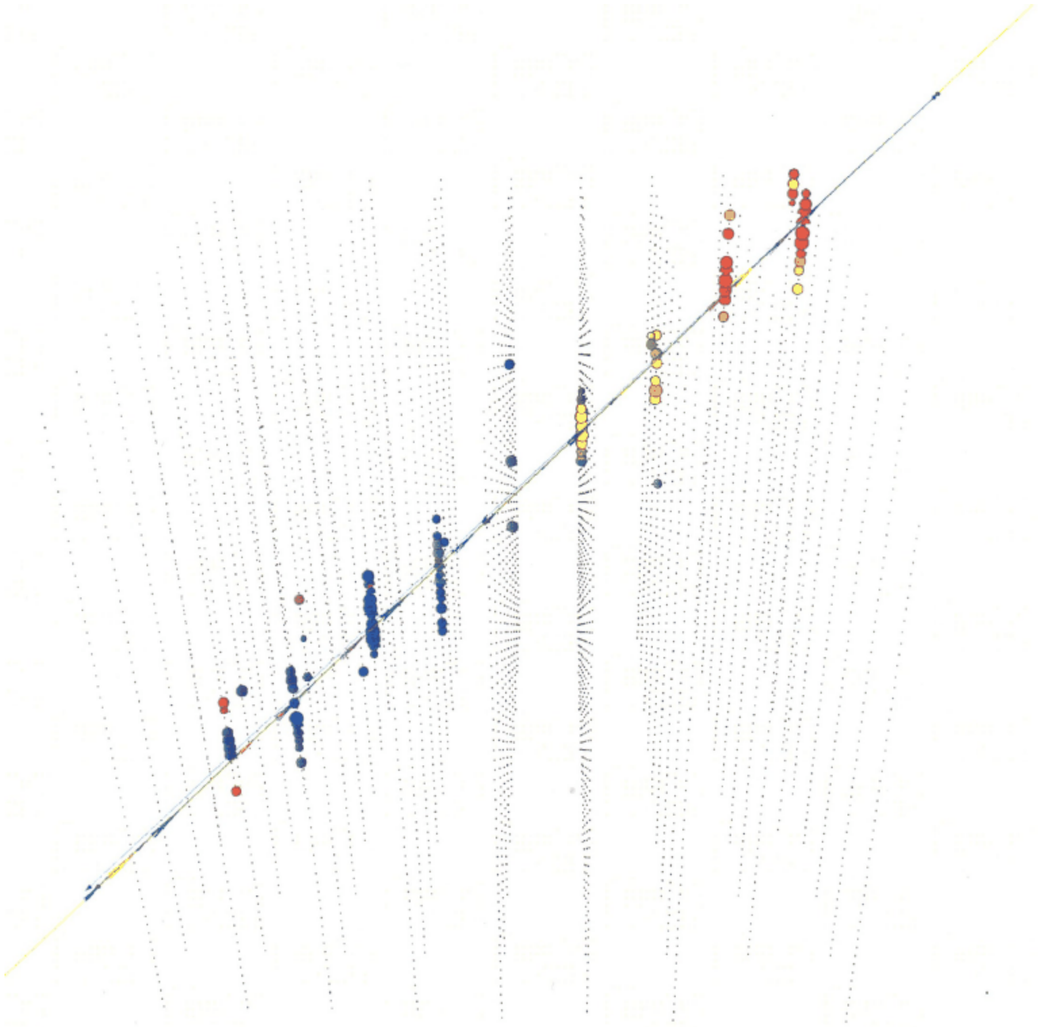

Figure 8.2: Simulation of a muon event in the IceCube neutrino observatory, to be completed in 2010. From [64].

Bibliography

[1] J. G. Learned and K. Mannheim. *Ann. Rev. Nucl. Science*, 50 (2000) 679–749.

[2] R. C. Hartman *et al.*. *Astrophys. J. Suppl. Ser.*, 123 (1999) 79–202.

[3] F. A. Aharonian and G. Heinzelmann. *Nucl. Phys. B (Proc. Suppl.)*, 60 (1998) 193–198.

[4] A. A. Watson. *Phys. Rep.*, 333 (2000) 309–27.

[5] X. Bertou, M. Boratav, and A. Letessier-Selvon. *Intl. J. Mod. Phys.*, A15 (2000) 2181–224.

[6] P. Bhattacharjee and G. Sigl. *Phys. Rept.*, 327 (2000) 109.

[7] M. Takeda *et al.*. *Astroparticle Phys.*, 19 (2003) 447–462.

[8] J. N. Bahcall. *Neutrino Astrophysics* (Cambridge University Press) (1989).

[9] B. Bratton *et al.*. *Phys. Rev. D*, 37 (1988) 3361.

[10] R. Bionta *et al.*. *Phys. Rev. Lett.*, 58 (1987) 1494.

[11] K. Hirata *et al.*. *Phys. Rev. D*, 38 (1988) 448.

[12] K. Hirata *et al.*. *Phys. Rev. Lett.*, 58 (1987) 1490.

[13] The DUMAND Collaboration. *DUMAND-II proposal* (1988). HDC-2-88.

[14] S. Matsuno *et al.*. *Nucl. Inst. & Meth. in Phys. Res.*, A276 (1989) 359–66.

[15] L. K. Resvanis *et al.*. In *Proc. Honolulu Workshop on High Energy Neutrino Astrophys.*, V. J. Stenger, J. G. Learned, S. Pakvasa, and X. Tata, eds. (World Scientific, Singapore) (March 1992) pp. 325–53.

[16] The ANTARES Collaboration. *A deep sea telescope for high energy neutrinos.* `astro-ph/9907432` (July 1999).

[17] C. de Marzo. *Nucl. Phys. B (Proc. Suppl.)*, 87 (2000) 33–5.

[18] I. A. Belolaptikov *et al.*. *Astroparticle Phys.*, 7 (1997) 263–82.

[19] J. Ahrens *et al.*. *Phys. Rev. D*, 66 (2002).

[20] Y. Fukuda. *Phys. Rev. Lett.*, 81 (1998) 1562–1567.

[21] T. Montaruli. *Proceedings of the 27th International Cosmic Ray Conference, Hamburg, Germany*, 81 (2001) 1069–1072.

[22] M. Goodman. *Proceedings of the 27th International Cosmic Ray Conference, Hamburg, Germany*, 81 (2001) 1085–1088.

[23] F. Halzen and A. Martin. *Quarks and Leptons* (John Wiley & Sons) (1984).

[24] T. Gaisser. *Cosmic Rays and Particle Physics* (Cambridge University Press) (1990).

[25] R. Gandhi, C. Quigg, M. H. Reno, and I. Sarcevic. *Astroparticle Phys.*, 5 (1996) 81–110.

[26] E. Fermi. *Phys. Rev.*, 75(8) (1949) 1169–1174.

[27] E. Fermi. *Astrophys. J.*, 119 (1954) 1–6.

[28] J. Bahcall and E. Waxman. *Phys. Rev. D*, 59 (1999).

[29] E. Waxman. *Astrophys. J.*, 452 (1995) L1.

[30] J. Bahcall and E. Waxman. *Phys. Rev. D*, 64 (2001) 023002.

[31] A. Y. Neronov and D. V. Semikoz. *Phys. Rev. D*, D66 (2002).

[32] C. Distefano, D. Guetta, E. Waxman, and A. Levinson. *Astrophys. J.*, 575 (2002) 378.

[33] A. Levinson and E. Waxman. *Phys. Rev. Lett.*, 87 (2001).

[34] J. Blanco-Pillado, R. Vazquez, and E. Zas. *Phys. Rev. Lett.*, 78 (1997) 3614.

[35] K. Capelle, J. Cronin, G. Parente, and E. Zas. *Astroparticle Phys.*, 8 (1998) 321.

[36] A. Letessier-Selvon. *Nucl. Phys. Proc. Suppl.*, 91 (2000) 473.

[37] X. Bertou *et al.*. *Astroparticle Phys.*, 17 (2002) 183.

[38] M. J. M. Sasaki, Y. Asaoka. *Astroparticle Phys.*, 19 (2003) 37.

[39] G. Hou and M. Huang. In *Proc. of the 1st NCTS Workshop on Astropart. Phys.* (Kenting, Taiwan) (2001) .

[40] D. Cline and F. Stecker. *Science white paper from UCLA Workshop on High Energy Neutrino Astrophysics*, (2000).

[41] G. Domogatsky. *Nucl. Phys. Proc. Suppl.*, 110 (2002) 504.

[42] S. Basa. In *Proc. 19th Texas Symposium on Relativistic Astrophysics*, E. Aubourg *et al.*, eds. (Paris, France) (2000) .

[43] C. Spiering. In *Proc. 8th International Workshop on Neutrino Telescopes* (Venice) (Feb. 1999) .

[44] J. Knödlseder. *Astron. & Astrophys.*, 360(2) (2000) 539–548.

[45] M. Casseánd J. Paul. *Astrophys. J.*, 237 (1980) 236–246.

[46] F. Aharonian *et al.*. *Astron. & Astrophys.*, 393 (2002) L37–L40.

[47] Y. Butt *et al.*. *Astrophys. J.*, 597 (2003) 494–512.

[48] R. Klebesadel, R. Strong, and L. Olson. *Astrophys. J. Letters*, 182 (1973) L85.

[49] C. Meegan *et al.*. *Nature*, 355 (1992) 143.

[50] T. Piran. *Phys. Rep.*, 314 (1999) 575–667.

[51] E. Costa *et al.*. *Nature*, 387 (1997) 783.

[52] J. van Paradijs *et al.*. *Nature*, 386 (1997) 686.

[53] R. Hardtke, K. Kuehn, and M. Stamatikos. In *Proc. of the 28th international Cosmic Ray Conference*, T. Kajita *et al.*, eds. (Tokyo) (2003) p. 2717.

[54] D. Jackson. *Classical Electrodynamics* (Wiley, N.Y.) (1996).

[55] D. E. Groom *et al.*. *European Phys. J.*, C15 (2000) 1.
URL `http://pdg.lbl.gov`

[56] G. Hill. *Experimental and Theoretical Aspects of High Energy Neutrino Astrophysics*. Ph.D. thesis, University of Adelaide (1996).

[57] C. H. V. Wiebusch. *The Detection of Faint Light in Deep Underwater Neutrino Telescopes*. Ph.D. thesis, RWTH (Rheinisch-Westfälische Technische Hochschule), Aachen (1995).

[58] H. Sobel. *Nucl. Phys. B (Proc. Suppl.)*, 91 (2001) 127–33.

[59] P. B. Price. In *Proc. Zeuthen Workshop on Simulation and Analysis Methods for Large Neutrino Telescopes*, C. Spiering, ed. (July 1998) pp. 120–131.

[60] C. Walck. *A study of life and death of the AMANDA detector*. AMANDA internal, in preparation.
URL `http://www.physto.se/ walck/amanda/livedead/`

[61] M. Ribordy. *AMANDA/2000 data statistics, OM selection and retriggering proceedure*. AMANDA Int. Rep. 20020601.

[62] I. Taboada. *Amanda cross talk cuts*.
URL `http://www.fis.usb.ve/ itaboada/private/amanda/xtalk/xtalk.html`

[63] D. Chirkin and W. Rhode. *Muon monte carlo: a new high-precision tool for muon propagation through matter*. AMANDA Int. Rep. 20000802.

[64] T. DeYoung. *Observation of Atmospheric Muon Neutrinos with AMANDA*. Ph.D. thesis, University of Wisconsin - Madison (2001).

[65] G. Hill, P. Desiati, A. Karle, and K. Woschnagg. *Evidence for insufficient absorption in the AMANDA monte carlo* (2003). Webpage.
URL `http://amanda.wisc.edu/ghill/absorption/absorption2.html`

[66] J. Ahrens *et al.*. *Calibration of AMANDA-II using the spase air shower array* (2003). Submitted to *Nucl. Instr. and Meth A*.

[67] J. Ahrens *et al.*. *Astrophys. J.*, 583 (2003) 1040.

[68] P. Doksus. private communication.

[69] A. Karle. In *Proc. Zeuthen Workshop on Simulation and Analysis Methods for Large Neutrino Telescopes*, C. Spiering, ed. (July 1998) pp. 174–185.

[70] D. Pandel. Ph.D. thesis, Humboldt University, Berlin (1996).

[71] G. Japaridze and M. Ribordy. *Photon arrival time distribution convoluted to a gaussian time measurement uncertainty*. AMANDA Int. Rep. 20031201.

[72] C. Wiebusch. In *Proc. Zeuthen Workshop on Simulation and Analysis Methods for Large Neutrino Telescopes*, C. Spiering, ed. (July 1998) pp. 302–316.

[73] W. H. Press, S. A. Teukolsky, W. T. Vetterling, and B. P. Flannery. *Numerical Recipes in C: The Art of Scientific Computing* (Cambridge University Press) (1995).

[74] G. Hill. *An introduction to efficient sampling techniques*.
URL `http://www.amanda.wisc.edu/simulation/`

[75] J. Neyman. *Phil. Trans. Royal Soc. London, Series A*, 236 (1937) 333–80.

[76] G. J. Feldman and R. D. Cousins. *Phys. Rev. D*, 57 (1998) 3873–89.

[77] G. Hill and K. Rawlins. *Astroparticle Phys.*, 19 (2003) 393–402.

[78] R. Cousins and V. Highland. *Nucl. Inst. & Meth. in Phys. Res.*, A320 (1992) 331–335.

[79] G. Hill. *Phys. Rev. D*, 67 (2003) 118101.

[80] J. Conrad, O. Botner, A. Hallgren, and C. Perez de los Heros. *Phys. Rev. D*, 67 (2003) 012002.

[81] T. Becka. *Experience with 2001 online processing - and proposal for 2002*. AMANDA Int. Rep. 20020102.

[82] P. Steffen. *Direct-walk II (improved version of direct walk)*. AMANDA Int. Rep. 20020201.

[83] P. Lipari and T. Stanev. *Phys. Rev. D*, 44 (1991) 3543–54.

[84] S. Young. *A Search for Point Sources of High Energy Neutrinos with the AMANDA-B10 Neutrino Telescope*. Ph.D. thesis, University of California, Irvine (2001).

[85] Y. Uchihori *et al.*. *Astroparticle Phys.*, 13 (2000) 151–160.

[86] A. B. von Curland. *One the Rejection of Atmospheric Muons in the AMANDA Detector*. Diploma thesis, Humboldt University, Berlin (1998).

[87] O. de Jager and F. Stecker. *Astrophys. J.*, 556 (2002) 738.

[88] T. Neunhoeffer. *Die Entwicklung eines neuen Verfahrens zur Suche nach kosmischen Neutrino-Punktquellen mit dem AMANDA-Neutrinoteleskop*. Ph.D. thesis (2003).

[89] F. H. T. K. Gaisser and T. Stanev. *Phys. Rept.*, 258 (3) (1995) 173.

[90] A. Karle. private communication.

APPENDICIES

Appendix A

Threshold Determination from TOTs

A.1 Introduction & Motivation

As introduced in §3.3.2, a new method for determining AMANDA thresholds (or the ORB-prompt pulse single photo-electron equivalent amplitude) from minimum bias TOT data has been developed. The single photon equivalent amplitudes are required inputs in the AMASIM geometry calibration file. This topic is important because a 30% uncertainty in thresholds over the entire detector could result in up to a 10% or 15% uncertainty in detector trigger rate. Determining thresholds by direct measurement with a scope requires that the measurement be repeated every time a change in hardware settings is made. The new method can be applied to data for which no scope measurements are available. The method can also be used to investigate the time dependence of the thresholds over the course of a season. The weakness of this method is that it depends on the TOT being accurately described by the detector simulation. Qualitative agreement between data and Monte Carlo TOT distributions is demonstrated after the new method is applied. In Monte Carlo tests, the method is self-consistent to within 5%. The absolute accuracy of the method can be checked by direct measurement.

The AMANDA-II amasim electronics file contains several parameters, including the DMADD threshold and the prompt pulse amplitude corresponding to a single photo-electron (or SPE). As seen in Fig. A.1, a schematic describing a typical AMANDA-II channel, an optical signal arrives from the OM and is converted into an electrical signal by the fast ORB. This signal is referred to in this report as the "prompt pulse." AMANDA-II Monte Carlo simulations require as input the most frequently occurring amplitude (peak of the distribution) corresponding to an SPE (point A in Fig. A.1). In this report, SPE amplitude is measured in millivolts. Also required in the geometry file is the threshold setting of the DMADD (point B). The threshold is set directly, and is thus known to within the precision of the DMADD (about 5% [90]), whereas the SPE prompt pulse amplitude is set indirectly by the fast ORB gain which can be different from one OM to the next.

In this analysis, "relative threshold" is defined as the fixed DMADD threshold setting divided by the prompt pulse SPE equivalent amplitude.

$$relative\ threshold = \frac{DMADD\ threshold}{prompt\ pulse\ SPE\ amplitude}$$

So when we refer to "relative threshold", we are really discussing the prompt pulse SPE amplitudes . This definition is constructed to allow us to more easily develop a method that is applicable to any module regardless of its absolute threshold. Obviously, given the known DMADD threshold, one can determine the prompt pulse SPE amplitude from the relative threshold.

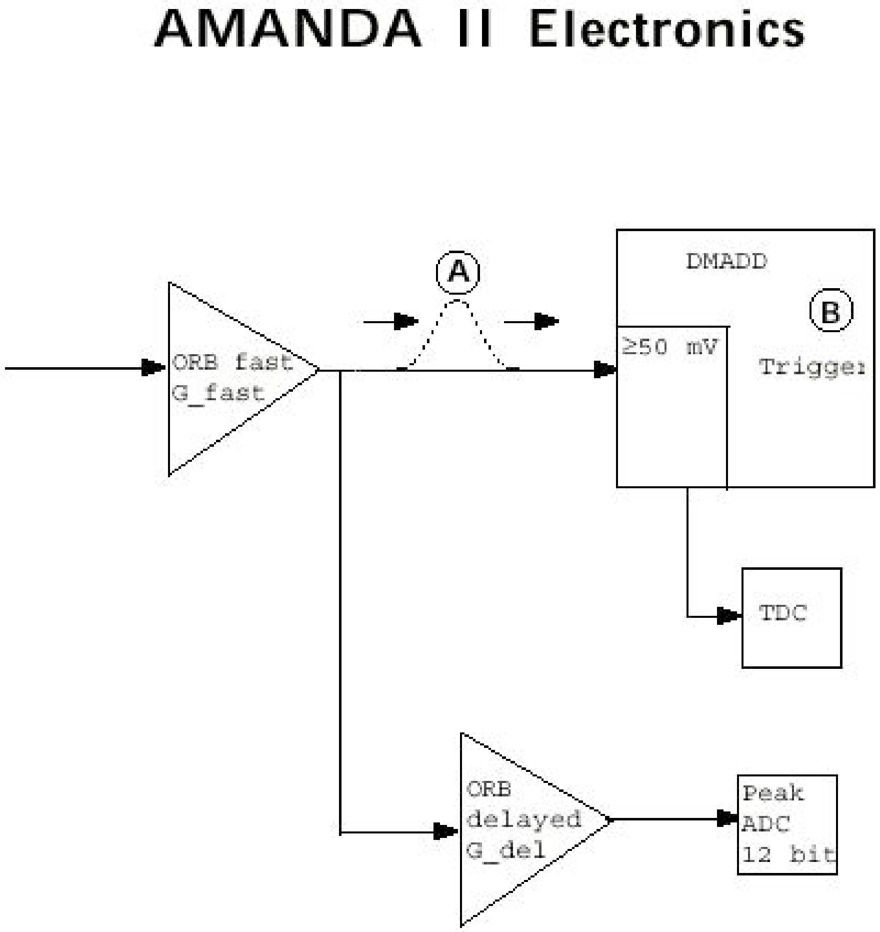

Figure A.1: Schematic of a typical AMANDA-II channel.

The Time-Over-Threshold (TOT) is defined, as usual, as the amount of time for which the prompt pulse signal exceeds the DMADD threshold. It stands to reason that the lower the relative threshold (the higher the SPE prompt pulse amplitude), the longer the measured TOT. This relationship is used to extract the relative threshold (and thus the SPE amplitudes) from TOT data.

In this appendix, the method, its implementation, and results when applied to AMANDA-II data are described.

A.2 Method

We begin by determining the function $\mathcal{T}(TOT)$ which returns a relative threshold given a TOT. This function is computed numerically from the digitized average pulses in the AMANDA-II pulse file. For the time being, it is assumed that all standard AMANDA-II pulses (of a given category, i.e. optical, DOM, ...) are identical in shape. Furthermore, we assume pulses vary only in their amplitudes, and are not stretched out in time. This is believed to be a reasonable assumption because each electron propagates through the dynode stack of the PMT independently.

To compute $\mathcal{T}(TOT)$, the TOT is measured as we move the relative threshold up the pulse. The resulting $\mathcal{T}(TOT)$ function is fit to a degree 5 polynomial. Shown in Fig. A.2 is a typical AMANDA-II prompt pulse and the corresponding $\mathcal{T}(TOT)$ function. Similar figures for each of the pulses in the AMANDA-II pulse file are shown in Figs. A.5 and A.6.

Now that the $\mathcal{T}(TOT)$ functions have been obtained, one must somehow choose an appropriate TOT from a TOT distribution to achieve the correct threshold. From a first look at some typical AMANDA-II TOT distributions (Fig. A.3), it is not neces-

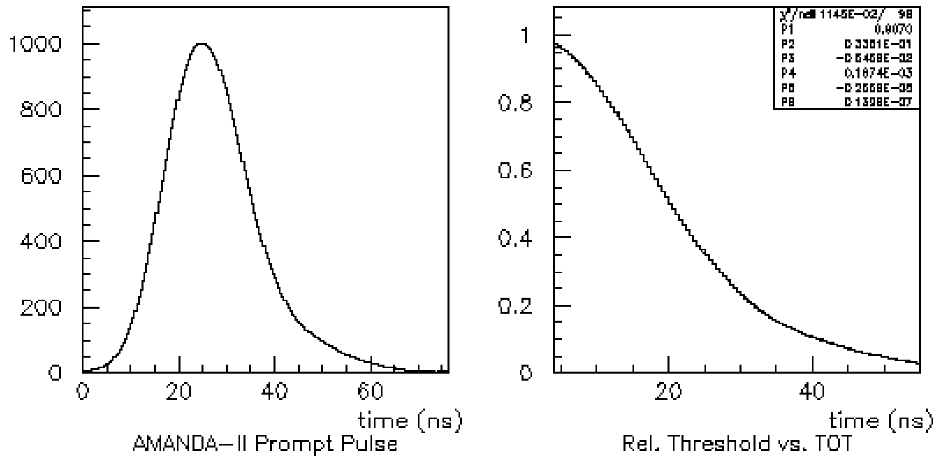

Figure A.2: (a) A typical AMANDA-II prompt pulse with amplitude normalized to 1000, and (b) its corresponding $\mathcal{T}(TOT)$ function (computed numerically). An increase in relative threshold is a decrease in absolute SPE amplitude and thus a decrease in TOT.

sarily obvious how to choose the correct TOT. Three methods have been investigated.

The first attempt was to use the TOT corresponding to the *peak* of the TOT distribution for each channel. The results showed that using this choice of TOT, we could determine the SPE amplitude to within only 30 to 50 percent.

Next the *median* TOT of the distribution was tried. This method gets closer, down to a 25 or 30 percent error.

Finally, the *average threshold* was computed for each OM by summing over the number of events of each TOT multiplied by the threshold corresponding to each TOT and dividing by the total number of events. This is actually the worst, resulting in SPE amplitudes that are up to 80% off from the true value.

The relative errors of the calculated amplitude versus calculated SPE amplitude as just discussed appear in Fig. A.4(a). In this plot, black corresponds to the peak

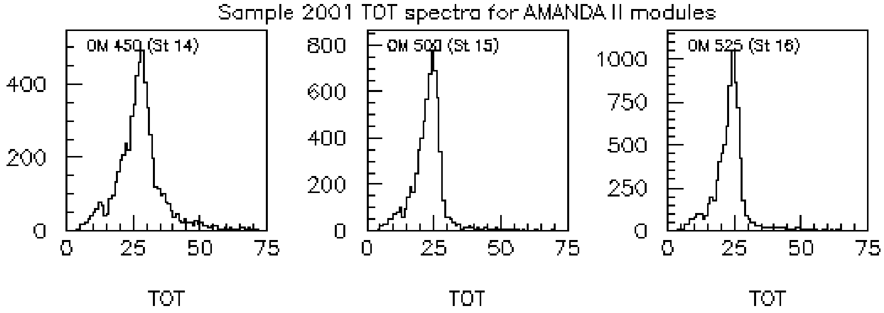

Figure A.3: Typical AMANDA-II TOT distributions.

TOT method, red to the median method, and blue to the average threshold method. One immediately notices that the relative error of the method is dependent on the actual amplitude sought.

This observation suggests that instead of simply calculating the threshold and SPE amplitude from a TOT read directly from the distribution, one can add an extra step to reduce the error. Once an SPE amplitude is computed using a given method, we can use the monte-carlo to find a function which returns the actual amplitude given the calculated amplitude. This function is exactly what is plotted in Fig. A.4(b). Observe that the red curve (median method) comes closest to a straight line with the fewest outlying points, but having a slope less than unity. Clearly, the red curve (median method) will give the best fit to a simple polynomial and will result in the smallest error. In practice, one should choose to deal not with amplitudes, but with relative thresholds, to allow the method to be applied modules of the same type but with different absolute thresholds. As such, the function $\Theta(\mathcal{T})$is defined as that which takes a calculated relative threshold and returns the corrected relative threshold.

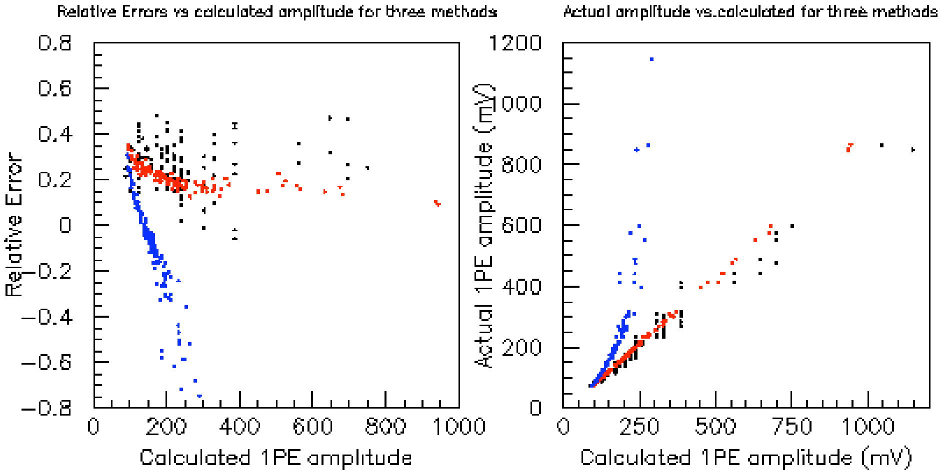

Figure A.4: (a) Relative error of three different $\mathcal{T}(TOT)$ functions. The black points correspond to the peak method, red to the median method, and blue to the average threshold method. (b) Actual Monte Carlo SPE amplitude vs. calculated.

The median method is believed to be more robust than the peak or average threshold methods because it is less sensitive to the tails and strange features that may be unique to individual OM TOT distributions. For this particular pulse, the method of obtaining thresholds as described in this section is accurate to within 5% on monte-carlo.

A.3 Implementation

A collection of scripts and paw kumacs collectively dubbed *Threshold Extraction Algorithms* or *TEA*, is available from the AMANDA CVS archive. There is a README file with instructions on how to use the package included with the code.

A sample of 50,000 events seems to provide adequate statistics for both the Monte Carlo and data phases of the analysis.

A.4 AMANDA-2000 Thresholds

The TEA method has been applied to AMANDA-II minimum bias data from year 2000. Shown in this section are the details of the analysis and a discussion of the time dependence and accuracy of the calculated thresholds.

A.4.1 $\mathcal{T}(TOT)$ & $\Theta(\mathcal{T})$ Determination

Figs. A.5 and A.6 show each of the pulse shapes used in this analysis. Fig. A.7 shows the corresponding $\Theta(\mathcal{T})$ functions fit with a second degree polynomial. Although modules identified with pulse ID 7 have normal behaving TOTs, there are not enough of them to make a good fit for the $\Theta(\mathcal{T})$ function, so modules with this pulse ID must be excluded.

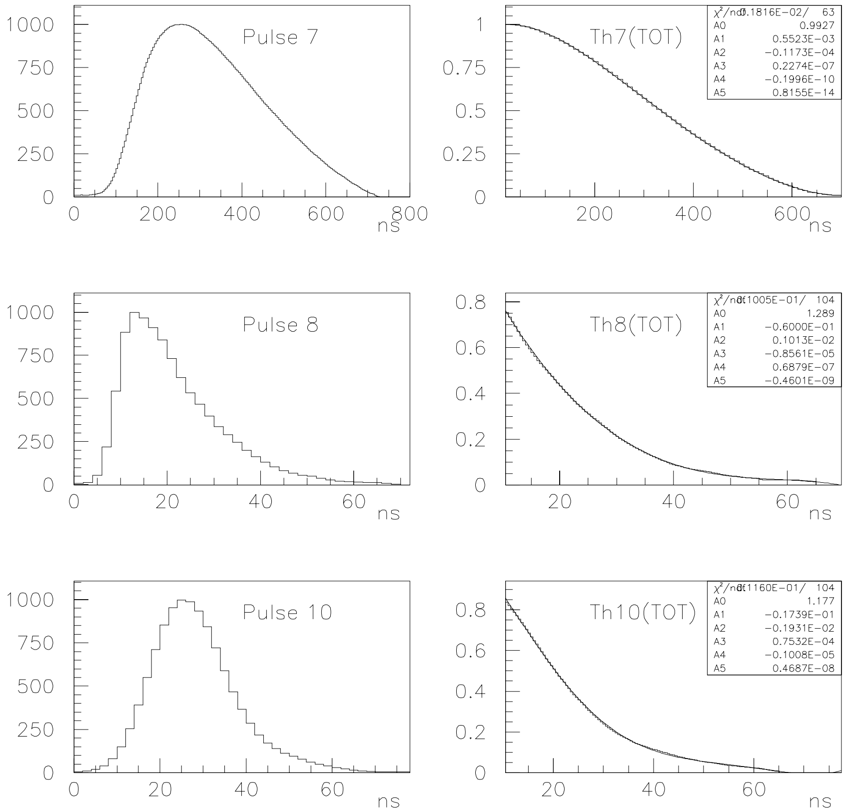

Figure A.5: AMANDA-II pulse shapes used in this analysis, along with their corresponding $\mathcal{T}(TOT)$ functions. Pulse 7: Hybrid str. 11-13: electrical; Pulse 8: Hybrid str. 11-13: optical; Pulse 10: Hybrid str. 14-19: optical.

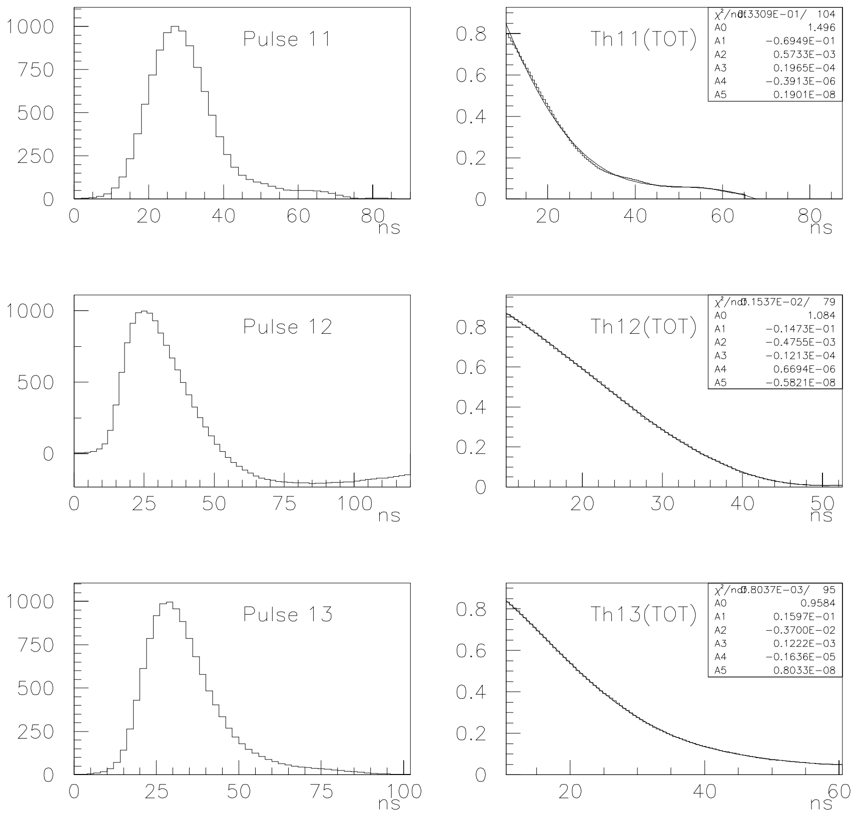

Figure A.6: AMANDA-II pulse shapes used in this analysis, along with their corresponding $\mathcal{T}(TOT)$ functions. (cont.) Pulse 11: DOM LED str. 18; Pulse 12: Laser Diode controlled HV: optical; Pulse 13: dAOM LED output controlled HV: optical.

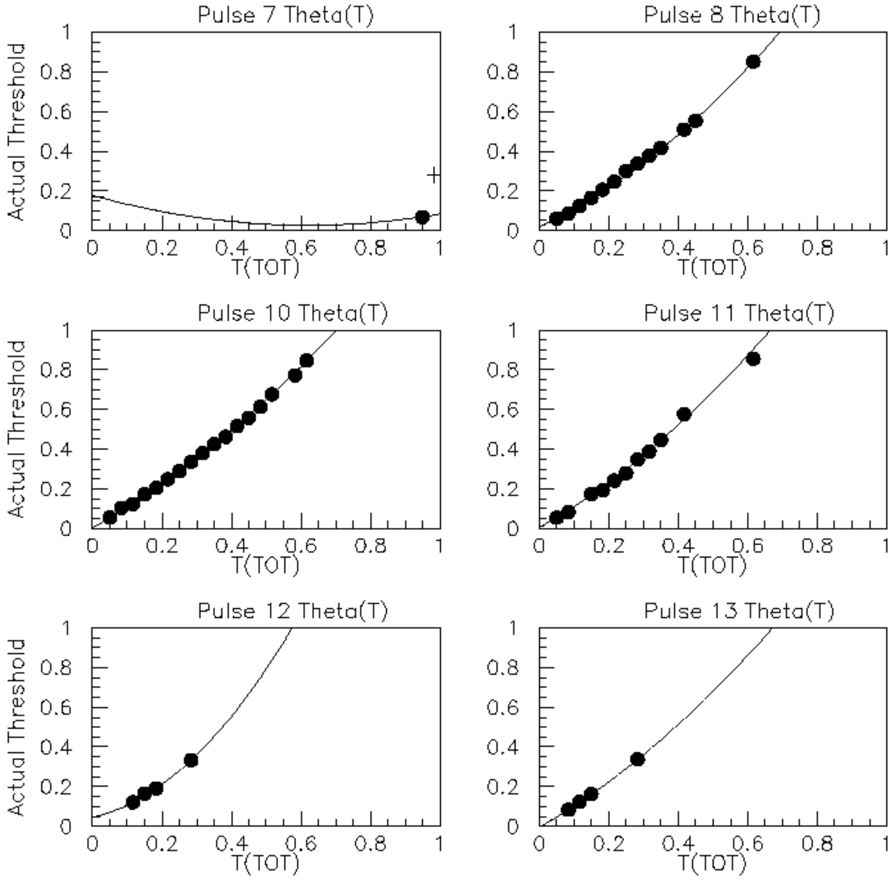

Figure A.7: Shown are $\Theta(\mathcal{T})$ functions for each of the pulses used in the analysis. Notice the poor quality of the fit for pulse 7 due to low statistics; only a few modules have this pulse, so they must be excluded from this analysis.

The $\mathcal{T}(TOT)$ functions for this analysis were computed numerically based on the pulse shapes from version 2.01 of the AMASIM pulse file. Fifth degree polynomial fits of these functions were used in this analysis:

$$\mathcal{T}(TOT) = a_0 + a_1\mathcal{T} + a_2\mathcal{T}^2 a_3\mathcal{T}^3 + a_4\mathcal{T}^4 + a_5\mathcal{T}^5$$

The fit parameters for each pulse used are found in the following table:

$\mathcal{T}(TOT)$ fit parameters

ID	a_0	a_1	a_2	a_3	a_4	a_5
7	1.0	5.5×10^{-4}	-1.2×10^{-5}	2.3×10^{-8}	-2.0×10^{-11}	8.2×10^{-15}
8	1.3	6.0×10^{-2}	1.0×10^{-3}	-8.6×10^{-6}	6.9×10^{-8}	-4.6×10^{-9}
10	1.2	-1.7×10^{-2}	-1.9×10^{-3}	7.5×10^{-5}	-1.0×10^{-6}	4.7×10^{-9}
11	1.5	-6.9×10^{-2}	5.7×10^{-4}	2.0×10^{-5}	-3.9×10^{-7}	1.9×10^{-9}
12	1.1	-1.5×10^{-2}	4.8×10^{-4}	-1.2×10^{-5}	6.7×10^{-6}	-5.8×10^{-9}
13	1.4	-5.8×10^{-2}	7.7×10^{-4}	-3.0×10^{-7}	-6.3×10^{-8}	3.5×10^{-10}

The $\Theta(\mathcal{T})$ functions from this analysis have been fit to a second degree polynomial:

$$\Theta(\mathcal{T}) = b_0 + b_1\mathcal{T} + b_2\mathcal{T}^2$$

$\Theta(\mathcal{T})$ fit parameters

ID	b_0	b_1	b_2
8	1.835×10^{-2}	8.100×10^{-1}	8.755×10^{-1}
10	3.711×10^{-3}	9.746×10^{-1}	6.326×10^{-1}
11	4.273×10^{-3}	9.852×10^{-1}	7.695×10^{-1}
12	4.664×10^{-2}	3.848×10^{-1}	2.213×10^{0}
13	-5.240×10^{-3}	1.002×10^{0}	7.359×10^{-1}

A.4.2 Quality Screening

A normal TOT distribution looks something like the ones shown earlier in Fig. A.3. The TEA method will not work on an anomalous TOT distribution. Therefore, each module's TOT distribution must be plotted and visually inspected. If a TOT distribution is deemed anomalous, the SPE amplitude must be determined by another method.

It is observed that many of these OMs can be categorized by one of a few specific types of TOT anomalies, representative examples of which are shown in Fig. A.8. Many of these anomalous channels are already on the 2000 bad channel list, but unfortunately about 80 of them are not. Since the TOT distributions of these modules do not conform to what we deem as normal, no thresholds can be obtained for these channels by this method. One may be able to find times during the season when some of these modules were behaving normally, but it would in some way seem better to have all of the thresholds taken from the same time. In this report, a first pass at this procedure is described. If the TOT distribution was bad on day 180, day 49 was checked, and then day 300, taking the threshold result from the first TOT distribution (in the described order) that had normal behavior.

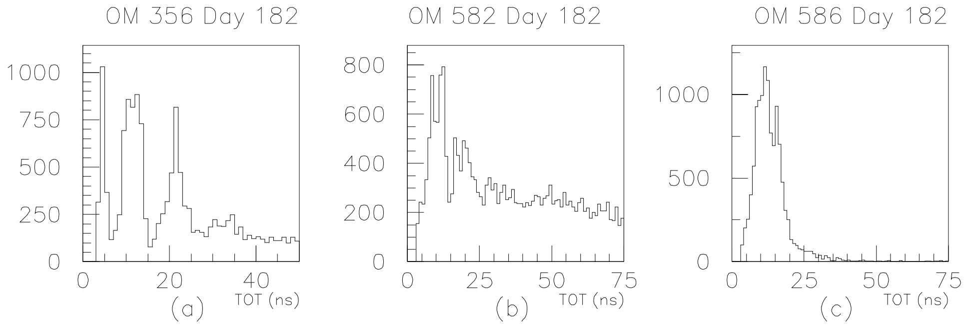

Figure A.8: Categories of TOT anomalies. Triple peak structure (a), "white noise" (b), and abnormally wide (c).

A.4.3 Time Variation

There has been some discussion in the collaboration about eventually implementing a time-dependent Monte Carlo where such parameters as dead OMs and noise rates would be changed to follow the actual behavior of the detector throughout the season. (See for example M. Ribordy's work on OM stability [61].) The TEA method allows one to perform an offline investigation of relative threshold stability over time. The results could then be used in a time-dependent Monte Carlo , or to estimate systematic uncertainty.

To demonstrate this capability the year 2000 data set has been broken into two halves and the time variation from the beginning to the middle, and middle to end of the year plotted in Fig. A.9. Also plotted is the difference from the year 2000 to the year 2001.

From the beginning of 2000 to the middle of 2000, the SPE amplitudes of most modules are stable to within 10%, with an overall downward trend of a few percent. A total of 10 modules die during this period, only one of which appears on the current nominal AMANDA-II bad OM list [61]. Thirteen modules experience more than a 20% change in SPE amplitude. Of these 13, five have normal TOT distributions. The others have slightly anomalous TOT distributions, but not so anomalous as to be excluded from the analysis.

From the middle to the end of 2000, the SPE amplitudes on strings 11-13 increase on average about 5%, while most of the values on strings 14-19 are even more stable than in the first half of the year. Another 10 modules die, none of which are on the nominal AMANDA-II bad OM list. This time, only 3 modules experience more than a 20% change in SPE amplitude, and all 3 have good TOT distributions.

In the austral summer calibration season of 2000 to 2001, the ORB gains of most AMANDA-II modules were changed. The resulting change in SPE amplitudes is evident by the plot on the right side of Fig. A.9. There is an average downward trend for strings 11-13 and a larger average upward trend for strings 14-19 with a typical relative change of up to +50 to +100%, This plot, taken together with the discussion of §A.5, demonstrates the importance of having a method such as TEA to determine SPE amplitudes after the gains have been changed and/or in the absence of direct measurements.

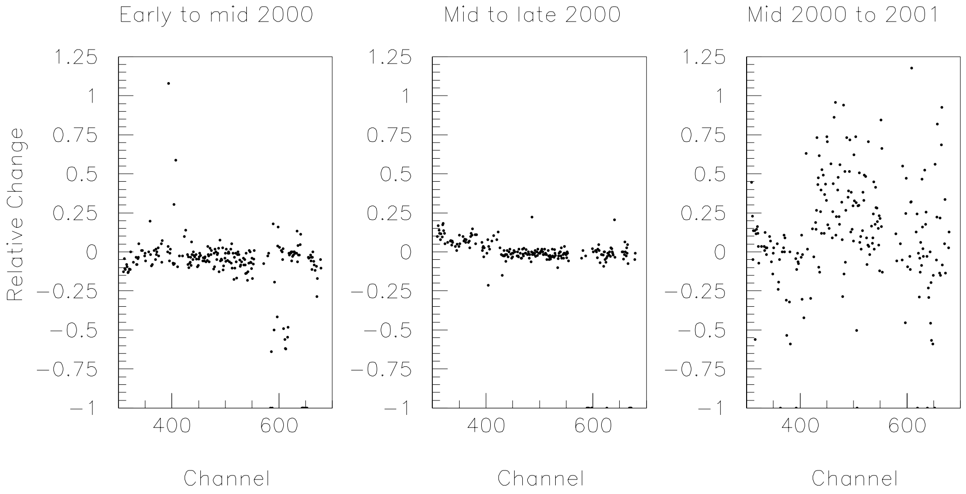

Figure A.9: Variation of the SPE amplitudes with time. Relative change from the beginning of 2000 to mid 2000, left; from mid 2000 to the end of 2000, center; from 2000 to 2001, right.

A.4.4 Accuracy

The best way to test the TEA method would be to compare its results to direct measurements of the prompt pulse amplitude. However, these data are not yet available. In the temporary absence of these data, one can judge qualitatively how well the method works on data by using TEA to obtain a set of thresholds from the data, running a Monte Carlo with those thresholds, and comparing the resulting Monte Carlo TOT distributions to the data.

A Monte Carlo analysis using an electronics file containing the SPE amplitudes as determined by TEA on 2000 data was performed. The TEA method was applied to the resulting Monte Carlo data. The two sets of SPE amplitudes are compared in Fig. A.10(a). From this plot, one observes that the method appears to be self-consistent to with about 5% for the largest fraction of modules. Fig. A.10(b) compares a typical Monte Carlo TOT distribution to the data. Going from the scope-deduced threshold Monte Carlo to the TEA-deduced threshold Monte Carlo , there is a clear shift of the TOT distribution to the left to better match the data

A.5 Systematic Uncertainty in the Detector Trigger Rate

All of the work that has been put into developing TEA methods begs the question, how important is this? Jodi Cooley performed a study where the thresholds were varied to investigate the effect on the trigger rate for atmospheric neutrinos. The results are abbreviated and summarized in the table below.

Effect of Thresholds on Atm. Nu Trigger Rate (Events Per Day)

Change in Thresholds	Trigger	Level 1	Level2
Normal	38.4	36.0	32.4
all down 30%	40.8	38.6	34.9
all up 30%	33.3	30.8	28.0
half down 30%	40.0	36.9	33.7
half up 30%	34.6	34.3	31.6

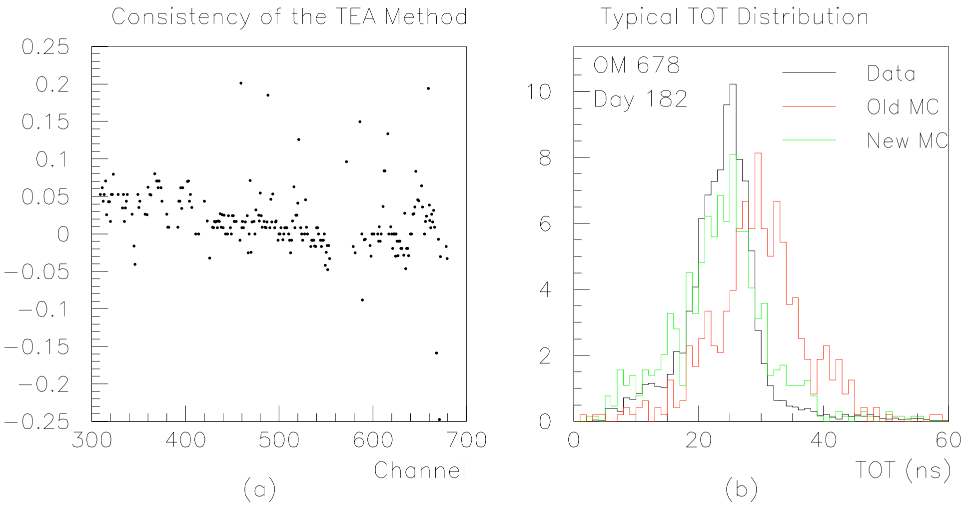

Figure A.10: In figure (a), a Monte Carlo simulation has been run using the SPE amplitudes obtained by the TEA method on 2000 data. Then the TEA method was re-applied to the resulting Monte Carlo data to check the self-consistency of the method. Plotted here is the relative difference between SPE amplitudes as determined from the data and the post-TEA monte-carlo. The figure demonstrates that the TEA methods is self- consistent to within 5% for most modules. In figure (b), two Monte Carlo TOT distributions are compared to the data. The “old MC” (red curve) is the Monte Carlo TOT distribution obtained using the scope-deduced threshold. The “new MC” (green curve) is the distribution resulting when the TEA-deduced threshold is used.

This study shows that if all thresholds were systematically off by 30% (all in the same direction), we could suffer up to a 15% change in event rate from trigger level down to level 2. If only half of the thresholds are systematically above or below the true value by 30%, we suffer by up to 10% in event rate.

Measurements were taken at the pole in February of 2001 to measure the correlation between the delayed and prompt pulse amplitudes. Since these measurements were done after changes in the gain were made for many modules, the results are only valid for 2001 data, assuming that no further changes to gains were made after the measurements were made.

Fig. A.11 is a plot of the percent difference between the SPE amplitudes as deduced from the scope measurements, and the new thresholds computed by the TEA method on 2001 data. If the ORB gains were not adjusted between when the scope measurements were taken and the TEA data were recorded, then the figure indicates large disagreement between the two methods with an overall downward trend going from the scope method to TEA. Since there is not yet data to confirm the validity of one method over the other, Fig. A.11 suggests that our uncertainty in the thresholds could be as much as 50% or more, further motivating this work.

A.6 Outlook

SPE calibration data are currently only available for AMANDA-II channels with normal TOT behavior. If these modules can not be fixed but are still to be used in some way in analysis, SPE amplitudes must be obtained by other means. Thresholds must be re-calculated for channels with normal behavior each time there is a change in gain.

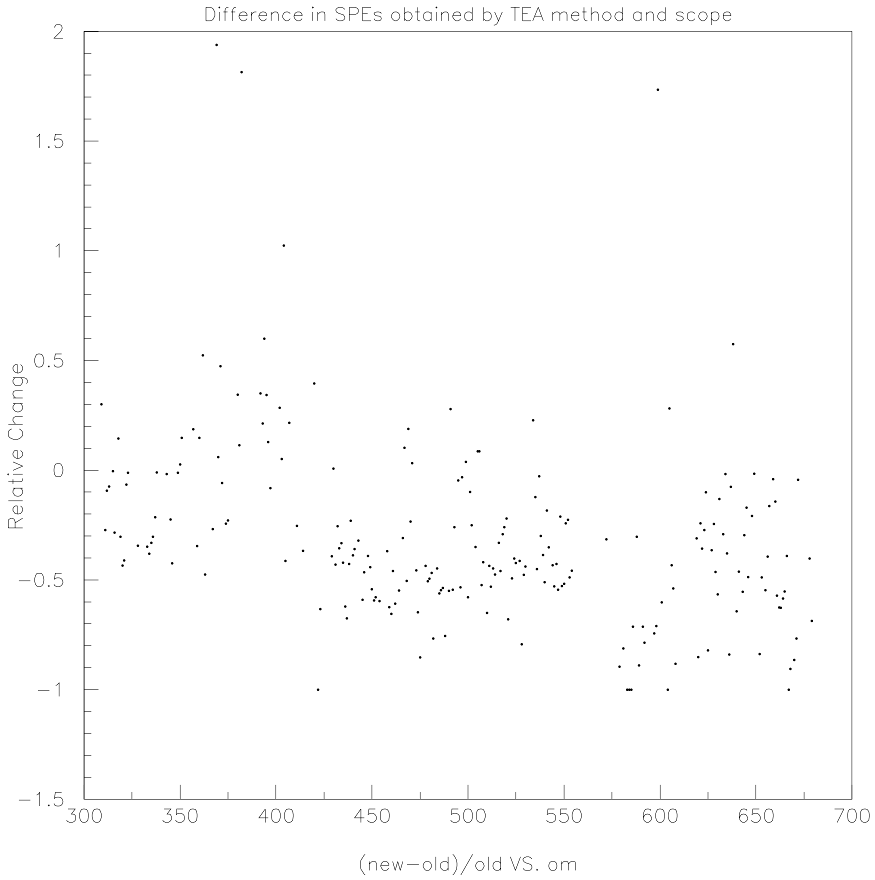

Figure A.11: Difference in SPE amplitudes from the scope-based method, to the new TEA method.

Electrical pulses of B-10 vary with cable length, so it is not possible to produce one characteristic average pulse for these modules. To overcome this feature, it has been proposed to compile an OM waveform database to allow the application of this method to those channels. The database could contain a waveform for each individual module, or representative wave-forms from each type of module and depth if applicable.

Appendix B

Table of Events

The following is a table of the 699 up-going events included in the final search sample (described in chapter §7.1). The table includes the event number, day of the year (counting from January 1, 2000) and the number of seconds into the day, as well as reconstructed Right Ascention, Declination, and N_{ch}, the number of channels fired (after hit-cleaning).

Table B.1: List of Events

Event Num.	Day	Seconds	Rt. Asc. [h]	Declin. [^{o}]	N_{ch}
456320	44	76551	1.93	17.77	53
759791	47	51553	16.50	2.14	26
5676936	48	33373	0.96	65.37	59
6034289	48	38314	0.80	16.82	30
3994675	50	2312	2.48	57.44	30
4436099	50	8086	13.14	48.53	30
4975641	50	15113	13.09	27.94	28
3871583	51	4711	23.10	42.99	33
3115686	51	80876	21.16	39.87	29
4546787	52	15321	23.18	77.35	41
2341138	52	63392	16.73	42.90	31
3021327	52	72601	18.48	41.48	22
5726476	53	23515	21.60	66.35	38
264065	53	34930	18.25	3.97	63
5603009	54	22269	12.93	64.80	29

continued on next page

Table B.1: *continued*

Event Num.	Day	Seconds	Rt. Asc. [h]	Declin. [^{o}]	N$_{\mathrm{ch}}$
1272826	54	48838	10.33	55.13	30
3123122	54	73984	0.23	45.64	31
1216984	55	48113	2.79	25.23	26
1614328	55	53611	14.68	7.93	98
4724656	56	10199	10.15	60.87	25
5090269	56	15027	13.24	48.22	23
5699913	56	23087	5.15	16.04	55
2218950	56	60505	6.03	35.47	50
1028626	57	44833	13.38	15.85	31
1121963	57	46064	22.31	1.30	22
3106760	57	72004	9.20	25.75	51
4826846	58	7458	2.52	10.91	59
5220970	58	12515	14.24	62.76	28
5574398	58	17101	20.89	4.61	121
4894298	59	9493	5.72	33.30	31
2277256	59	60557	8.97	31.01	73
2658001	59	65470	17.74	70.21	33
2854432	59	68006	20.49	47.49	35
5157920	60	11322	18.94	1.60	33
5886750	60	20724	21.78	53.87	27
1283256	60	47633	21.70	41.39	29
3997456	60	82967	21.48	71.11	30
5554292	61	17054	15.84	18.19	64
3315	61	31267	11.16	2.12	63
619215	61	39109	22.93	0.47	30
2390016	61	61830	12.87	66.52	66
4222511	61	85781	14.47	58.68	38
4547414	62	3681	17.53	56.95	29
5392785	62	14882	14.74	32.45	24
6351108	62	27332	8.86	2.64	52
1331839	62	48582	5.34	60.42	44
6098983	63	24988	20.88	35.27	29
151289	63	33227	19.57	13.63	30
3349658	63	75954	7.30	48.65	32
3764681	63	81486	1.69	1.91	38
1025334	64	44898	2.19	5.48	41
4601733	65	5814	5.90	38.68	60

continued on next page

Table B.1: *continued*

Event Num.	Day	Seconds	Rt. Asc. [h]	Declin. [^{o}]	N_{ch}
1583493	65	51689	17.36	13.04	64
1670408	65	52847	18.89	6.20	39
2511909	65	64076	10.31	19.04	26
5627509	66	19289	6.75	2.60	46
1857451	66	56014	6.28	58.20	32
2783371	66	68386	17.85	42.61	36
4984941	67	11458	4.36	2.17	48
5920297	67	23994	6.44	89.88	31
1931466	67	56723	1.05	1.13	33
3520175	67	77718	11.25	37.77	29
3609301	67	78863	20.01	23.28	31
1522129	68	50973	22.15	19.82	56
4023765	68	83410	20.13	83.24	25
5331635	69	14180	1.75	48.77	26
6429891	69	28854	13.16	56.33	38
1135287	69	46362	20.96	39.05	25
4169148	69	85973	9.00	13.47	47
57191	70	31938	23.32	68.27	40
2398046	70	63054	9.24	0.98	41
2509774	70	64541	5.70	34.94	24
5080513	71	12095	4.80	51.52	56
765112	71	40976	20.75	53.38	26
1090911	71	45144	5.93	38.34	31
2783736	71	66775	20.81	69.94	36
898909	72	42306	0.98	54.41	28
4537982	73	2319	4.37	8.44	67
5839478	73	19641	7.66	30.81	79
5920919	73	20730	18.72	53.01	46
3830670	74	81725	4.38	6.10	28
5698902	75	20053	22.10	55.35	34
5949917	75	23454	21.06	38.22	33
2232184	75	61668	13.24	69.71	40
934557	76	43909	2.77	1.47	49
1229568	77	47921	23.82	79.21	39
4810010	78	9428	6.03	59.43	36
194659	78	33770	9.22	17.95	32
722405	78	40767	18.69	29.12	37

continued on next page

Table B.1: *continued*

Event Num.	Day	Seconds	Rt. Asc. [h]	Declin. [^{o}]	N_{ch}
2072549	78	59037	3.06	69.00	33
2851464	78	69593	11.08	35.12	21
1363197	79	48977	16.53	54.19	42
5400981	80	15717	17.91	61.16	31
5472179	81	20554	16.35	80.45	32
6148346	81	29985	2.41	21.99	28
2943743	81	72082	9.29	3.71	87
2973316	81	72494	1.23	23.67	50
3659927	81	82145	23.88	30.11	37
2308452	82	64003	0.84	54.50	27
4373126	83	6909	10.93	56.08	24
5779172	83	26985	8.70	19.13	29
2500629	83	66802	22.74	17.16	31
3524743	83	81433	15.89	40.23	41
5596961	84	24598	6.01	53.01	32
481414	84	37979	23.67	36.52	68
1790620	84	56223	20.05	0.65	37
3908375	84	85431	17.92	12.86	52
4082255	85	1524	21.48	38.62	61
4408836	85	6198	17.70	23.58	43
5509929	85	21930	7.44	56.34	38
5850961	85	26818	22.48	32.26	31
553138	85	38991	12.79	4.40	42
1042680	85	45966	6.82	2.86	26
2412334	85	64581	2.33	53.41	38
2840930	85	70403	19.50	58.26	31
2915911	85	71424	14.38	23.80	32
5213051	86	16891	17.23	20.37	38
1478497	86	51176	20.22	2.32	51
4790963	87	8288	2.46	1.69	41
1105867	87	45419	15.45	53.36	24
1468281	87	50123	8.17	16.14	64
2929338	87	69070	8.31	19.37	76
4058549	87	84303	17.29	41.68	42
5285978	88	14634	2.49	5.52	34
2377102	88	63511	15.26	84.45	48
4567259	89	7138	0.92	56.84	33

continued on next page

Table B.1: *continued*

Event Num.	Day	Seconds	Rt. Asc. [h]	Declin. [^{o}]	N$_{\text{ch}}$
1411443	89	50401	21.82	11.73	69
3797071	89	83184	14.11	33.66	24
715221	90	40728	7.76	38.67	25
2863674	91	70594	16.01	90.00	48
6130048	92	29290	2.84	40.57	29
1976388	93	35354	1.94	53.42	36
4353733	93	67146	20.50	40.04	25
1978706	94	35092	14.49	12.55	61
4072756	94	63877	5.53	1.62	29
2872972	95	46437	4.48	35.08	26
2839606	96	46100	3.84	53.17	30
2415962	97	40902	2.75	23.46	33
5258373	97	79693	22.52	30.70	58
5736570	97	86224	8.88	59.78	48
5827573	98	1069	8.31	50.63	49
1295968	98	25665	23.18	64.10	58
2116378	98	36950	16.47	0.30	47
5068639	98	78314	23.42	19.73	29
5696224	99	517	16.09	56.04	28
4406198	99	68512	9.76	66.55	42
4717507	99	72778	13.00	87.02	25
2051152	100	37312	12.92	0.62	48
3147292	100	53262	7.26	68.92	40
177109	101	10446	9.83	33.37	32
4279269	101	67012	12.41	0.71	24
5959479	102	3928	5.60	15.60	33
2897298	102	47705	19.40	56.47	32
4439572	102	68310	5.53	39.68	25
4451937	102	68477	19.08	36.39	85
5620288	102	84160	6.02	18.07	75
181	103	7967	0.27	54.01	32
2654542	103	43956	8.13	1.43	34
3664277	103	57472	23.77	36.82	23
5737484	103	85871	14.87	14.76	31
597394	104	16752	23.63	53.80	20
3082043	104	55744	9.78	10.84	50
3154244	104	56824	0.47	32.52	42

continued on next page

Table B.1: *continued*

Event Num.	Day	Seconds	Rt. Asc. [h]	Declin. [^{o}]	N_{ch}
3750107	104	65535	7.82	74.09	33
4045415	104	69843	0.09	5.58	57
5840154	106	2616	3.03	21.47	27
2495921	106	40973	10.69	64.40	40
2928444	106	46764	7.72	73.77	46
3374821	106	52794	5.02	54.90	24
1985658	107	35724	16.82	6.80	25
471928	108	74771	11.31	51.28	39
3162260	109	25700	6.85	33.93	29
1208393	111	11378	21.67	47.24	28
1406501	111	14284	2.73	18.10	26
3484351	112	44540	19.55	36.77	31
5333153	112	71381	4.34	18.17	32
4829945	113	62913	13.32	2.44	61
488352	114	471	4.60	60.55	29
1140739	114	9763	20.58	1.40	39
1699573	114	17810	12.84	57.09	23
4527543	114	57349	11.08	67.41	34
5087764	114	65003	4.76	31.97	52
545025	115	915	12.82	53.52	31
1305562	115	11729	3.70	45.97	57
3273134	115	39229	1.80	47.24	27
4321045	115	54306	16.45	20.01	29
5693640	115	74032	5.19	16.49	25
653087	116	2961	5.47	20.19	24
1344026	116	12959	3.48	26.70	34
3233955	116	40794	3.15	39.73	28
4292412	116	56434	2.65	81.48	24
983255	117	8079	9.81	16.65	29
2623688	117	32414	7.36	14.40	44
4294055	117	57160	9.28	62.10	36
5616346	117	76774	9.42	2.17	37
4551231	118	60686	7.00	40.23	29
5817674	118	79349	9.68	49.54	31
1030608	119	8672	9.44	1.49	30
2163722	119	25341	19.06	49.15	46
4586445	119	60940	9.96	58.13	23

continued on next page

Table B.1: *continued*

Event Num.	Day	Seconds	Rt. Asc. [h]	Declin. [^{o}]	N_{ch}
4981039	119	66737	10.55	18.38	30
4438509	120	58496	15.08	80.13	40
5528885	120	74401	4.21	37.99	30
915341	121	7096	11.31	57.29	32
2070666	121	23463	13.43	10.41	32
2085362	121	23671	6.31	69.65	39
2905292	121	35304	22.22	53.58	27
3756210	121	47341	21.07	0.94	80
4703218	121	60776	5.22	63.66	46
5172909	121	67488	12.91	26.37	25
6014534	121	79559	16.58	42.87	35
224809	121	83779	2.43	46.55	36
747371	122	4864	11.22	24.38	46
887102	122	6871	22.58	38.47	31
1349324	122	13526	0.39	68.71	33
1861965	122	21086	14.21	0.46	35
2842946	122	35512	5.54	50.71	44
368226	122	85779	0.82	48.69	28
4285190	123	55896	21.18	35.97	28
4929757	123	64887	10.74	35.58	28
5029367	123	66276	2.35	58.33	40
5477189	123	72503	23.93	59.47	30
1573814	124	16407	2.26	34.21	31
4077610	124	52442	11.17	21.58	24
4332919	124	56145	11.10	79.51	50
4869527	124	63862	19.82	25.44	95
1654462	125	37190	8.77	53.52	25
1749335	125	38530	7.21	1.39	24
1947477	125	41342	4.37	49.82	33
5619504	126	6177	20.40	39.40	25
372857	126	19246	1.54	33.77	55
2611950	126	52094	4.98	12.50	55
3071680	126	58807	18.47	18.57	31
213326	127	16984	0.13	33.77	66
2310094	127	47992	10.24	33.17	34
1056477	129	26401	3.03	32.11	29
3279091	129	58751	0.59	11.20	27

continued on next page

Table B.1: *continued*

Event Num.	Day	Seconds	Rt. Asc. [h]	Declin. [^{o}]	N_{ch}
3628162	129	63814	3.01	10.94	50
102699	130	12332	4.84	21.41	33
1695899	130	36007	21.92	15.56	76
1801321	131	47349	9.07	11.91	36
1898807	131	48799	3.31	32.15	49
1935762	131	49350	5.80	22.43	43
2405773	131	56292	2.89	2.94	37
2910481	131	63737	2.33	21.66	30
3686705	132	73868	12.96	39.79	31
5609582	133	15167	16.35	19.01	28
1467722	133	41824	6.77	31.43	37
3465006	133	70663	6.58	31.09	20
5745413	134	17239	8.63	29.85	34
2846119	134	62068	20.86	70.90	30
4542990	135	314	0.02	1.66	24
1303222	135	39431	6.77	17.23	26
3385603	135	69448	2.79	65.99	34
1069891	136	36122	1.11	62.30	30
2719596	136	59874	9.92	41.24	30
4384033	136	84072	8.68	30.20	26
4819501	137	4034	13.09	33.03	25
5923655	137	20201	12.78	57.40	17
5929236	137	20282	15.18	51.97	33
5157441	138	9404	14.91	35.04	31
1329751	138	39833	11.45	56.12	35
4437595	138	85526	7.89	11.57	47
5281309	139	11665	10.23	49.53	47
301199	139	24950	10.06	38.99	39
698547	139	30669	21.32	39.83	27
1530546	139	42604	16.60	43.99	26
4098030	139	78564	8.76	17.45	24
441286	140	27023	23.22	45.44	32
1836554	140	46963	12.81	11.46	112
2707061	140	58698	5.19	26.85	43
5696095	141	14760	0.25	14.63	44
2309938	141	54161	22.94	68.70	44
2418728	141	55703	20.93	1.01	38

continued on next page

Table B.1: *continued*

Event Num.	Day	Seconds	Rt. Asc. [h]	Declin. [^{o}]	N_{ch}
2718534	141	59906	13.86	67.40	38
1974873	143	48216	22.40	18.26	36
4563241	143	84212	0.21	76.37	47
5303086	144	8026	18.26	80.71	24
5867358	144	16080	18.67	1.23	28
3348076	144	67364	14.78	23.78	32
3598260	144	70769	18.09	0.23	24
5391306	145	8804	2.10	33.67	45
239722	145	24012	7.27	78.35	31
1567237	145	42976	8.36	52.47	37
2072713	145	50117	9.47	33.97	36
2186626	145	51755	9.15	0.22	162
2218020	145	52216	6.85	16.90	29
3169934	145	66222	9.67	85.27	31
1836073	146	47683	10.11	14.35	29
4830613	147	4852	23.05	69.40	22
1355187	147	40489	15.08	79.22	86
1440392	147	41746	8.56	1.86	25
1930732	147	48786	20.64	18.63	30
941061	148	34754	3.24	2.78	35
2161655	148	53407	8.24	28.44	38
2165291	148	53461	0.62	78.98	33
4410924	149	1494	20.95	46.66	52
1453177	149	42938	13.24	34.60	28
3612050	149	76214	5.68	43.08	48
5491930	150	18802	23.02	37.64	20
1053797	150	36816	20.34	32.10	45
1085833	150	37311	12.88	45.48	23
3819978	151	80271	8.41	43.19	34
4211145	152	59	22.78	40.06	36
4807264	152	9491	1.73	47.08	36
610793	152	29879	6.28	57.36	52
1208246	152	39022	15.00	32.41	18
1259101	152	39800	17.69	58.04	32
1547045	152	44203	17.38	36.38	53
2954433	152	65697	15.23	45.01	45
3495958	153	72609	0.03	0.97	27

continued on next page

Table B.1: *continued*

Event Num.	Day	Seconds	Rt. Asc. [h]	Declin. [^{o}]	N_{ch}
866	154	504	7.75	78.07	41
3459315	154	75688	7.49	65.81	27
3878658	154	82241	4.94	17.64	118
4121944	154	86057	19.77	54.72	25
5475210	155	20904	15.11	42.94	22
4377402	156	4357	0.58	76.84	84
509647	156	26639	23.07	57.26	37
3926431	156	79174	19.70	35.04	27
4382518	156	86005	14.42	74.71	33
5014377	157	9280	0.71	53.26	29
1332216	157	74188	12.89	70.82	53
3670860	158	24725	6.04	86.16	41
4132334	158	31996	7.56	38.58	28
4748315	158	41704	20.96	1.55	23
2412706	159	47908	0.67	49.31	26
4817639	159	84703	6.26	5.72	25
1803916	160	43832	22.62	1.97	38
5133030	161	5924	22.77	5.73	32
166896	161	19392	11.82	18.76	33
1378782	161	37243	8.18	51.32	56
2876041	161	59628	20.83	36.23	44
799955	162	11907	14.08	6.58	28
1218145	162	18318	17.95	52.63	28
1987188	162	30087	6.75	0.51	25
2533762	162	38466	9.09	33.07	25
3770598	162	57483	8.49	20.37	22
672440	163	9733	1.85	0.98	69
3993165	163	59176	9.51	28.00	27
672095	164	9747	11.88	53.83	28
3914785	164	57971	0.32	51.59	35
4607462	164	68280	16.02	39.93	32
5526489	164	81907	14.16	34.46	54
1197689	165	17566	10.56	31.86	52
1981017	165	29355	16.78	47.27	23
2116222	165	31397	16.40	55.66	26
2300493	165	34173	13.52	52.76	22
2654773	165	39508	11.93	10.83	31

continued on next page

Table B.1: *continued*

Event Num.	Day	Seconds	Rt. Asc. [h]	Declin. [°]	N_{ch}
3681545	165	54909	10.36	36.59	30
1363912	166	19238	14.42	50.13	38
1550214	166	22204	2.14	1.87	29
364278	169	42895	2.09	31.36	24
3910453	170	12980	0.10	68.78	39
2579176	170	78372	3.76	70.70	72
2024699	171	69939	16.78	5.76	44
652870	172	39742	19.56	4.74	41
885675	173	43589	22.42	76.46	34
2774180	173	74412	8.01	4.08	37
1148976	174	47837	13.07	23.08	37
1997064	174	61407	11.83	82.86	58
4295459	175	11854	13.21	60.83	37
399490	175	35872	17.31	51.69	38
1255821	175	49102	11.80	1.41	25
1918694	175	59357	11.69	11.49	113
1097197	176	46464	23.88	77.75	23
4275575	177	8933	9.72	18.93	41
4576434	177	13566	10.76	54.58	40
408176	177	35815	10.57	33.10	31
871018	177	43005	0.07	18.52	39
938476	177	44066	14.24	39.72	35
5194469	178	24677	12.44	40.85	42
1766684	178	57507	3.69	31.83	32
2417299	178	67814	18.22	52.30	27
3819862	179	3644	20.01	53.92	24
4833861	179	19757	5.34	8.97	70
2171437	179	63929	0.04	59.70	43
2395183	179	67482	22.19	23.48	36
2419051	179	67861	16.30	61.52	38
3521648	179	85388	6.09	36.89	21
2049092	180	61978	11.28	86.59	38
353405	181	35074	9.70	1.52	30
4420050	182	13129	21.78	8.52	43
417433	182	36115	9.04	80.84	40
475650	182	37040	10.07	79.50	32
1001946	182	45392	18.70	40.93	67

continued on next page

Table B.1: *continued*

Event Num.	Day	Seconds	Rt. Asc. [h]	Declin. [^{o}]	N_{ch}
2202190	182	64432	20.46	35.31	30
2659702	182	71705	7.17	18.63	34
3211870	182	80496	5.01	20.79	38
3512935	182	85266	11.83	42.82	41
548845	183	38481	10.73	7.78	30
1796076	183	58910	2.00	31.58	27
3799899	184	4496	14.56	38.37	24
4028316	184	8107	14.44	10.38	232
491361	184	37508	20.53	55.63	72
2002836	184	62389	16.52	64.90	44
4895669	185	22986	6.22	39.33	33
3059438	185	77832	9.79	56.13	31
799334	186	28159	20.08	35.91	24
2668517	186	46430	16.45	12.20	37
4927557	186	68552	19.26	29.44	29
1114208	187	31305	9.24	0.77	42
1957663	187	39551	18.65	81.51	34
8395367	188	16293	4.35	33.38	30
425222	188	24540	2.49	38.35	32
1021126	188	30355	5.52	66.08	59
1580120	188	35850	21.37	30.45	26
1760779	188	37622	18.16	72.31	98
2665888	188	46507	4.40	41.94	54
984299	189	36423	11.15	12.20	34
3776343	189	80133	16.33	51.57	56
573627	190	30102	18.27	53.27	33
1509044	190	44759	7.16	2.68	26
1958212	191	52710	23.51	25.18	32
2785061	191	65962	18.89	24.48	33
5370254	192	21043	7.25	21.71	23
1661314	192	47058	22.10	5.72	31
1744920	199	30453	18.45	14.52	74
3915916	199	65586	12.65	46.00	35
5276912	200	1153	6.88	52.62	28
4537450	200	74846	14.46	19.14	27
4708149	200	77560	23.02	65.05	57
5320342	201	875	15.44	5.33	26

continued on next page

Table B.1: *continued*

Event Num.	Day	Seconds	Rt. Asc. [h]	Declin. [^{o}]	N_{ch}
1583087	201	27120	23.96	0.34	27
4138556	201	67851	23.03	48.23	35
4974272	201	81235	20.83	42.37	28
395645	202	8534	14.96	24.07	33
129583	202	21256	2.28	42.50	33
132811	202	21309	7.33	29.81	26
2137011	202	53807	18.96	83.46	49
4586796	203	6902	19.00	16.92	51
4592349	203	6990	7.83	35.15	42
5058855	203	14452	23.12	20.01	69
967389	203	34768	19.97	56.02	23
3907278	203	81885	18.37	0.81	39
4633118	204	7066	17.64	43.69	27
3268457	205	70492	8.83	4.39	28
2248138	207	27337	15.28	46.65	26
3282703	207	43276	6.89	75.09	49
4869710	207	67781	23.14	29.93	27
64253	207	79346	8.63	53.11	24
5073299	208	66752	14.44	23.98	31
4111686	210	64351	23.83	60.25	37
4579870	210	72017	17.32	18.27	27
5147663	210	81242	20.72	13.60	38
246923	211	1296	1.45	22.46	29
1691281	212	39856	21.13	3.98	40
4637678	213	1538	9.71	46.63	29
2491556	213	53971	4.38	47.76	35
4092401	213	80203	17.56	6.21	68
65969	214	14376	10.53	7.42	84
2087472	214	47836	14.36	30.34	39
2281801	214	51055	9.28	3.37	40
3292675	214	67830	4.89	54.30	51
3818291	214	76526	20.84	44.99	26
1746315	216	42265	17.22	32.53	5
525984	217	21979	13.80	44.49	24
856749	218	27389	6.34	51.24	32
955188	218	29026	12.84	42.48	22
3336654	218	68371	18.93	63.97	49

continued on next page

Table B.1: *continued*

Event Num.	Day	Seconds	Rt. Asc. [h]	Declin. [^{o}]	N_{ch}
821013	220	18603	12.14	1.89	27
3386140	220	59056	15.08	20.08	22
162130	221	7639	8.61	1.73	74
2332133	221	42706	9.66	1.45	36
5110864	222	1922	23.98	59.48	39
2089774	222	39160	15.23	59.48	34
3055268	222	54915	7.98	40.98	33
4872625	223	82617	17.65	2.07	55
5354954	224	4023	22.51	58.96	18
89496	224	6455	4.71	12.83	32
332303	224	10312	16.03	56.28	36
3867415	224	68082	12.35	75.12	48
1853106	226	34152	11.80	43.99	35
3593604	226	61812	21.29	81.44	133
64573	227	6057	21.99	46.07	40
1545937	227	30272	11.16	2.39	43
1760196	227	33795	0.71	27.77	32
2586098	227	47309	2.48	1.25	28
2867881	227	51899	2.71	55.83	34
1635083	234	34760	3.10	44.47	28
4650863	235	65961	3.19	10.68	85
4953315	236	69495	21.17	68.25	27
5162621	236	72724	7.22	56.49	64
1697	236	79549	22.48	58.58	30
1693124	238	20805	4.98	19.44	32
1728274	239	21978	19.42	1.39	24
3533809	239	52039	18.72	32.08	28
3565440	239	52563	12.07	83.86	25
4162247	239	62500	2.29	10.25	31
21924	239	79864	9.79	13.78	38
2337283	240	31991	11.06	30.58	32
4182481	240	62694	16.71	42.87	23
111005	240	81350	3.73	0.71	58
2490049	241	34607	20.32	0.55	30
520134	242	1781	7.24	53.05	43
1433197	242	16919	8.24	60.53	37
2365707	242	32557	6.78	17.18	56

continued on next page

Table B.1: *continued*

Event Num.	Day	Seconds	Rt. Asc. [h]	Declin. [^{o}]	N_{ch}
2762494	242	39160	3.62	39.89	54
3009792	242	43327	11.53	68.68	64
3014988	242	43414	16.20	6.80	31
576848	243	2841	6.32	82.10	23
1475367	243	17709	7.31	70.52	32
1730523	243	21979	18.32	28.01	24
2425443	243	33639	12.30	0.74	25
2533885	243	35453	0.64	32.27	61
3184282	244	47237	13.13	44.04	28
4196058	244	64532	9.32	41.84	36
4685513	244	72883	12.45	4.57	28
1536994	245	19531	1.63	77.90	64
1573409	245	20163	21.99	20.56	39
1830710	245	24620	13.36	42.54	22
2901500	245	43127	2.16	79.41	22
1013252	246	10623	17.94	26.68	34
4679714	246	73861	10.19	18.52	51
1608536	249	20976	0.64	32.51	34
1701274	249	22564	19.53	15.84	27
2843674	249	42141	5.89	46.60	34
389600	250	193	10.44	63.40	35
686114	250	5270	6.19	1.48	24
2240798	250	31921	17.32	40.14	36
2434075	250	35234	20.45	20.78	31
3014760	250	45176	15.57	49.61	27
3171153	250	47853	13.03	2.49	26
1595767	251	20927	12.72	9.68	31
2608500	252	38357	13.38	41.46	25
99861	252	81590	2.46	20.46	30
4345784	253	67837	19.22	13.66	45
5034218	253	79592	11.78	1.61	56
1124617	254	12681	21.45	10.02	69
2669207	254	39007	8.17	47.83	35
4106905	254	63515	21.40	41.00	37
2060472	255	28329	14.75	42.18	30
4648526	255	72213	0.88	28.43	44
1545291	256	19660	21.24	40.30	38

continued on next page

Table B.1: *continued*

Event Num.	Day	Seconds	Rt. Asc. [h]	Declin. [^{o}]	$\mathrm{N_{ch}}$
1867813	257	25126	8.82	14.41	27
4919462	258	33512	9.92	22.08	27
1645042	258	65202	19.70	11.60	29
3300293	259	6874	22.46	34.80	41
4663929	259	30052	11.40	2.30	31
831360	259	51457	15.00	38.15	30
978070	260	19862	15.93	53.63	28
4234847	260	75112	10.89	4.28	63
4519966	260	79841	3.99	24.82	29
1740457	261	32591	8.40	36.30	29
486914	262	11247	20.75	64.94	38
1470638	262	27786	0.07	2.24	20
3208799	262	56973	13.84	34.03	32
3748156	262	66005	16.69	23.03	34
730347	263	15520	1.61	52.87	36
2084416	263	38257	5.98	75.75	35
2517339	263	45440	3.32	47.39	30
2845681	263	50958	22.71	41.15	25
3492598	263	61802	6.56	38.64	29
1172768	264	22670	22.24	50.89	45
2200836	264	39783	14.89	46.51	38
3220315	264	56553	4.38	71.14	36
4140788	265	73334	12.44	33.75	43
234639	266	7208	14.81	10.62	104
394540	267	9751	5.25	47.32	24
1368619	267	25855	9.53	21.41	26
3910373	267	67982	17.41	0.41	58
44693	268	3957	1.61	42.49	32
2079433	268	38328	22.10	22.94	54
2363088	268	43116	7.32	14.55	27
423496	269	10388	1.31	31.90	68
787075	269	16556	10.83	10.24	63
1208815	269	23714	8.52	85.47	30
2324445	269	42426	9.43	39.60	23
3415232	269	60723	23.25	30.09	25
4697157	269	82233	22.46	11.34	29
1457590	270	27681	10.79	4.42	25

continued on next page

Table B.1: *continued*

Event Num.	Day	Seconds	Rt. Asc. [h]	Declin. [^{o}]	N_{ch}
4475024	270	78197	2.27	61.46	31
2258153	271	40194	6.75	78.97	43
3480654	271	60488	21.73	44.32	29
4260023	271	73586	20.48	0.77	92
28561	272	3657	8.47	83.88	41
214575	272	6761	1.57	17.66	24
1339798	272	25576	22.30	18.13	44
1712004	272	31614	12.01	41.80	56
3002342	272	52781	11.37	60.32	22
1633951	273	30637	14.29	1.62	64
3136000	273	55679	13.66	74.35	24
4839112	273	84158	3.20	53.00	29
2411812	274	43215	4.45	23.20	55
70296	275	4305	11.87	65.15	118
2808416	275	49916	20.65	21.53	46
3187840	275	56101	8.20	17.71	61
3492058	275	60995	7.72	11.27	38
466376	276	10974	7.86	2.96	63
2861464	276	51012	5.86	84.71	42
2880198	276	51327	16.57	56.66	44
3290529	276	58161	12.24	55.95	25
1920910	277	35059	2.30	1.76	57
3638945	277	63517	16.82	73.58	49
3671632	277	64059	15.50	44.46	37
1948674	278	34725	21.76	73.00	28
2395528	278	41799	10.92	75.29	39
4540918	278	75983	13.37	30.98	28
4573922	278	76527	23.15	53.49	28
2828443	279	49151	10.40	45.85	25
4008483	279	68607	20.28	49.53	44
1141409	280	22172	11.43	14.59	49
1680617	280	31159	23.94	19.18	25
2651168	280	47364	22.69	72.62	35
2736465	280	48792	13.84	29.29	32
3618665	280	63490	0.39	76.71	34
412098	281	9981	2.24	59.95	51
1560336	281	29095	4.04	39.70	38

continued on next page

Table B.1: *continued*

Event Num.	Day	Seconds	Rt. Asc. [h]	Declin. [^{o}]	N_{ch}
3660323	281	64068	0.13	31.19	19
5113287	282	1843	23.20	61.29	59
122072	282	5162	7.29	80.65	44
511925	282	11660	14.97	33.00	98
2207942	282	39921	15.25	45.74	51
3427166	282	60258	11.00	37.91	32
3571269	282	62667	11.20	16.89	55
3759241	282	65803	7.82	19.42	65
4589828	282	79684	13.57	1.15	31
758164	283	15773	9.24	45.81	28
1096311	283	21407	5.19	31.32	41
3017864	283	53379	1.85	22.03	29
1418387	284	26701	1.00	69.31	30
1725932	284	31818	3.13	36.85	32
4011793	284	69828	23.05	2.48	26
4994987	284	86095	3.28	62.16	35
25856	285	3511	16.96	42.30	24
525762	285	11684	15.22	39.85	25
1535236	285	28293	12.89	43.75	31
2700849	285	47408	20.15	44.11	38
3154203	285	54831	20.63	5.88	25
3374037	285	58414	6.38	50.46	37
3407046	285	58951	6.69	60.14	39
3686412	285	63518	9.13	56.63	24
3874632	285	66587	21.67	57.53	38
5255931	286	2657	14.41	1.99	32
1245839	286	23335	9.91	21.18	26
1740923	287	31158	9.93	19.00	26
3488013	287	59077	4.59	49.09	69
3881741	287	65419	2.39	4.64	48
5021362	287	83731	22.44	23.96	39
5212833	288	413	21.15	68.25	31
2264527	288	39680	7.89	53.99	28
2750296	288	47508	23.32	18.53	57
1664954	289	29865	11.26	44.03	25
3466077	289	58542	22.98	61.27	22
4903090	289	81508	17.87	61.62	62

continued on next page

Table B.1: *continued*

Event Num.	Day	Seconds	Rt. Asc. [h]	Declin. [^{o}]	N_{ch}
1310392	290	24329	3.83	70.81	37
2652262	290	46055	22.37	6.34	41
2843210	290	49153	1.78	35.66	38
4382458	290	74055	19.66	48.95	49
4787184	290	80599	23.89	6.97	24
239640	291	6936	4.21	1.17	46
2516121	291	43605	17.39	20.43	30
3357016	291	56851	23.76	26.29	37
4054707	291	67915	6.87	21.61	26
215224	292	6478	20.90	64.45	41
1735409	292	30539	14.36	27.49	156
3341036	292	56165	17.00	22.20	49
4253360	292	69993	11.52	47.70	26
883409	293	17082	22.15	0.45	87
943232	293	18035	23.10	60.82	20
1023078	293	19304	21.69	1.54	29
1724267	293	30401	11.28	29.14	150
1899601	293	33182	13.04	8.94	24
2478105	293	42309	1.70	77.62	21
5410121	294	2246	22.58	31.99	35
1630711	294	29025	13.60	32.09	23
2896018	294	49188	13.56	9.76	30
4321534	294	71929	3.96	1.27	24
5056787	295	83031	21.24	1.20	32
1546608	296	27421	10.55	34.32	66
2536284	296	43025	22.30	36.12	37
4577801	296	75216	18.51	5.63	26
5354236	297	1078	0.03	20.88	41
2393966	297	40897	16.77	35.45	27
2586815	297	43959	22.23	43.90	48
4113525	297	68122	3.70	44.61	48
3814241	298	63746	10.65	2.54	53
414608	299	9612	1.43	0.98	42
472032	299	10524	16.37	2.28	33
997065	299	18841	12.34	44.26	25
1051944	299	19712	13.43	8.55	54
3016875	299	50973	7.06	59.13	30

continued on next page

Table B.1: *continued*

Event Num.	Day	Seconds	Rt. Asc. [h]	Declin. [^{o}]	N_{ch}
3977189	299	66272	2.60	29.62	59
484165	300	10714	19.57	0.33	19
3465498	300	58303	22.43	2.14	44
4238638	300	70683	21.44	0.23	20
2401616	301	41101	1.34	46.50	30
51239	302	8902	11.21	19.79	23
1297596	302	28395	4.25	23.99	47
3842463	302	68102	20.63	19.56	113
4110705	302	72274	23.55	40.68	32
4329713	302	75681	15.30	56.27	30
563256	303	16955	8.38	29.14	35
1895817	303	37770	6.13	4.08	31
126491	305	39650	9.86	65.59	61
2558651	305	77327	10.91	2.33	32
3277996	307	642	3.84	58.84	48
3927550	307	10660	10.51	2.26	36
4953648	309	40121	8.16	3.31	116
2297976	309	85434	18.15	48.91	51